

UCD-PHYC/071001
arXiv:0710.2838 [hep-ex]
15 October 2007

arXiv:0710.2838v1 [hep-ex] 15 Oct 2007

Experimental Precision Tests for the Electroweak Standard Model

Martin W. Grünewald

University College Dublin
UCD School of Physics
Belfield, Dublin 4
Ireland

Abstract

This paper contains a review of recent precision measurements of electroweak observables and resulting tests of the electroweak Standard Model.

Invited Chapter for a Handbook of Particle Physics

1 Experimental Precision Tests for the Electroweak Standard Model

MARTIN W. GRÜNEWALD
UNIVERSITY COLLEGE DUBLIN
UCD SCHOOL OF PHYSICS
BELFIELD
DUBLIN 4
IRELAND
e-mail: Martin.Grunewald@cern.ch

1.1 Introduction

The last twenty years have seen enormous progress in experimental precision measurements in particle physics and tests of the electroweak Standard Model. New generations of experiments using advanced detectors at high-energy particle colliders perform measurements with a precision unprecedented in high-energy particle physics. This review summarises the major exciting experimental results measured at the highest energies and pertaining to the electroweak interaction. Comparisons with the theory, the Standard Model of particle physics (SM) [1], are used to test the theory and to constrain its free parameters. The data sets analysed for the precision measurements presented here have been accumulated at the world's highest-energy particle colliders over the last two decades. They verify the SM as a renormalisable field theory correctly describing nature.

Electron-positron collisions at 91 GeV centre-of-mass energy were studied by the SLD detector [8], operating at Stanford's Linear Collider (SLC) [12] (1989-1998), and by the experiments ALEPH [13], DELPHI [15], L3 [17] and OPAL [21], taking data at the Large Electron Positron collider (LEP) [25] (1989-1995) at the European Laboratory for Particle Physics, CERN, Geneva, Switzerland. This centre-of-mass energy corresponds to the mass of the Z boson, the heavy neutral exchange particle of the electroweak interaction, which is thus produced in resonance, $e^+e^- \rightarrow Z$. While SLC provided interactions at a fixed centre-of-mass energy corresponding to the maximum of the Z resonance cross section, the LEP-I collider provided collisions at several centre-of-mass energy points, thereby scanning the Z resonance lineshape in the range from 88 GeV to 94 GeV. By increasing the LEP center-of-mass energy up to 209 GeV (LEP-II, 1996-2000), the precision measurements of Z-boson properties at LEP-I were complemented by measurements of the properties of the W-boson, the charged carrier of the electroweak interaction, in the reaction $e^+e^- \rightarrow W^+W^-$ at LEP-II.

Proton-antiproton collisions are provided by the Tevatron collider operating at the Fermi Na-

tional Accelerator Laboratory close to Chicago in the USA, at centre-of-mass energies of 1.8 TeV (Run-I, 1992-1996) and 2.0 TeV (Run-II, since 2001), and are studied by the experiments CDF [29] and DØ [30]. Results from the Tevatron experiments important for the electroweak interaction include measurements of the mass of the W boson, as well as the discovery of the sixth and heaviest quark known today, the top quark, in 1995 and the measurements of its properties, in particular its mass.

In addition, key measurements were performed in dedicated experiments at lower interaction energies, notably the measurement of the anomalous magnetic moment of the muon [32], as well as the measurements of parity violation effects in atomic transitions [33, 34, 35], in Moller scattering [36, 37] and in neutrino-nucleon scattering [38]. The following sections summarise the major experimental measurements of particular relevance to electroweak physics, starting with electron-positron collisions at the Z pole and above the W-pair threshold, the measurements at the Tevatron collider, and the specialised measurements at lower momentum transfer. The combined set of experimental results is compared to predictions based on the Standard Model of particle physics and used to constrain its free parameters. In particular, the predictive power of the SM and the precision of the electroweak measurements is elucidated by the predictions of the masses of heavy fundamental particles, such as W boson, top quark and Higgs boson, which are contrasted with the direct measurements of these quantities.

1.2 Fermion-Pair production and the Z resonance

1.2.1 Introduction

Fermion-pair production is the dominant interaction in electron-positron collisions. The two important Feynman diagrams in fermion-antifermion production, shown in Figure 1.1, proceed through s -channel exchange of the neutral electroweak gauge bosons, namely photon (γ) and Z boson.

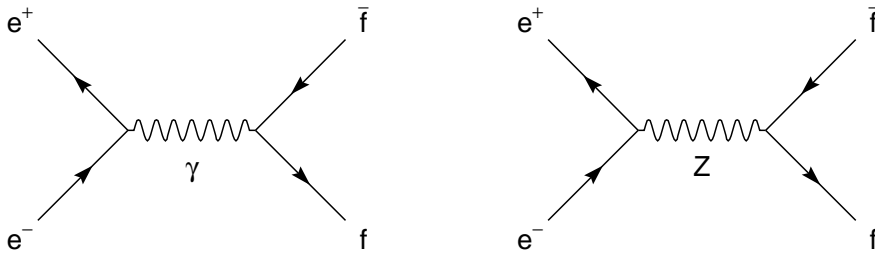


Figure 1.1: The lowest-order s -channel Feynman diagrams for the reaction $e^+e^- \rightarrow f\bar{f}$. For e^+e^- and $\nu_e\bar{\nu}_e$ final states, additional t -channel diagrams with photon, Z- or W-boson exchange contribute as well. The contribution of Higgs boson exchange diagrams is negligible.

The Z-exchange diagram causes a resonant enhancement of the total cross section by nearly three orders of magnitude when the centre-of-mass energy, \sqrt{s} , is close to the mass of the Z boson, m_Z . In the vicinity of the Z pole, the total and differential cross sections for fermion-pair production, $e^+e^- \rightarrow f\bar{f}$, are given by:

$$\sigma^0(e^+e^- \rightarrow f\bar{f}; s) = \frac{12\pi}{m_Z^2} \frac{\Gamma_{ee}\Gamma_{f\bar{f}}}{\Gamma_Z^2} \frac{s\Gamma_Z^2}{(s - m_Z^2)^2 + s^2\Gamma_Z^2/m_Z^2} + \gamma/Z \text{ interference} + \text{photon exchange} \quad (1)$$

$$\frac{d\sigma^0(s)}{d\cos\theta} = \sigma^0(s) \left[\frac{3}{8}(1 + \cos^2\theta) + A_{\text{FB}}^{0,f}(s) \cos\theta \right] \quad (2)$$

where the additional terms not further specified are small. The angle θ denotes the polar scattering angle of the outgoing fermion with respect to the direction of the incoming electron. The dependence of the total cross section and the forward-backward asymmetry on the centre-of-mass energy is shown in Figure 1.2. The effect of radiation of photons in the initial state on cross section and forward-backward asymmetry, very large as shown in Figure 1.2, is incorporated in the calculations by a convoluting the above expressions with QED radiator functions to yield realistic predictions, which are compared to the experimental measurements. These realistic, QED-convoluted observables are indicated by dropping the superscript 0 from the above pole-like quantities. The QED-deconvoluted quantities, indicated by the superscript 0, are sometimes also called pseudo observables. The numerical calculations are performed with Monte Carlo programs as well as the semi-analytical programs TOPAZ0 [39] and ZFITTER [43], which incorporate state-of-the-art higher-order radiative corrections.

The total and partial decay widths of the Z boson, Γ_Z and $\Gamma_{f\bar{f}}$ for fermion species f ($Z \rightarrow f\bar{f}$), are:

$$\Gamma_Z = \sum_{f \neq t} \Gamma_{f\bar{f}} = \Gamma_{\text{had}} + \Gamma_{ee} + \Gamma_{\mu\mu} + \Gamma_{\tau\tau} + 3\Gamma_{\nu\bar{\nu}} \quad (3)$$

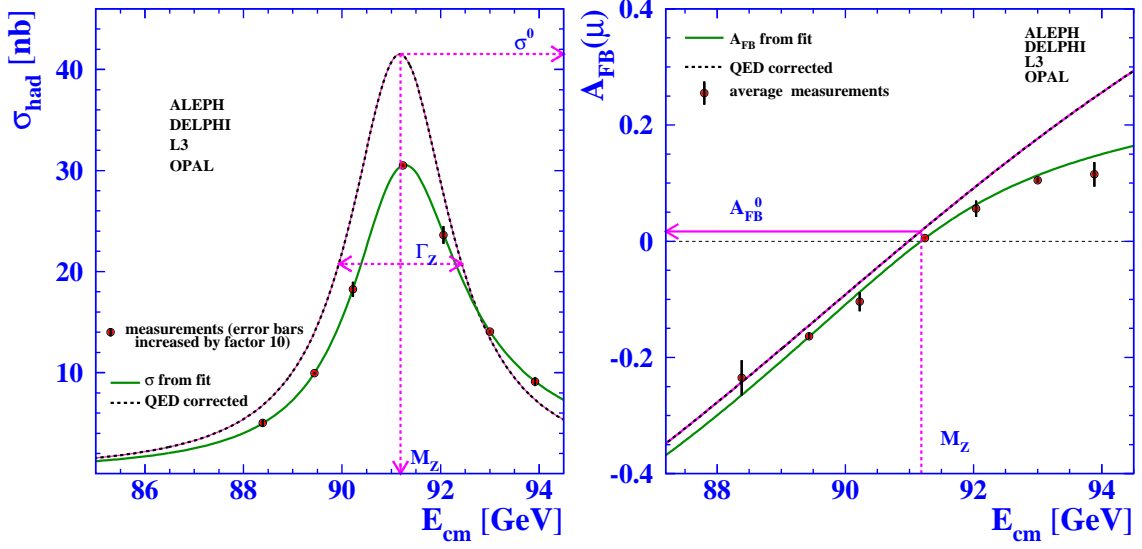


Figure 1.2: Left: average over measurements of the total inclusive hadronic cross-section of the process $e^+e^- \rightarrow q\bar{q}$, Equation 1. Right: average over measurements of the forward-backward asymmetry A_{FB}^μ in muon production, $e^+e^- \rightarrow \mu^+\mu^-$, Equation 2. The measurements are shown as a function of the centre-of-mass energy. The full line represents the result of a fit including QED radiative corrections to the measurements as described in the text. Unfolding for QED radiative effects yields the dashed curves, corresponding to the Z parameters shown in Equations 1 and 2.

$$\Gamma_{\text{ff}} = N_C^f \frac{G_F m_Z^3}{6\pi\sqrt{2}} (g_{Vf}^2 + g_{Af}^2) \quad (4)$$

where Γ_{had} is the inclusive hadronic decay width summed over the five light quark flavours, u, d, s, c, and b (top is too heavy), N_C^f is the QCD colour factor (3 for quarks and 1 for leptons), and g_{Vf} and g_{Af} are the effective vector and axial-vector coupling constants of the neutral weak current, i.e., the coupling of the Z boson to fermion species f. The QED-deconvoluted forward-backward asymmetry $A_{\text{FB}}^{0,f}$ at $\sqrt{s} = m_Z$, excluding photon exchange and γZ interference, decomposes into factors of coupling constants for the initial state and for the final state as follows:

$$A_{\text{FB}}^{0,f} = \frac{3}{4} \mathcal{A}_e \mathcal{A}_f \quad (5)$$

$$\mathcal{A}_f = \frac{2 g_{Vf} g_{Af}}{g_{Vf}^2 + g_{Af}^2} = 2 \frac{g_{Vf}/g_{Af}}{1 + (g_{Vf}^2/g_{Af}^2)}, \quad (6)$$

where \mathcal{A}_f is called the asymmetry parameter. Hence, measurements of both cross-sections and forward-backward asymmetries allow us to disentangle and determine the effective vector and axial-vector coupling constants g_{Vf} and g_{Af} . The asymmetry parameters and thus forward-backward asymmetries alone determine directly the effective electroweak mixing angle, because:

$$\frac{g_{Vf}}{g_{Af}} = 1 - 4|Q_f| \sin^2 \theta_{\text{eff}}^f, \quad (7)$$

where Q_f is the electric charge of fermion f.

1.2.2 Z Lineshape and Forward-Backward Asymmetries

At LEP, data samples were collected at various centre-of-mass energy points around the Z resonance. Measurements are routinely performed separating four final states: the three charged lepton species, e^+e^- , $\mu^+\mu^-$, and $\tau^+\tau^-$ and the inclusive hadronic final state arising from $q\bar{q}$ production.¹ Total cross sections are measured for all four final states. Differential cross sections and forward-backward asymmetries are measured for the lepton-pair final states.² Each LEP experiment collected a total integrated luminosity of about 200 pb^{-1} , with the datasets of the four LEP experiments combined consisting of about 15.5 million hadronic events and 1.7 million lepton-pair events.

The different final states are separated based on multiplicity (high-multiplicity hadronic jets arising from quark fragmentation, versus low-multiplicity charged leptons) and the characteristic signatures of the different charged lepton species as illustrated in Figure 1.3: electrons deposit all their energy in the electromagnetic calorimeter while muons traverse the complete detector as minimal ionising particles with their momentum measured by the inner and outer tracking systems. Tau leptons decay before they are measured by the detectors and are thus identified by their low-multiplicity decay signature different of that of di-electrons and di-muons and the high-multiplicity quark-jets, combined with missing energy due to neutrinos.

Owing to the highly advanced detectors with near 4π coverage, backgrounds in the selected samples are typically at the 1% level only. Event selection efficiencies within the acceptance range from 70% for $\tau^+\tau^-$ to more than 99% for hadrons. Systematic errors are smallest for the inclusive hadronic final states, typically 0.04% to 0.1%, and somewhat larger for the leptonic final states, up to 0.7% especially for tau-pairs. In addition, the luminosity uncertainty of 0.07% to 0.24%, depending on data taking period, is correlated between all cross section measurements. Detailed informations on the analyses are given in the References [52, 57, 61, 65].

The large data samples enable to perform precision cross section and asymmetry measurements as shown in Figures 1.2 and 1.4. The effect of initial-state photon radiation is clearly visible in Figure 1.2. It must be controlled to per-mill precision and better to allow the determination of the underlying Z resonance parameters such as mass, total and partial decay widths, pole cross sections and pole asymmetries, with unspoiled precision. Differential cross sections measured in e^+e^- and $\mu^+\mu^-$ production are shown in Figure 1.4. The t -channel exchange contribution in e^+e^- production changes the differential and also total cross section compared to the s -channel only production of the other charged fermions. This effect is of course taken into account in the analysis of e^+e^- production.

For reduced correlations between the observables, the measurements of Z-boson parameters are presented using the parameters [69]: m_Z , Γ_Z , $\sigma_{\text{had}}^0 = \sigma^0(e^+e^- \rightarrow \text{hadrons})$ at $\sqrt{s} = m_Z$, $R_\ell^0 = \sigma_{\text{had}}^0/\sigma_{\text{lep}}^0 = \Gamma_{\text{had}}/\Gamma_{\ell\ell}$ and $A_{\text{FB}}^{0,\ell} = 3\mathcal{A}_e\mathcal{A}_\ell/4$ for $\ell = e, \mu, \tau$. These nine pseudo observables reduce to five under the assumption of neutral-current charged-lepton universality. The results of the four LEP experiments are compared in Figure 1.5; combined numerical results [69] are also reported in Table 1.1. The χ^2/dof of the combination indicates that the model describes the data well. The mass of the Z boson is determined with a precision of 23 ppm, and its total width with per-mill precision. Uncertainties due to the absolute and relative LEP beam-energy calibration [70] affect the averaged results on m_Z and Γ_Z at the level of 1.7 MeV and 1.2 MeV, respectively, showing how precise a LEP beam energy calibration was achieved. The measurement of luminosity affects σ_{had}^0 only. Both statistical and systematic uncertainties on efficiency and acceptance contribute to the total uncertainty on R_ℓ^0 , while the forward-backward asymmetries are still statistics dominated. Neutral current lepton universality is strongly favoured by the results for R_ℓ^0 and $A_{\text{FB}}^{0,\ell}$ as shown in Figure 1.6, where the contours for electrons, muons and taus largely overlap. Numerical results imposing lepton universality are also reported in Table 1.1.

¹For a separation of quark flavours, see Section 1.2.5.

²For a measurement of an inclusive hadronic charge asymmetry, see Section 1.2.6.

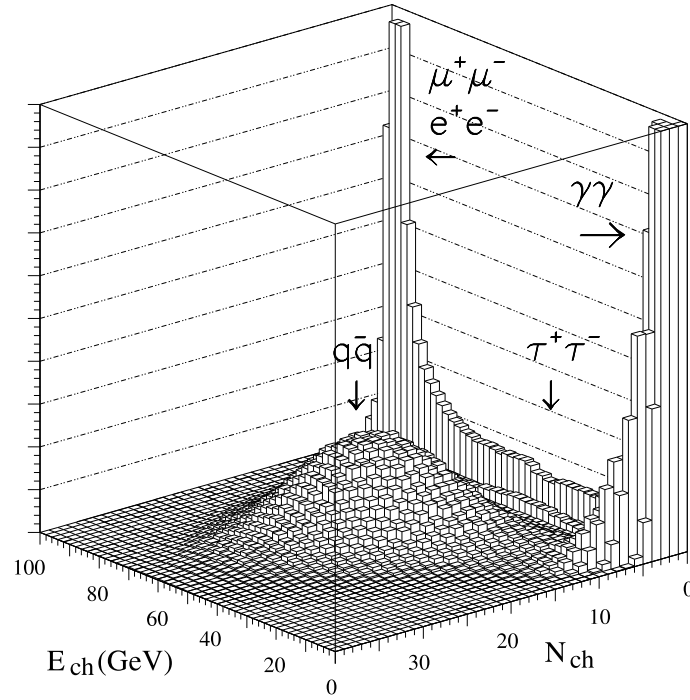


Figure 1.3: Experimental separation of the final states using only two variables, the sum of the track momenta, E_{ch} , corresponding to the energy carried by charged hadrons, and the track multiplicity, N_{ch} , in the central detector of the ALEPH experiment.

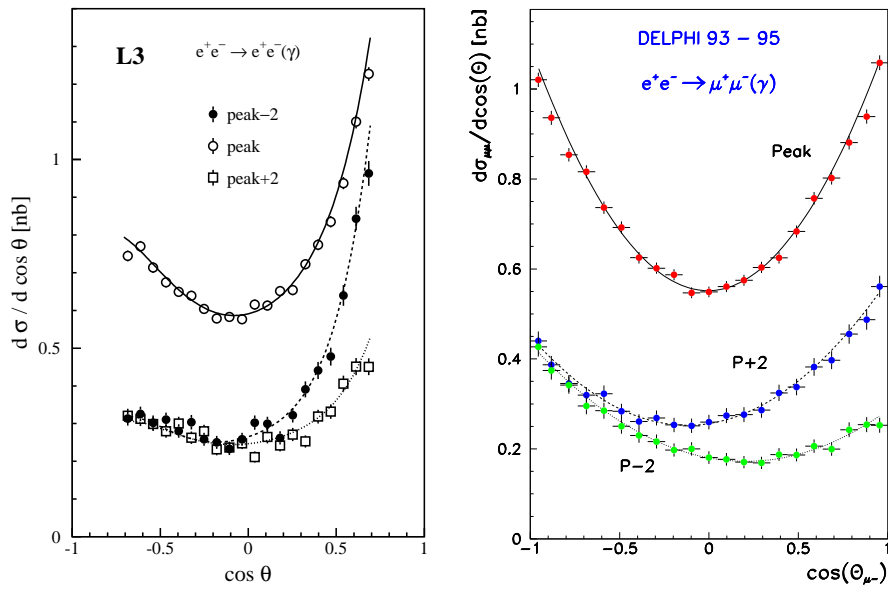


Figure 1.4: Distribution of the production polar angle, $\cos\theta$, for e^+e^- and $\mu^+\mu^-$ events at the three principal energies during the years 1993–1995, measured in the L3 (left) and DELPHI (right) detectors, respectively. The curves show the SM prediction from ALIBABA [51] for e^+e^- and a fit to the data for $\mu^+\mu^-$ assuming the parabolic form of the differential cross-section given in the text. The labels “peak” and “peak \pm 2” correspond to the centre-of-mass energy of the peak, and energy points about ± 2 GeV below and above the cross section peak.

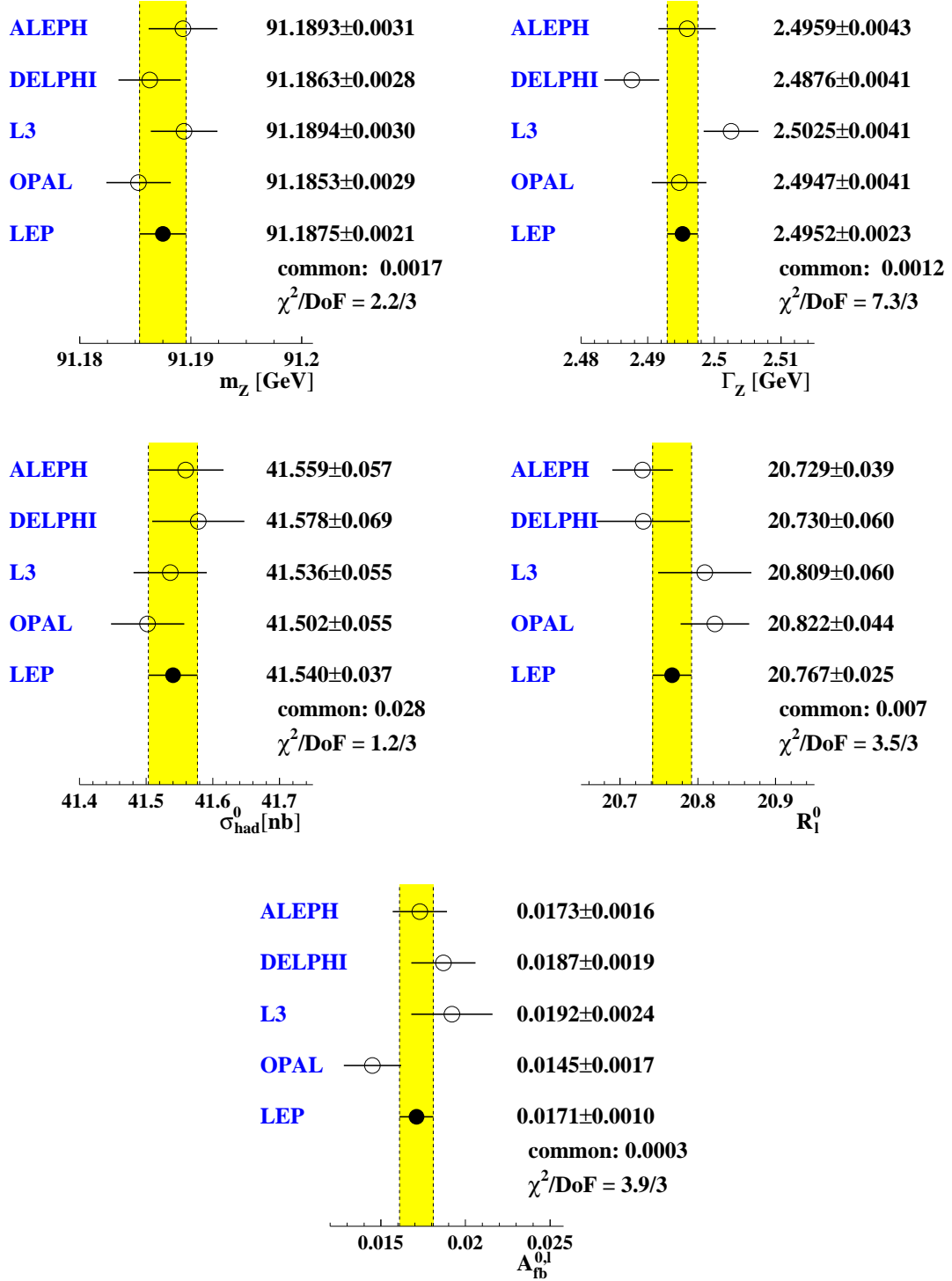


Figure 1.5: Measurements of m_Z , Γ_Z , σ_{had}^0 , R_ℓ^0 and $A_{\text{FB}}^{0,\ell}$. The averages indicated were obtained taking correlated uncertainties into account. The values of χ^2 per degree of freedom were calculated considering error correlations between measurements of the same parameter, but not error correlations between different parameters.

Table 1.1: Combined results for the Z parameters, without (top) and with (bottom) the assumption of lepton universality.

Without lepton universality		Correlations								
$\chi^2/\text{dof} = 32.6/27$		m_Z	Γ_Z	σ_{had}^0	R_e^0	R_μ^0	R_τ^0	$A_{\text{FB}}^{0,e}$	$A_{\text{FB}}^{0,\mu}$	$A_{\text{FB}}^{0,\tau}$
m_Z [GeV]	91.1876 ± 0.0021	1.000								
Γ_Z [GeV]	2.4952 ± 0.0023	-0.024	1.000							
σ_{had}^0 [nb]	41.541 ± 0.037	-0.044	-0.297	1.000						
R_e^0	20.804 ± 0.050	0.078	-0.011	0.105	1.000					
R_μ^0	20.785 ± 0.033	0.000	0.008	0.131	0.069	1.000				
R_τ^0	20.764 ± 0.045	0.002	0.006	0.092	0.046	0.069	1.000			
$A_{\text{FB}}^{0,e}$	0.0145 ± 0.0025	-0.014	0.007	0.001	-0.371	0.001	0.003	1.000		
$A_{\text{FB}}^{0,\mu}$	0.0169 ± 0.0013	0.046	0.002	0.003	0.020	0.012	0.001	-0.024	1.000	
$A_{\text{FB}}^{0,\tau}$	0.0188 ± 0.0017	0.035	0.001	0.002	0.013	-0.003	0.009	-0.020	0.046	1.000

With lepton universality		Correlations				
$\chi^2/\text{dof} = 36.5/31$		m_Z	Γ_Z	σ_{had}^0	R_ℓ^0	$A_{\text{FB}}^{0,\ell}$
m_Z [GeV]	91.1875 ± 0.0021	1.000				
Γ_Z [GeV]	2.4952 ± 0.0023	-0.023	1.000			
σ_{had}^0 [nb]	41.540 ± 0.037	-0.045	-0.297	1.000		
R_ℓ^0	20.767 ± 0.025	0.033	0.004	0.183	1.000	
$A_{\text{FB}}^{0,\ell}$	0.0171 ± 0.0010	0.055	0.003	0.006	-0.056	1.000

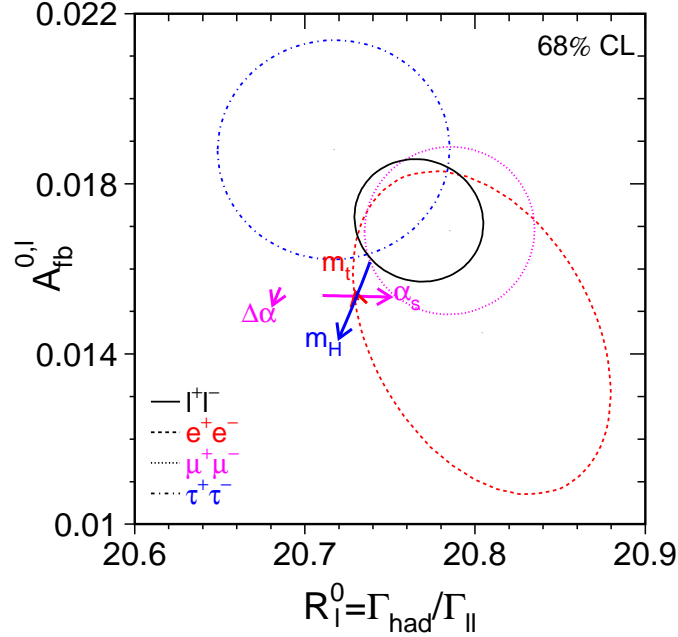


Figure 1.6: Contour lines (68% CL) in the $R_\ell^0 - A_{\text{FB}}^{0,\ell}$ plane for e^+e^- , $\mu^+\mu^-$ and $\tau^+\tau^-$ pairs, without and with the assumption of lepton universality, $\ell^+\ell^-$. The results for the τ lepton are corrected to correspond to the massless case. The SM prediction is shown as arrows corresponding to variations of $m_Z = 91.1875$ GeV, $m_t = 170.9 \pm 1.8$ GeV, $m_H = 300^{+700}_{-186}$ GeV, $\alpha_S(m_Z^2) = 0.118 \pm 0.003$. The arrow showing the dependence on the hadronic vacuum polarisation $\Delta\alpha_{\text{had}}^{(5)}(m_Z^2) = 0.02758 \pm 0.00035$ is displaced for clarity.

1.2.3 Polarised Asymmetries at SLC

In contrast to LEP where the beams were unpolarised, SLC provided electron-positron collisions with longitudinally polarised electrons. The beam polarisation as a function of Z event count is shown in Figure 1.7, indicating that polarisation in excess of 70% was routinely achieved for the bulk of the data. In order to measure polarised asymmetries such as left-right and left-right forward-backward asymmetries with highest possible statistical precision, SLC maximised the event count by providing collisions at a single fixed centre-of-mass energy only, corresponding to the maximum of the annihilation cross section.

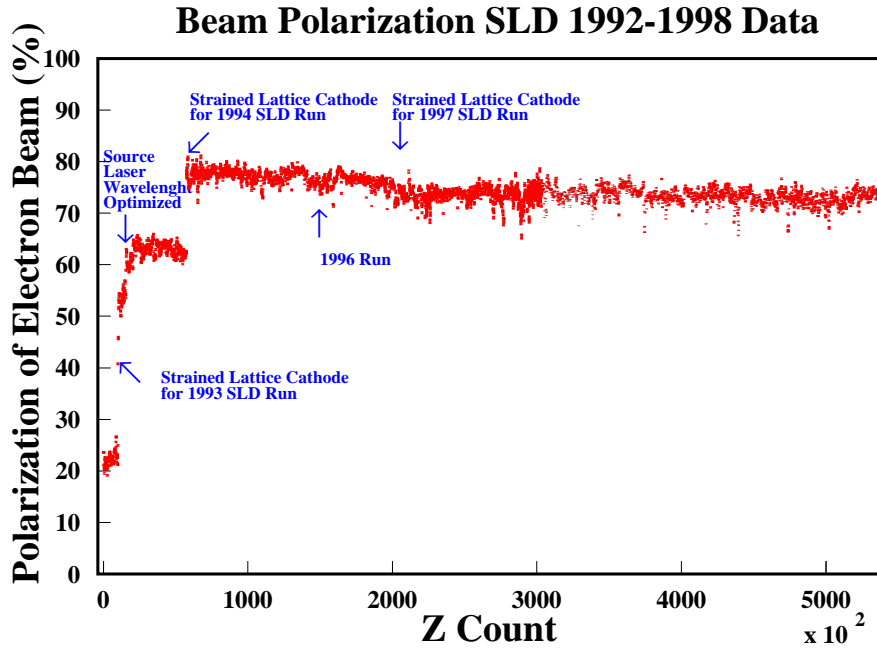


Figure 1.7: The amount of longitudinal electron polarisation as a function of the number of recorded Z decays at SLD.

Left-Right Asymmetry

The left-right asymmetry is an experimentally robust quantity, depending only on event counting:

$$A_{LR} = \frac{N_L - N_R}{N_L + N_R} \frac{1}{\mathcal{P}_e}, \quad (8)$$

where N_L and N_R are the event yields per luminosity unit produced with left- and right-handed polarised electron beams, with the degree of longitudinal polarisation denoted by \mathcal{P}_e . Many systematic effects, such as those affecting acceptance or efficiency, cancel in the ratio. QED radiative corrections ΔA_{LR} are small and calculated to high precision. The corresponding pole quantity A_{LR}^0 is then simply:

$$A_{LR} + \Delta A_{LR} = A_{LR}^0 = \mathcal{A}_e = \frac{2g_{Ve}/g_{Ae}}{1 + (g_{Ve}/g_{Ae})^2}. \quad (9)$$

The left-right asymmetry measurement determines directly the asymmetry parameter \mathcal{A}_f for the initial state fermions. Any final state can be used for the measurement.

The SLD collaboration performed the measurement of A_{LR} with the high-statistics inclusive hadronic channel in order to obtain a high-precision measurement of A_{LR}^0 [71]. Leptonic final states are separated out and used in the independent determination of the left-right forward-backward asymmetry discussed below. The results on A_{LR}^0 for the different data taking periods with their different degree of beam polarisation, compared in Figure 1.8, show reasonable overall consistency.

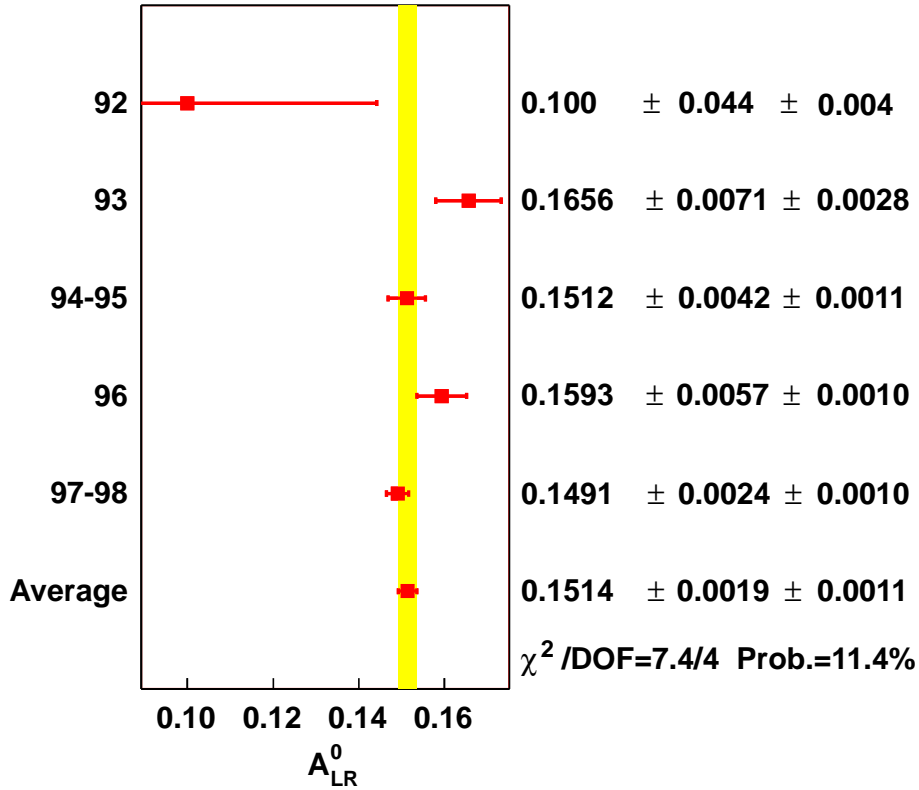


Figure 1.8: A compilation of the published SLD A_{LR}^0 results, ordered by year the data was taken. The final average is calculated including correlations of systematic uncertainties.

The average over the complete SLD data sample, taking correlated uncertainties into account, results in [71]:

$$A_{LR}^0 = 0.1514 \pm 0.0022 \quad (10)$$

or equivalently:

$$\sin^2 \theta_{\text{eff}}^{\text{lept}} = 0.23097 \pm 0.00027. \quad (11)$$

This measurement is the single most precise determination of $\sin^2 \theta_{\text{eff}}^{\text{lept}}$. It is still statistics dominated; the systematic errors included in the total errors listed above are ± 0.0011 and ± 0.00013 , respectively.

Left-Right Forward-Backward Asymmetry

In contrast to the left-right asymmetry, the left-right forward-backward asymmetry determines the asymmetry parameter \mathcal{A}_f specific to the analysed final state:

$$A_{\text{LRFB}}^f = \frac{1}{\mathcal{P}_e} \frac{(N_{F,L} - N_{B,L}) - (N_{F,R} - N_{B,R})}{(N_{F,L} + N_{B,L}) + (N_{F,R} + N_{B,R})} \rightarrow A_{\text{LRFB}}^0 = \frac{3}{4} \mathcal{A}_f, \quad (12)$$

where the subscripts indicate forward and backward events (F, B) accumulated with left- or right-handed electron beams (L, R). Owing to $|\mathcal{P}_e| = 75\%$, the left-right forward-backward asymmetries yield a statistical precision equivalent to measurements of the unpolarised forward-backward asymmetry, $A_{\text{FB}}^{0,f} = (3/4)\mathcal{A}_e\mathcal{A}_f$, using a 25 times larger event sample.

The final states e^+e^- , $\mu^+\mu^-$ and $\tau^+\tau^-$ were used to determine the asymmetry parameter \mathcal{A}_ℓ for the three charged lepton species [75, 76]. For increased statistical precision, the differential distributions in terms of $\cos\theta$, the polar scattering angle, for the left- and right-handed data samples, shown in Figure 1.9, are analysed, allowing a combined determination of both \mathcal{A}_e and \mathcal{A}_f . In case of e^+e^- production, the additional contributions due to t -channel scattering, skewing the differential distribution, are accounted for in the analysis.

Summary

The combined results [69] derived from the measurements of the left-right and left-right forward-backward asymmetries by SLD at SLC are listed in Table 1.2. These results are in good agreement as expected from neutral-current lepton universality. The measurement of \mathcal{A}_e , fully dominated by the A_{LR}^0 result, is by far the most precise determination of any of the \mathcal{A}_ℓ asymmetry parameters. The combined result, assuming lepton universality and accounting for small correlated systematic uncertainties, is:

$$\mathcal{A}_\ell = 0.1513 \pm 0.0021, \quad (13)$$

where the total error includes a systematic error of ± 0.0011 . This measurement is equivalent to a determination of:

$$\sin^2 \theta_{\text{eff}}^{\text{lep}} = 0.23098 \pm 0.00026, \quad (14)$$

where the total error includes a systematic error of ± 0.00013 .

Table 1.2: Results on the leptonic asymmetry parameters \mathcal{A}_ℓ not assuming neutral-current lepton universality obtained at SLD. The result on \mathcal{A}_e includes the result on A_{LR}^0 .

Parameter	Average	Correlations		
		\mathcal{A}_e	\mathcal{A}_μ	\mathcal{A}_τ
\mathcal{A}_e	0.1516 ± 0.0021	1.000		
\mathcal{A}_μ	0.142 ± 0.015	0.038	1.000	
\mathcal{A}_τ	0.136 ± 0.015	0.033	0.007	1.000

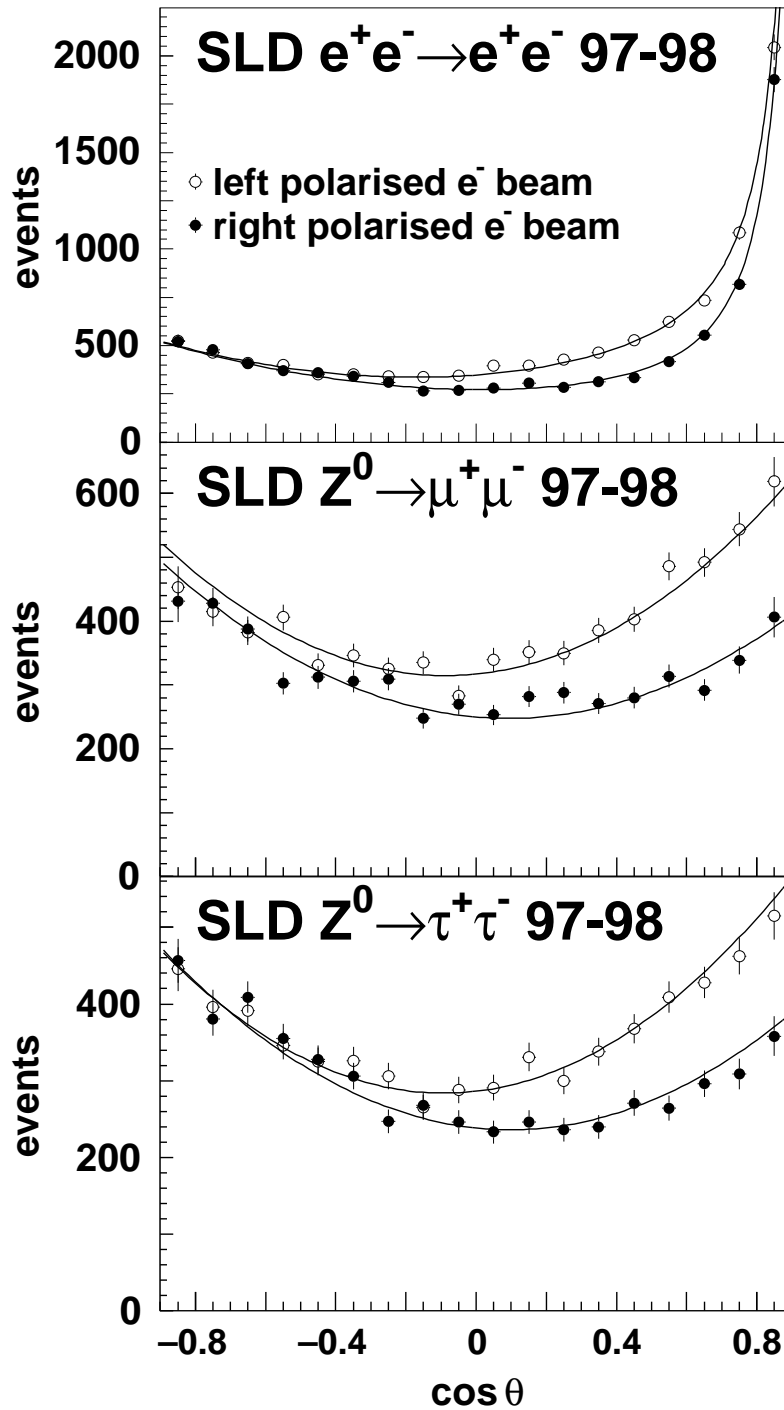


Figure 1.9: Polar-angle distributions for observed for e^+e^- , $\mu^+\mu^-$ and $\tau^+\tau^-$ events selected in the 1997-1998 SLD run. The solid line represents the fit, while the points with error bars show the data in bins of 0.1 in $\cos \theta$. For $|\cos \theta| > 0.7$, the data are corrected for a decrease in the detection efficiency with increasing $|\cos \theta|$.

1.2.4 Tau Polarisation at LEP

Even in case of unpolarised beams, the final-state fermions in $e^+e^- \rightarrow f\bar{f}$ exhibit a non-zero polarisation (average helicity) arising from the parity-violating coupling of the exchanged Z boson to the initial- and final-state fermions. For final-state fermions undergoing charged weak decay, the parity-violating nature of the charged weak decay serves as a polarisation analyser and thus allows to measure the polarisation [77], here in case of $\tau^+\tau^-$ production with subsequent V–A tau decay.

At $\sqrt{s} = m_Z$ and considering only Z-boson exchange, the dependence of the polarisation on the polar scattering angle reads:

$$\mathcal{P}_\tau(\cos\theta_{\tau^-}) = -\frac{\mathcal{A}_\tau(1 + \cos^2\theta_{\tau^-}) + 2\mathcal{A}_e \cos\theta_{\tau^-}}{(1 + \cos^2\theta_{\tau^-}) + \frac{8}{3}A_{\text{FB}}^\tau \cos\theta_{\tau^-}}, \quad (15)$$

where $\mathcal{P}_\tau \equiv \mathcal{P}_{\tau^-} = -\mathcal{P}_{\tau^+}$ since the τ^- and τ^+ have opposite helicities in Z decays. Analysis of the differential distributions allows the separate determination of the asymmetry parameters \mathcal{A}_e and \mathcal{A}_τ . The average polarisation and the forward-backward asymmetry of the polarisation are related to the asymmetry parameters \mathcal{A}_ℓ as:

$$\langle \mathcal{P}_\tau^0 \rangle = -\mathcal{A}_\tau \quad (16)$$

$$A_{\text{FB}}^{\text{pol},0} = -\frac{3}{4}\mathcal{A}_e. \quad (17)$$

The analysis of the differential distribution Equation 15 in terms of both \mathcal{A}_e and \mathcal{A}_τ yields statistically somewhat more precise results on the asymmetry parameters than using just the average polarisation and its forward-backward asymmetry.

Each LEP experiment analysed up to five of the most important τ decay modes with high branching fractions [78, 82, 84, 87]: $\tau \rightarrow \pi\nu$, $\tau \rightarrow \rho\nu$, $\tau \rightarrow a_1\nu$, $\tau \rightarrow e\nu\bar{\nu}$ and $\tau \rightarrow \mu\nu\bar{\nu}$. The tau polarisation affects the distribution of decay angles in the rest frame of the decaying tau lepton, which translates into a polarisation dependent energy spectrum of the decay products in the laboratory or detector system; for example for $\tau \rightarrow \pi\nu$ and $\tau \rightarrow \ell\nu_\ell\nu_\tau$ decays:

$$\frac{1}{\Gamma} \frac{d\Gamma}{dx_\pi} = 1 + \mathcal{P}_\tau(2x_\pi - 1) \quad (18)$$

$$\frac{1}{\Gamma} \frac{d\Gamma}{dx_\ell} = \frac{1}{3} [(5 - 9x_\ell^2 + 4x_\ell^3) + \mathcal{P}_\tau(1 - 9x_\ell^2 + 8x_\ell^3)] , \quad (19)$$

where x denotes the fractional energy E/E_τ of the visible decay product. Distributions of kinematic observables of the visible τ decay products are hence used to measure the polarisation as a function of $\cos\theta$. For multi-hadronic τ decays through intermediate mesons, such as ρ or a_1 , more complicated, so-called optimal observables, ω , are used, which are designed for optimal statistical sensitivity to the tau polarisation [91]. Example distributions are shown in Figure 1.10. The tau polarisation is extracted by fitting a linear combination of positive and negative helicity contributions, obtained from Monte-Carlo simulations [92, 93], to the observed data distribution. The measured values of \mathcal{P}_τ as a function of $\cos\theta_{\tau^-}$ is shown in Figure 1.11.

For the LEP combination [69], each LEP experiment provides a result for \mathcal{A}_e and \mathcal{A}_τ , which are already averaged over the experiment's analyses [78, 82, 84, 87]. These results are reported in Table 1.3 and compared in Figure 1.12, showing that the results from the different experiments agree well.

Systematic errors are summarised in Table 1.4; they are generally much smaller for \mathcal{A}_e than for \mathcal{A}_τ , as \mathcal{A}_e is equivalent to a forward-backward asymmetry of the $\cos\theta$ dependent tau polarisation, whereas \mathcal{A}_τ is given by the average tau polarisation. The systematic uncertainty labelled ZFITTER includes decay-independent systematic uncertainties arising from corrections of the experimental

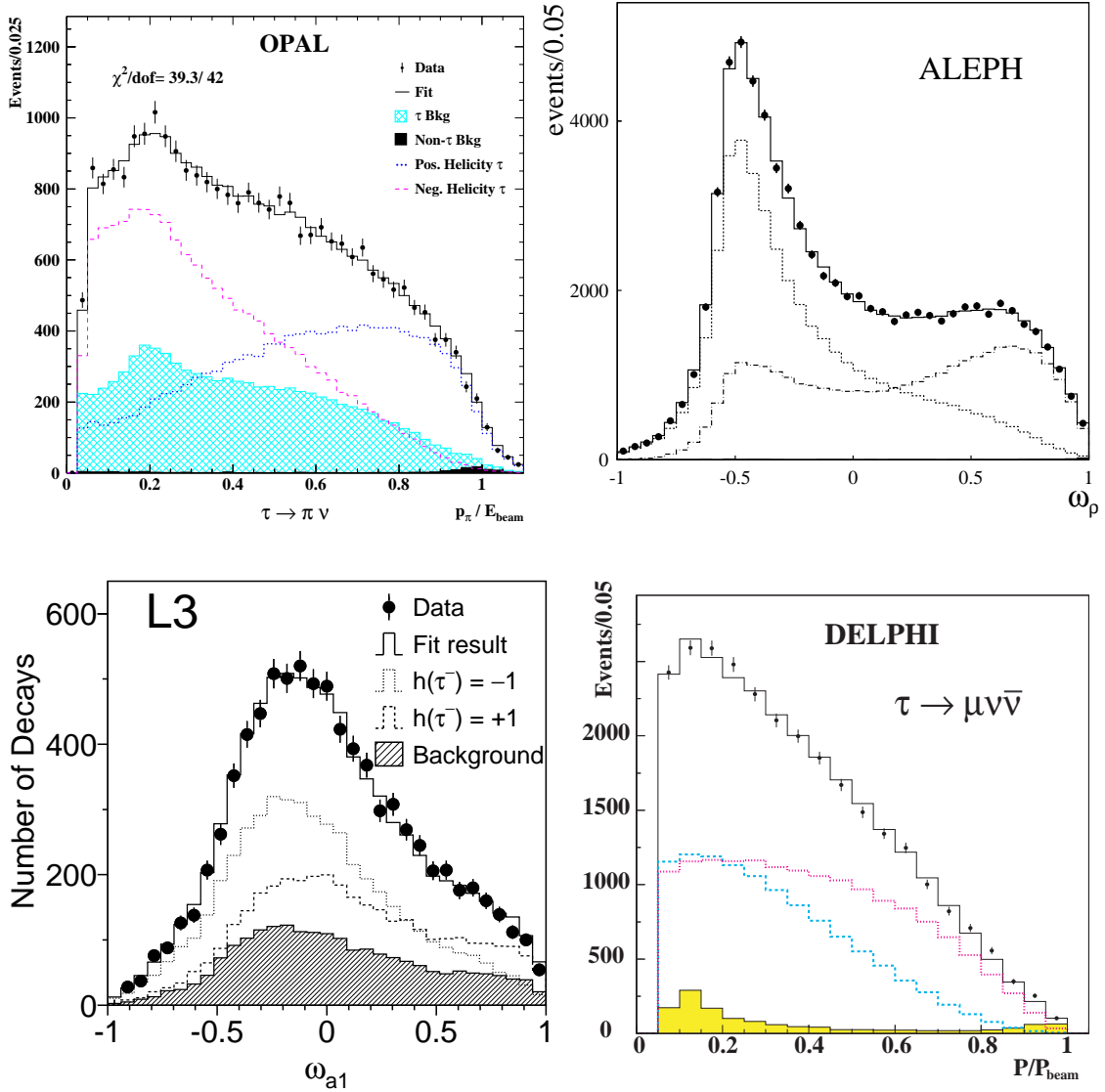


Figure 1.10: The measured distributions in the polarisation-sensitive variable for the $\tau \rightarrow \pi \nu$ decays (OPAL), $\tau \rightarrow \rho \nu$ decays (ALEPH), $\tau \rightarrow a_1 \nu$ decays (L3) and $\tau \rightarrow \mu \nu \bar{\nu}$ decays (DELPHI), in each case integrated over the whole $\cos \theta_{\tau^-}$ range, with ω denoting the relevant optimal observable as discussed in the text. Overlaying this distribution are Monte Carlo distributions for the two helicity states, and for their sum including background, assuming a value for $\langle \mathcal{P}_\tau \rangle$ equal to the fitted polarisation.

distributions to the pole quantities \mathcal{A}_e and \mathcal{A}_τ , such as QED radiative corrections, energy dependence of the tau polarisation, and mass effects leading to helicity flips. These uncertainties are calculated with ZFITTER and are treated as fully correlated between all decay channels and all experiments in the combination. The remaining systematic errors are dependent on the specific tau decay mode analysed and are thus treated as uncorrelated between different decay modes but as

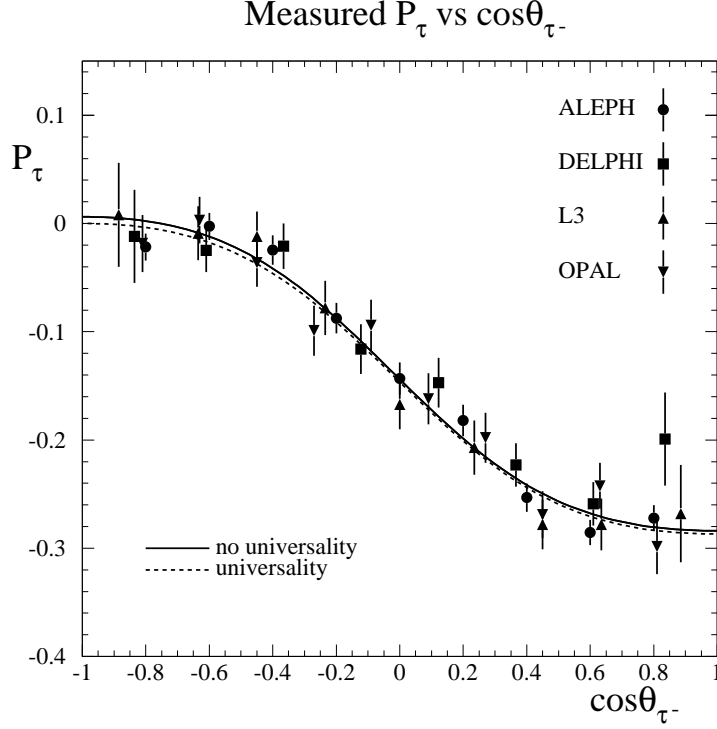


Figure 1.11: The values of \mathcal{P}_τ as a function of $\cos\theta_{\tau^-}$ as measured by each of the LEP experiments. Only the statistical errors are shown. The values are not corrected for radiation, interference or pure photon exchange. The solid curve overlays Equation 15 for the LEP values of \mathcal{A}_τ and \mathcal{A}_e . The dashed curve overlays Equation 15 under the assumption of lepton universality for the LEP value of \mathcal{A}_ℓ .

correlated between experiments. These errors describe the dependence on tau branching fractions taken from References [94, 95], affecting the purity of the data sample, the contamination of the selected samples by background processes, mainly arising from two-photon collision processes, and the modelling of the specific decay in hadronic tau decays [96, 97]. In all cases, the systematic errors are much smaller than the statistical errors.

The combined LEP results for \mathcal{A}_e and \mathcal{A}_τ are:

$$\mathcal{A}_\tau = 0.1439 \pm 0.0043 \quad (20)$$

$$\mathcal{A}_e = 0.1498 \pm 0.0049, \quad (21)$$

where the average has a χ^2 of 3.9 for six degrees of freedom. The correlation between the results is +0.012. The uncertainties of both averages are still dominated by statistics, in particular for \mathcal{A}_e , being related to the forward-backward asymmetry of the tau polarisation. The results are in good agreement with each other, as expected from neutral-current lepton universality. Assuming $e - \tau$ universality, a combined value of:

$$\mathcal{A}_\ell = 0.1465 \pm 0.0033, \quad (22)$$

is obtained, where the total error contains a systematic error of 0.0015. The χ^2 of this average is 4.7 for seven degrees of freedom. The above value of \mathcal{A}_ℓ corresponds to:

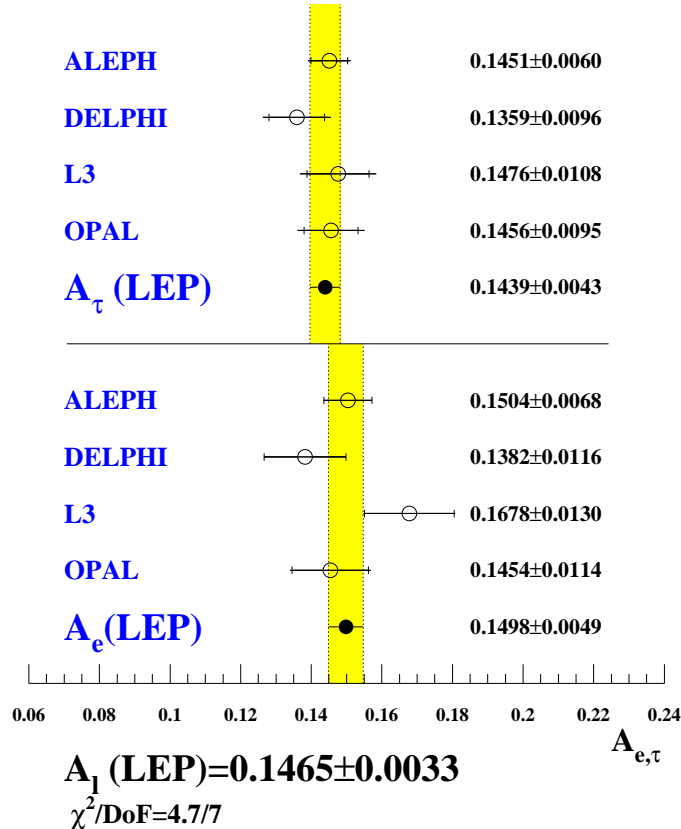
$$\sin^2 \theta_{\text{eff}}^{\text{lept}} = 0.23159 \pm 0.00041. \quad (23)$$

Table 1.3: LEP results for \mathcal{A}_τ and \mathcal{A}_e . The first error is statistical and the second systematic.

Experiment	\mathcal{A}_τ	\mathcal{A}_e
ALEPH	$0.1451 \pm 0.0052 \pm 0.0029$	$0.1504 \pm 0.0068 \pm 0.0008$
DELPHI	$0.1359 \pm 0.0079 \pm 0.0055$	$0.1382 \pm 0.0116 \pm 0.0005$
L3	$0.1476 \pm 0.0088 \pm 0.0062$	$0.1678 \pm 0.0127 \pm 0.0030$
OPAL	$0.1456 \pm 0.0076 \pm 0.0057$	$0.1454 \pm 0.0108 \pm 0.0036$
LEP	$0.1439 \pm 0.0035 \pm 0.0026$	$0.1498 \pm 0.0048 \pm 0.0009$

Table 1.4: The magnitude of the major common systematic errors on \mathcal{A}_τ and \mathcal{A}_e by category for each of the LEP experiments.

	ALEPH		DELPHI		L3		OPAL	
	$\delta\mathcal{A}_\tau$	$\delta\mathcal{A}_e$	$\delta\mathcal{A}_\tau$	$\delta\mathcal{A}_e$	$\delta\mathcal{A}_\tau$	$\delta\mathcal{A}_e$	$\delta\mathcal{A}_\tau$	$\delta\mathcal{A}_e$
ZFITTER	0.0002	0.0002	0.0002	0.0002	0.0002	0.0002	0.0002	0.0002
τ branching fractions	0.0003	0.0000	0.0016	0.0000	0.0007	0.0012	0.0011	0.0003
two-photon bg	0.0000	0.0000	0.0005	0.0000	0.0007	0.0000	0.0000	0.0000
had. decay model	0.0012	0.0008	0.0010	0.0000	0.0010	0.0001	0.0025	0.0005

Figure 1.12: Measurements of \mathcal{A}_τ and \mathcal{A}_e from the four LEP experiments and the combined values. The error bars indicate the total errors. The magnitude of the statistical error alone is indicated by the small tick marks on each error bar.

1.2.5 Heavy Quark Flavours b and c

Introduction

The Z lineshape analyses in the inclusive hadronic channel as discussed in Section 1.2.2 do not separate the different quark flavours, hence do not allow the determination of individual quark couplings. In contrast, this section describes the complex analyses required in order to isolate samples of specific quark flavor, namely containing the heavy hadrons containing b and c quarks arising in $b\bar{b}$ and $c\bar{c}$ production [69]. These data samples allow the determination of electroweak observables similar to those discussed in the previous sections, namely:

$$R_q^0 = \frac{\Gamma_{q\bar{q}}}{\Gamma_{\text{had}}} \quad (24)$$

$$A_{\text{FB}}^{0,q} = \frac{3}{4} \mathcal{A}_c \mathcal{A}_q \quad (25)$$

$$A_{\text{LRFB}}^q = \frac{3}{4} \mathcal{A}_q, \quad (26)$$

for the quark flavours $q = b, c$. The quantities R_q^0 are measured by SLD and at LEP, $A_{\text{FB}}^{0,q}$ is measured at LEP, and A_{LRFB}^q is measured by SLD.

Tagging Methods

Hadrons containing heavy quarks are identified experimentally by their high mass, semileptonic decay modes, fully or partially reconstructed decays, or long lifetime leading to secondary decay vertices and high impact parameter tracks. Distributions of several tagging observables [98, 99, 100, 101, 102, 103, 104], comparing heavy quarks samples with light quark background, are shown in Figure 1.13. The impact parameter is the distance of closest approach of a track to the reconstructed interaction point or primary vertex, and is thus large for tracks originating from the decay of long-lived hadrons. In case the secondary decay vertex is reconstructed, the significance of its distance from the primary production vertex is again large for long-lived hadrons containing heavy quarks. In case the decay vertex is measured, the mass of the decaying object is reconstructed using a pseudo-mass technique, and used to check whether it is compatible with a heavy objects. Semileptonic decays of heavy hadrons produce leptons with high total momentum as well as high momentum transverse to the jet containing the decaying hadron. As an example, the performance of the combined tagging algorithms used in the R_b analyses is reported in Table 1.5 for the five experiments. The small beam pipe and low repetition rate of SLC allows the SLD experiment to employ detector systems reaching superior tagging performance.

Table 1.5: Tagging performance of the different experiments as used for the R_b analyses.

	ALEPH	DELPHI	L3	OPAL	SLD
b Purity [%]	97.8	98.6	84.3	96.7	98.3
b Efficiency [%]	22.7	29.6	23.7	25.5	61.8

Partial Width Measurements

Each tagging method, applied to a hadronic jet or event hemisphere, identifies the underlying quark flavor with a certain efficiency, tuned to be high for b and c quarks but low for uds quarks.

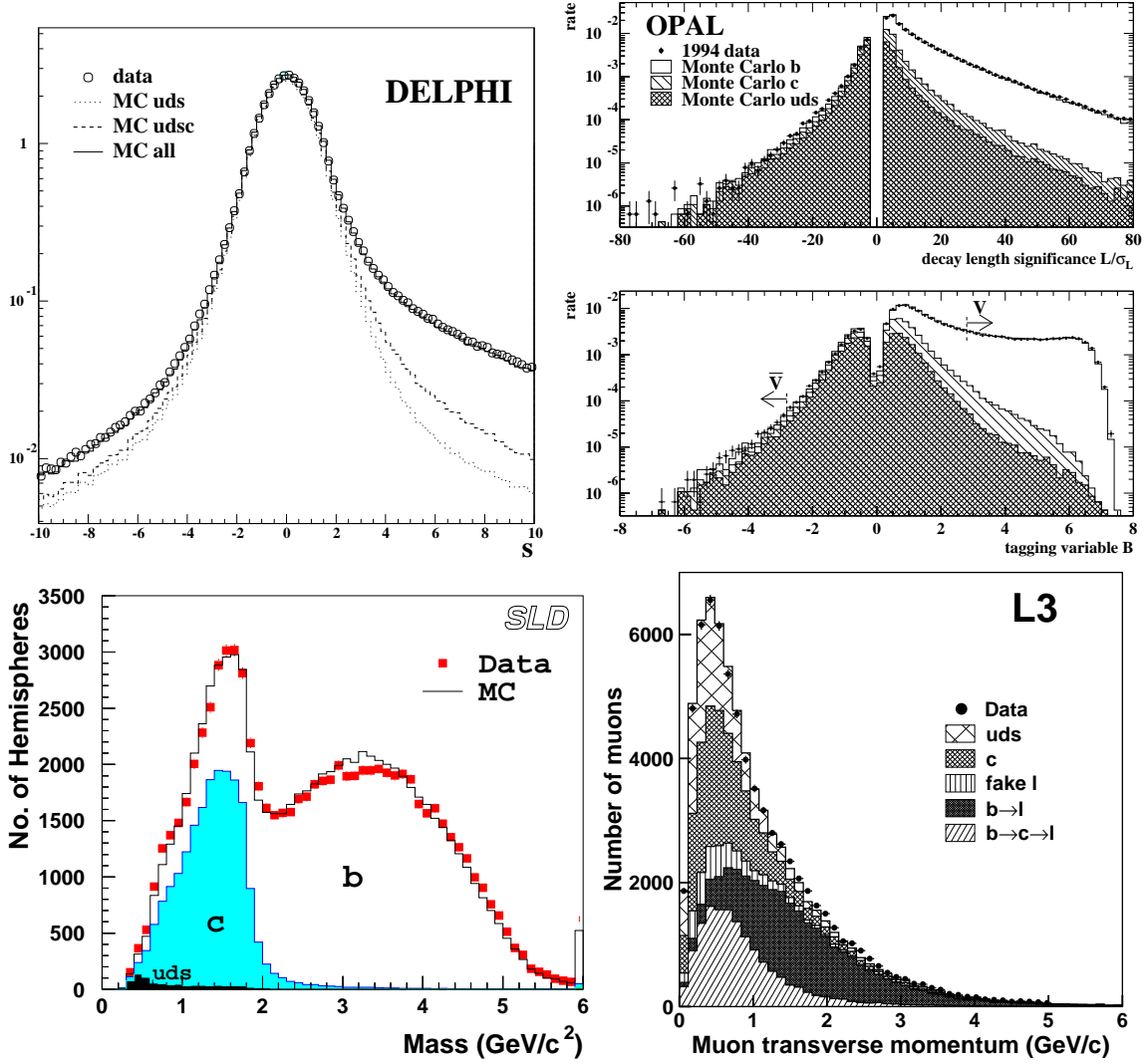


Figure 1.13: Distribution of tagging variables. Top left: impact parameter significance; top right: decay length significance and neural-net tagging output; bottom left: vertex mass; bottom right: transverse momentum of inclusive muon arising from the decay of b- and c-flavour hadrons transverse to the containing jet. Monte Carlo contributions are separated according to different quark flavours.

Since there are two jets or hemispheres in each event, the fraction of events with a single tag and a double tag are expressed as:

$$\begin{aligned} f_s &= \varepsilon_b R_b + \varepsilon_c R_c + \varepsilon_{uds}(1 - R_b - R_c) \\ f_d &= \varepsilon_b^{(d)} R_b + \varepsilon_c^{(d)} R_c + \varepsilon_{uds}^{(d)}(1 - R_b - R_c), \end{aligned} \quad (27)$$

where ε_f is the tagging efficiency for quark flavour f . The double-tagging efficiency $\varepsilon_f^{(d)}$ is written as

$$\varepsilon_f^{(d)} = (1 + \mathcal{C}_f)\varepsilon_f^2 \quad (28)$$

where the correction factor $\mathcal{C}_f \neq 0$ accounts for the the two hemispheres in an event being somewhat correlated. Neglecting correlations and backgrounds, one finds $R_b = f_s^2/f_d$ independent of ε_b , ie, a robust measurement. However, the neglected terms are not small and must be determined from Monte Carlo simulations, leading to model dependencies and thus correlated systematic uncertainties affecting the measurements. In multi-tag methods, several different tagging algorithms are used simultaneously, leading to a system of linear equations similar to the above which is overconstrained and allows the extraction of rates as well as several efficiencies from the data, resulting in reduced model dependence. Further details on the various measurements of the five experiments are given in [105, 100, 102, 103, 106] for R_b and in [107, 108, 107, 109, 110, 109, 111, 112, 106] for R_c .

Asymmetry Measurements

The asymmetry measurements are performed by analysing the event rate as a function of the polar angle of the event thrust axis. This in turn requires the assignment of a charge to a quark jet or event hemisphere. The measured asymmetry is given by:

$$A_{\text{FB}}^{\text{meas}} = \sum_{\text{q}} (2\omega_{\text{q}} - 1)\eta_{\text{q}}A_{\text{FB}}^{\text{q}\bar{\text{q}}}, \quad (29)$$

where η_{q} is the fraction of $\text{q}\bar{\text{q}}$ events in the sample, ω_{q} is the probability to tag the quark charge correctly, and the sum is taken over all quark flavours.

Various charge tagging methods are employed by the five experiments. For heavy quarks decaying semileptonically, the charge of the lepton is correlated with the charge of the decaying heavy quark. Independent of decay mode, the jet or vertex charge is used, constructed as the momentum weighted sum of charges of tracks belonging to the jet or the identified secondary decay vertex:

$$Q_h = \frac{\sum_i q_i p_{\parallel i}^{\kappa}}{\sum_i p_{\parallel i}^{\kappa}}, \quad (30)$$

and where p_{\parallel} is the momentum of the track along the thrust axis, and κ is a tunable parameter with typical values between 0.3 and 1.

A precise measurement of an asymmetry requires good charge separation (for example, semileptonic decays, which however are limited by their branching fractions) and/or high statistics (jet/vertex charge which, however, has a worse charge separation). As an example, the charge separation δ_{q} for $\text{b}\bar{\text{b}}$ events achieved by ALEPH is shown in Figure 1.14, where:

$$\begin{aligned} \langle Q_{\text{FB}} \rangle &= \langle Q_{\text{F}} - Q_{\text{B}} \rangle = \delta_{\text{q}} A_{\text{FB}}^{\text{q}\bar{\text{q}}} \\ \delta_{\text{q}} &= \langle Q_{\text{q}} - Q_{\bar{\text{q}}} \rangle, \end{aligned}$$

which is largely measured from data, for example:

$$\left(\frac{\delta_{\text{q}}}{2}\right)^2 = \frac{\langle Q_{\text{F}} \cdot Q_{\text{B}} \rangle + \rho_{\text{q}\bar{\text{q}}}\sigma(Q)^2 + \mu(Q)^2}{1 + \rho_{\text{q}\bar{\text{q}}}}, \quad (31)$$

where $\mu(Q)$ is the mean value of Q for all hemispheres and $\sigma(Q)$ is its variance. Note that $\mu(Q)$ is slightly positive due to an excess of positive hadrons in secondary hadronic interactions. Only the hemisphere correlations, $\rho_{\text{q}\bar{\text{q}}}$, which arise from charge conservation, hard gluon radiation and other small effects, must be taken from simulation.

The resulting differential distributions in polar angle are shown in Figures 1.15 and 1.16 for the forward-backward and left-right forward-backward asymmetry in $\text{b}\bar{\text{b}}$ production, respectively.

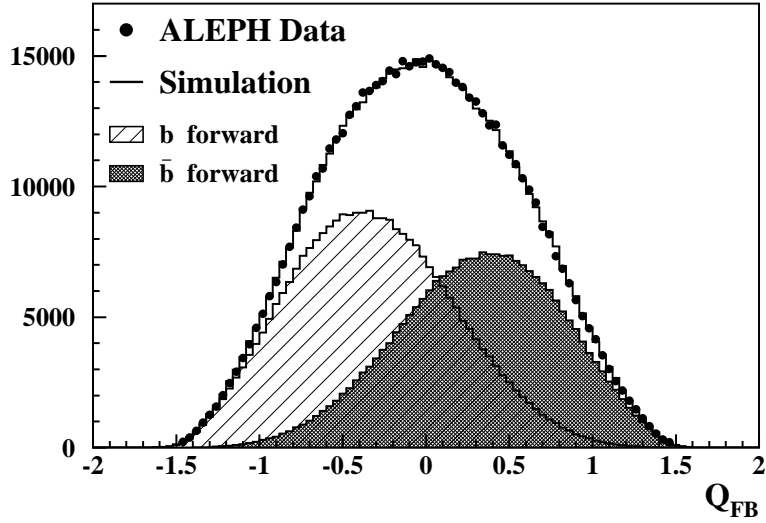


Figure 1.14: Charge separation of the ALEPH neural net tag using jet charge, vertex charge and charged kaons [113]. The asymmetry reflects $A_{\text{FB}}^{\text{b}\bar{\text{b}}}$ diluted by the non-perfect charge tagging.

These distributions, evaluated in terms of the expected asymmetries between bins at $\pm \cos \theta$:

$$A_{\text{FB}}^{\text{q}\bar{\text{q}}}(\cos \theta) = \frac{8}{3} A_{\text{FB}}^{\text{q}\bar{\text{q}}} \frac{\cos \theta}{1 + \cos^2 \theta} \quad (32)$$

$$A_{\text{LRFB}}^{\text{q}\bar{\text{q}}}(\cos \theta) = |\mathcal{P}_e| \mathcal{A}_q \frac{2 \cos \theta}{1 + \cos^2 \theta}, \quad (33)$$

allow to determine $A_{\text{FB}}^{0;\text{q}}$ and \mathcal{A}_q , respectively. The analyses of the four LEP experiments are described in detail in [114, 113, 115, 117, 118, 119, 121, 122, 123, 124] for b quarks, and in [114, 125, 115, 117, 119, 123, 124] for c quarks, while the SLD results for the polarised asymmetries are described in [126, 128, 130, 131] and in [126, 132, 131], respectively.

Corrections and Systematic Uncertainties

The various flavour and charge tagging analyses necessarily depend on assumptions about the fragmentation of heavy quarks and decays of hadrons containing these quarks. This leads to non-trivial correlations between the results of the LEP and SLD experiments, which have to be taken into account in a combination, as well as to a dependence on additional model parameters. In order to derive consistent and correct averages in a fit to the experimental results, the five experiments have agreed on a common set of values for external parameters and their associated uncertainties. The associated uncertainties are propagated to all results using parametrised dependencies.

Additional observables besides the six electroweak observables are included in the combination procedure as well in case they are also measured by the five experiments and correlated to the main analyses. These additional fit parameters are:

- the probability that a c-quark fragments into a D^{*+} that decays into $D^0 \pi^+$: $P(c \rightarrow D^{*+}) \times B(D^{*+} \rightarrow \pi^+ D^0)$, denoted $P(c \rightarrow D^{*+} \rightarrow \pi^+ D^0)$ in the following,
- the fraction of charm hemispheres fragmenting into a specified weakly-decaying charmed hadron: $f(D^+)$, $f(D_s)$, $f(c_{\text{baryon}})$,³

³ The quantity $f(D^0)$ is calculated from the constraint $f(D^0) + f(D^+) + f(D_s) + f(c_{\text{baryon}}) = 1$.

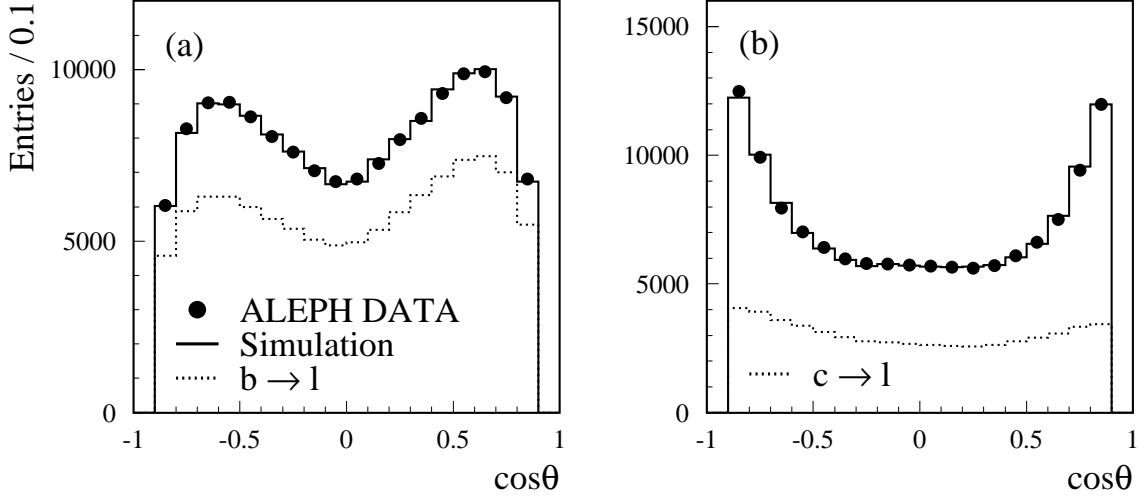


Figure 1.15: Reconstructed $\cos\theta$ distribution from the ALEPH asymmetry measurements with leptons for a) the b-enriched and b) the c-enriched sample [114]. The full histogram shows the expected raw angular distribution in the simulation. The dashed histogram show the signal component.

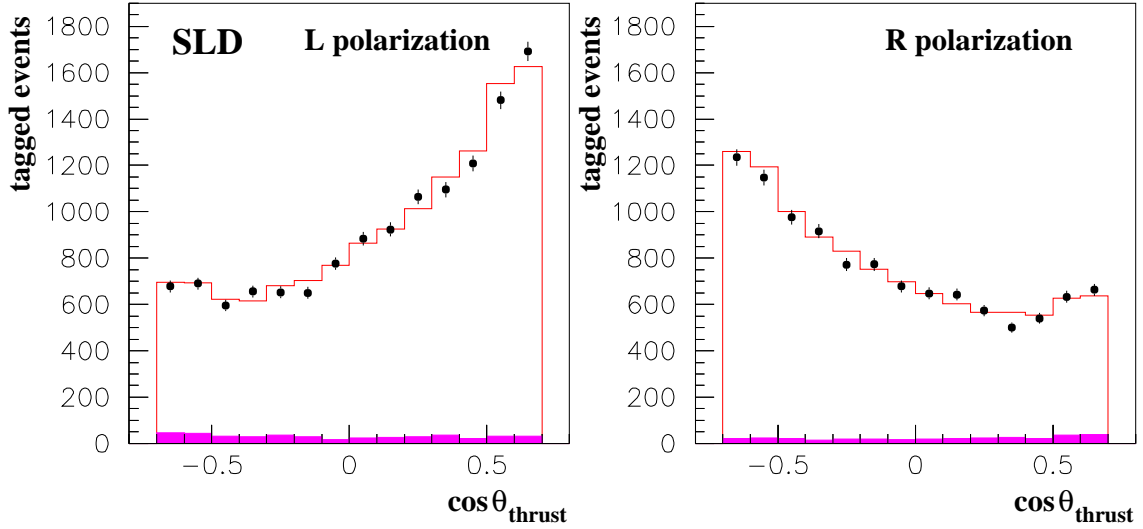


Figure 1.16: Reconstructed $\cos\theta$ distributions from the SLD vertex charge \mathcal{A}_b analysis for events with left-handed and right-handed electron beam polarisations. The shaded region corresponds to the $uds c$ background in the sample estimated from Monte Carlo.

- the prompt and cascade semileptonic branching fraction of the b-hadrons $B(b \rightarrow \ell^-)^4$ and $B(b \rightarrow c \rightarrow \ell^+)$ and the prompt semileptonic branching fraction of the c-hadrons $B(c \rightarrow \ell^+)$,
- the $B^0\bar{B}^0$ effective mixing parameter $\bar{\chi}$, which is the probability that a semileptonically decaying b-quark has been produced as an anti-b-quark.

⁴ Unless otherwise stated, charge conjugate modes are always included.

Small corrections have to be applied to the raw experimental results. The R_b and R_c analyses measure ratios of production rates, $R_q = \sigma_{q\bar{q}}/\sigma_{\text{had}}$. To obtain the ratios of partial widths $R_q^0 = \Gamma_{q\bar{q}}/\Gamma_{\text{had}}$, corrections for photon exchange and γ - Z interference must be applied. These corrections are small, typically $+0.0002$ for R_b and -0.0002 for R_c depending slightly on the invariant mass cutoff of the $q\bar{q}$ -system imposed in the analysis. Corrections of similar origin have to be applied to the asymmetries, as even the data denoted “peak”, taken at the maximum annihilation cross section, is at a \sqrt{s} value slightly different from m_Z while the asymmetries are strongly varying as a function of energy. These corrections on the asymmetries are summarised in Table 1.6.

Table 1.6: Corrections to be applied to the quark asymmetries as $A_{\text{FB}}^{0,q} = A_{\text{FB}}^{\text{q}\bar{\text{q}}}(\text{pk}) + \delta A_{\text{FB}}$. The row labelled “other” denotes corrections due to γ exchange, γ - Z interference, quark-mass effects and imaginary parts of the couplings. The uncertainties of the corrections are negligible.

Source	$\delta A_{\text{FB}}^{\text{b}\bar{\text{b}}}$	$\delta A_{\text{FB}}^{\text{c}\bar{\text{c}}}$
$\sqrt{s} = m_Z$	-0.0014	-0.0035
QED corrections	+0.0039	+0.0107
other	-0.0006	-0.0008
Total	+0.0019	+0.0064

However, for the asymmetries, the largest corrections are those for QCD effects, which are, in contrast to the case of partial widths, by construction not absorbed in the definition of the electroweak asymmetry parameters. The dominant QCD corrections arise from gluon radiation and depend on whether the jet axis or thrust axis is used to determine the polar angle in the analysis. The QCD corrections on the asymmetries are written as follows [133]:

$$\begin{aligned} \left(A_{\text{FB}}^{\text{q}\bar{\text{q}}}\right)_{\text{meas}} &= (1 - C_{\text{QCD}}) \left(A_{\text{FB}}^{\text{q}\bar{\text{q}}}\right)_{\text{no QCD}} \\ &= \left(1 - \frac{\alpha_s(m_Z^2)}{\pi} c_1 - \left(\frac{\alpha_s(m_Z^2)}{\pi}\right)^2 c_2\right) \left(A_{\text{FB}}^{\text{q}\bar{\text{q}}}\right)_{\text{no QCD}} . \end{aligned} \quad (34)$$

The first-order corrections are known including mass effects [134]. Taking the thrust axis as the direction and using the pole mass, they are $c_1 = 0.77$ for $A_{\text{FB}}^{\text{b}\bar{\text{b}}}$ and $c_1 = 0.86$ for $A_{\text{FB}}^{\text{c}\bar{\text{c}}}$. The second-order corrections have been recalculated in [135] and [136]; the second order coefficients used are $c_2 = 5.93$ for $A_{\text{FB}}^{\text{b}\bar{\text{b}}}$ and $c_2 = 8.5$ for $A_{\text{FB}}^{\text{c}\bar{\text{c}}}$. The final QCD correction coefficients, including further corrections due to fragmentation effects and using the thrust axis as reference direction ($C_{\text{QCD}}^{\text{had,T}}$), are $C_{\text{QCD}}^{\text{had,T}} = 0.0354 \pm 0.0063$ for $A_{\text{FB}}^{\text{b}\bar{\text{b}}}$ and $C_{\text{QCD}}^{\text{had,T}} = 0.0413 \pm 0.0063$ for $A_{\text{FB}}^{\text{c}\bar{\text{c}}}$. The breakdown of the errors relating to the QCD corrections is given in Table 1.7.

Table 1.7: Error sources for the QCD corrections to the forward-backward asymmetries.

Error on $C_{\text{QCD}}^{\text{had,T}}$		$\text{b}\bar{\text{b}}$	$\text{c}\bar{\text{c}}$
Higher orders [136]		0.0025	0.0046
Mass effects [133]		0.0015	0.0008
Higher order mass [136]		0.005	0.002
$\alpha_s = 0.119 \pm 0.003$		0.0012	0.0015
Hadronisation [133]		0.0023	0.0035
Total		0.0063	0.0063

Table 1.8: The dominant error sources for the heavy-flavour electroweak parameters from the 14-parameter fit, see text for details. The total systematic error is separated into a contribution uncorrelated between the measurements, and in several components which are correlated between measurements, as resulting from the combination procedure.

Source	R_b^0 [10^{-3}]	R_c^0 [10^{-3}]	$A_{\text{FB}}^{0,b}$ [10^{-3}]	$A_{\text{FB}}^{0,c}$ [10^{-3}]	\mathcal{A}_b [10^{-2}]	\mathcal{A}_c [10^{-2}]
statistics	0.44	2.4	1.5	3.0	1.5	2.2
internal systematics	0.28	1.2	0.6	1.4	1.2	1.5
QCD effects	0.18	0	0.4	0.1	0.3	0.2
$B(D \rightarrow \text{neut.})$	0.14	0.3	0	0	0	0
D decay multiplicity	0.13	0.6	0	0.2	0	0
B decay multiplicity	0.11	0.1	0	0.2	0	0
$B(D^+ \rightarrow K^- \pi^+ \pi^+)$	0.09	0.2	0	0.1	0	0
$B(D_s \rightarrow \phi \pi^+)$	0.02	0.5	0	0.1	0	0
$B(\Lambda_c \rightarrow p K^- \pi^+)$	0.05	0.5	0	0.1	0	0
D lifetimes	0.07	0.6	0	0.2	0	0
B decays	0	0	0.1	0.4	0	0.1
decay models	0	0.1	0.1	0.5	0.1	0.1
non incl. mixing	0	0.1	0.1	0.4	0	0
gluon splitting	0.23	0.9	0.1	0.2	0.1	0.1
c fragmentation	0.11	0.3	0.1	0.1	0.1	0.1
light quarks	0.07	0.1	0	0	0	0
beam polarisation	0	0	0	0	0.5	0.3
total correlated	0.42	1.5	0.4	0.9	0.6	0.4
total error	0.66	3.0	1.6	3.5	2.0	2.7

The dominant sources of systematic errors in the determination of the six electroweak observables are reported in Table 1.8. For the two partial width observables, the systematic errors are of similar size to the statistical errors. In contrast, the four asymmetry measurements are by far statistically dominated.

Combined Results

The heavy flavour results are combined using a χ^2 minimisation [137]. In a first analysis to the set of experimental results, the forward-backward asymmetry measurements at LEP are corrected to three common centre-of-mass energy points, corresponding to the “peak” of the Z resonance curve, and “peak ± 2 GeV” [69]. The asymmetry measurements are compared to the expectation as a function of \sqrt{s} in Figure 1.17. Good agreement with the expected \sqrt{s} dependence is observed.

In a second analysis, the off-peak forward-backward asymmetry measurements are all transported to the “peak” centre-of-mass energy [69]. The peak asymmetries in $b\bar{b}$ and $c\bar{c}$ production are then corrected [138] to the corresponding pole quantity $A_{\text{FB}}^{0,q}$ using ZFITTER, recall Table 1.6. The results of the corresponding 14-parameter fit are reported in Tables 1.9 and 1.10.

The main measurements of the experiments used in the determination of the six electroweak observables are compared in Figures 1.18 to 1.20. For each electroweak observable, the measurements of the five experiments are very consistent. This is also reflected in the overall χ^2 of the fit, which is 53 for 105 – 14 degrees of freedom. The small χ^2/dof is largely a result of statistical effects and

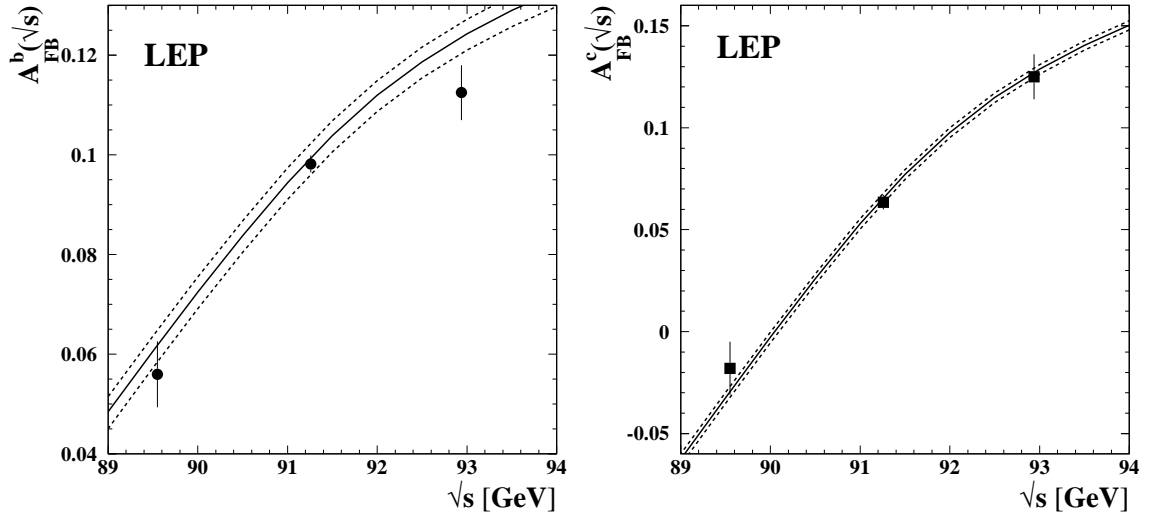


Figure 1.17: Dependence of A_{FB}^b and A_{FB}^c on the centre-of-mass energy \sqrt{s} . The solid line represents the SM prediction for $m_t = 178$ GeV, $m_H = 300$ GeV, the upper (lower) dashed line is the prediction for $m_H = 100$ (1000) GeV. The measurements are shown for the three main energies.

systematic errors evaluated conservatively. For example, the forward-backward asymmetry measurements, all statistically dominated, show very consistent central values. For the partial width measurements, several systematic uncertainties are evaluated by comparing test quantities between data as well as between model simulations. Even if no effect is found or expected, the statistical errors of these tests are taken as systematic uncertainties.

The consistency of the combined results with the expectations calculated within the SM is shown in Figures 1.21 and 1.22, including the consistency between the forward-backward and forward-backward left-right asymmetry results. Note that the asymmetries are in perfect agreement with the SM expectation for high masses of the Higgs boson, in contrast to the leptonic quantities discussed in the previous sections which prefer a much lower Higgs-boson mass. This different behaviour has consequences for joint analyses of all results as presented in Sections 1.2.7 and 1.6.

Table 1.9: The results of the 14-parameter fit to the LEP/SLD heavy flavour data.

Observable	Result
R_b^0	0.21629 ± 0.00066
R_c^0	0.1721 ± 0.0030
$A_{\text{FB}}^{0,b}$	0.0992 ± 0.0016
$A_{\text{FB}}^{0,c}$	0.0707 ± 0.0035
\mathcal{A}_b	0.923 ± 0.020
\mathcal{A}_c	0.670 ± 0.027
$B(b \rightarrow \ell^-)$	0.1071 ± 0.0022
$B(b \rightarrow c \rightarrow \ell^+)$	0.0801 ± 0.0018
$B(c \rightarrow \ell^+)$	0.0969 ± 0.0031
$\bar{\chi}$	0.1250 ± 0.0039
$f(D^+)$	0.235 ± 0.016
$f(D_s)$	0.126 ± 0.026
$f(c_{\text{baryon}})$	0.093 ± 0.022
$P(c \rightarrow D^{*+} \rightarrow \pi^+ D^0)$	0.1622 ± 0.0048

Table 1.10: The correlation matrix for the set of the 14 heavy flavour parameters. $B(1)$, $B(2)$ and $B(3)$ denote $B(b \rightarrow \ell^-)$, $B(b \rightarrow c \rightarrow \ell^+)$ and $B(c \rightarrow \ell^+)$ respectively, P denotes $P(c \rightarrow D^{*+} \rightarrow \pi^+ D^0)$.

	R_b	R_c	$A_{FB}^{0,b}$	$A_{FB}^{0,c}$	\mathcal{A}_b	\mathcal{A}_c	$B(1)$	$B(2)$	$B(3)$	$\bar{\chi}$	$f(D^+)$	$f(D_s)$	$f(c_{bar.})$	P
R_b	1.00													
R_c	-0.18	1.00												
$A_{FB}^{0,b}$	-0.10	0.04	1.00											
$A_{FB}^{0,c}$	0.07	-0.06	0.15	1.00										
\mathcal{A}_b	-0.08	0.04	0.06	-0.02	1.00									
\mathcal{A}_c	0.04	-0.06	0.01	0.04	0.11	1.00								
$B(1)$	-0.08	0.05	-0.01	0.18	-0.02	0.02	1.00							
$B(2)$	-0.03	-0.01	-0.06	-0.23	0.02	-0.04	-0.24	1.00						
$B(3)$	0.00	-0.30	0.00	-0.21	0.03	-0.02	0.01	0.10	1.00					
$\bar{\chi}$	0.00	0.02	0.11	0.08	0.06	0.00	0.29	-0.23	0.16	1.00				
$f(D^+)$	-0.15	-0.10	0.01	-0.04	0.00	0.00	0.04	0.02	0.00	0.02	1.00			
$f(D_s)$	-0.03	0.13	0.00	-0.02	0.00	0.00	0.01	0.00	-0.01	-0.01	-0.40	1.00		
$f(c_{bar.})$	0.11	0.18	-0.01	0.04	0.00	0.00	-0.02	-0.01	-0.02	0.00	-0.24	-0.49	1.00	
P	0.13	-0.43	-0.02	0.04	-0.02	0.02	-0.01	0.01	0.13	0.00	0.08	-0.06	-0.14	1.00

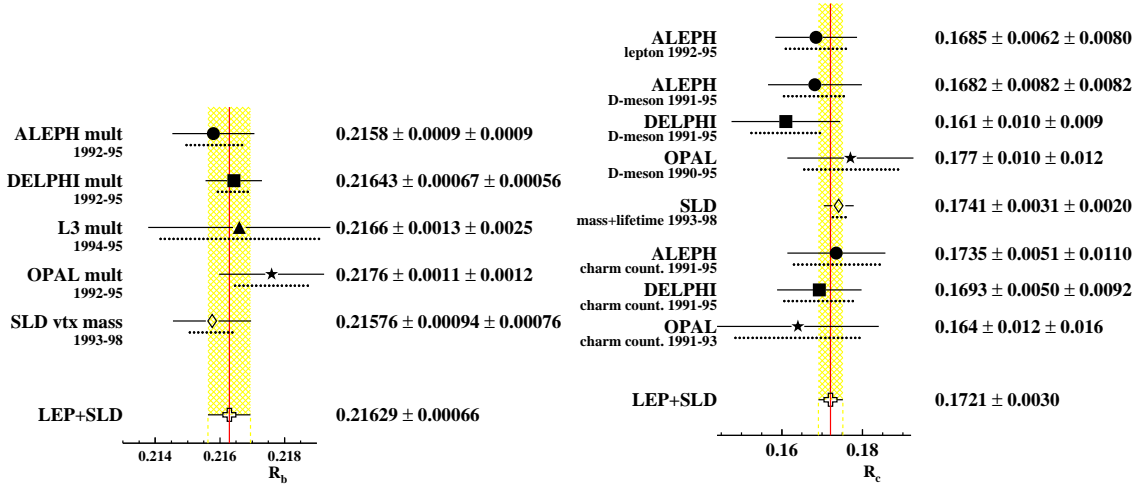


Figure 1.18: R_b^0 and R_c^0 measurements used in the heavy flavour combination, corrected for their dependence on parameters evaluated in the multi-parameter fit described in the text. The dotted lines indicate the size of the systematic error.

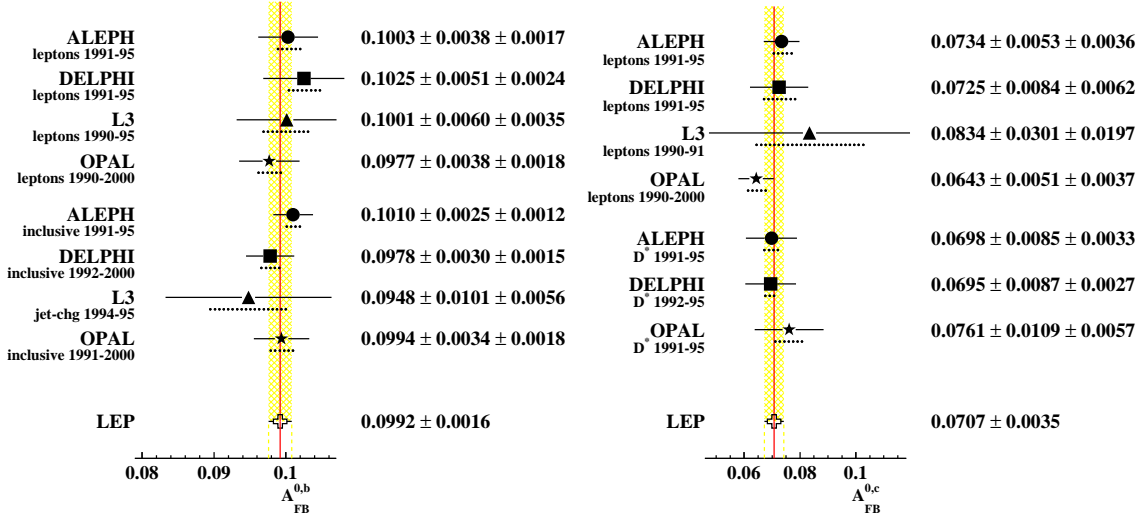


Figure 1.19: $A_{FB}^{0,b}$ and $A_{FB}^{0,c}$ measurements used in the heavy flavour combination, corrected for their dependence on parameters evaluated in the multi-parameter fit described in the text. The $A_{FB}^{0,b}$ measurements with D-mesons do not contribute significantly to the average and are not shown in the plots. The experimental results combine the different centre of mass energies. The dotted lines indicate the size of the systematic error.

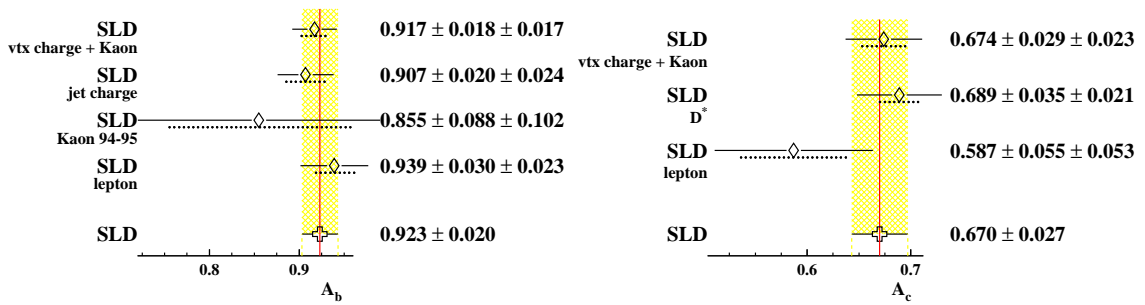


Figure 1.20: A_b and A_c measurements used in the heavy flavour combination, corrected for their dependence on parameters evaluated in the multi-parameter fit described in the text. The dotted lines indicate the size of the systematic error.

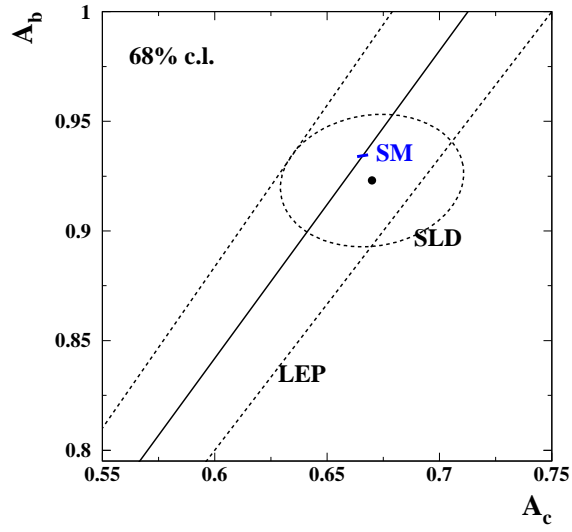


Figure 1.21: Contours in the \mathcal{A}_c - \mathcal{A}_b plane and ratios of forward-backward asymmetries from the SLD and LEP, corresponding to 68 % confidence levels assuming Gaussian systematic errors. The SM prediction is shown for the same parameters as used for Figure 1.22.

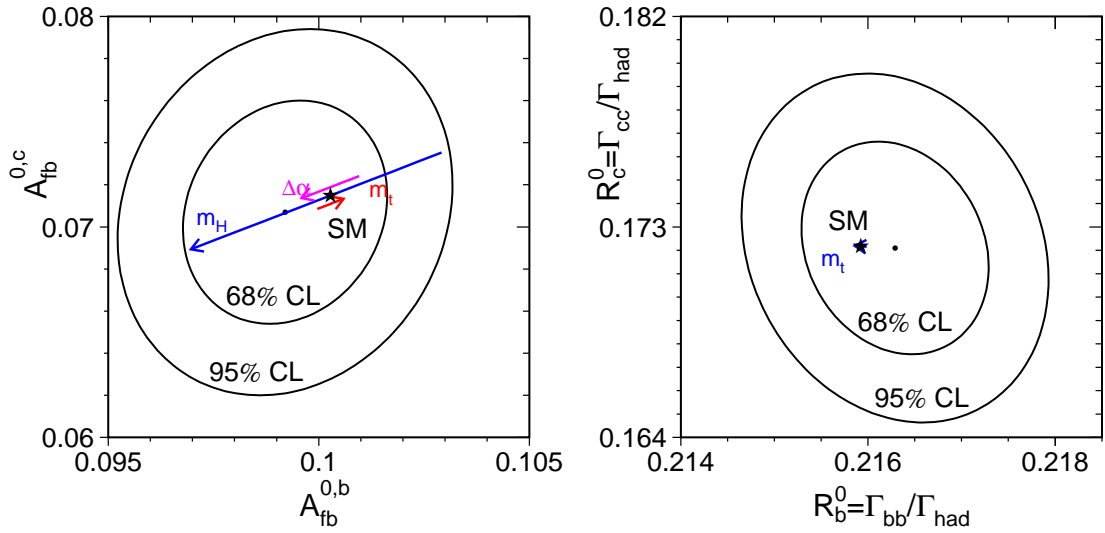


Figure 1.22: Contours in the $A_{\text{FB}}^{0,c}$ - $A_{\text{FB}}^{0,b}$ and R_c^0 - R_b^0 planes from the LEP and SLD data, corresponding to 68 % confidence levels assuming Gaussian systematic errors. The SM prediction for $m_t = 170.9 \pm 1.8$ GeV, $m_H = 300_{-186}^{+700}$ GeV and $\Delta\alpha_{\text{had}}^{(5)}(m_Z^2) = 0.02758 \pm 0.00035$ is also shown.

1.2.6 Inclusive Hadronic Charge Asymmetry

The hadronic final state occurs in Z boson production with a fraction of about 70%. The determination of the inclusive hadronic partial decay width of the Z boson described in Section 1.2.2 does not attempt to separate the quark flavours. In a similar manner, a high-statistics inclusive forward-backward charge asymmetry can be defined, avoiding heavy-quark tagging and hence based on charge flow rather than flavour flow. The inclusive hadronic forward-backward charge asymmetry, averaged over all quark flavours u, d, s, c and b, is measured through the charges of jets or hemispheres associated to the primary quark-antiquark pair:

$$\langle Q_{\text{FB}} \rangle = \sum_{q \neq t} R_q A_{\text{FB}}^{q\bar{q}} \text{sign}(Q_q), \quad (35)$$

where Q_q is the electric charge of quark flavour q . Since $A_{\text{FB}}^{q\bar{q}}$ denotes the flavour forward-backward asymmetry, up-type quarks and down-type quarks contribute with opposite sign to the forward-backward charge asymmetry. The charge separation, ie, the difference of the measured charges of the two hadronic jets, indicates how well the detector can separate charges in order to achieve a significant asymmetry measurement. As an example, the distribution of jet charges in the inclusive analysis of the L3 experiment is shown in Figure 1.23.

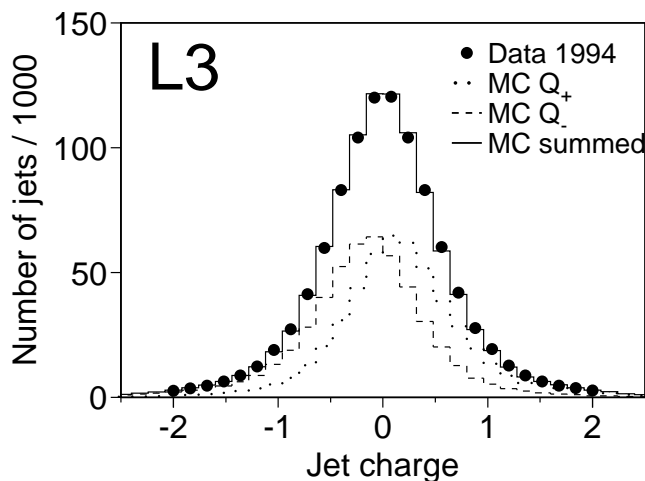


Figure 1.23: The Q_+ and Q_- distributions obtained from Monte Carlo simulation by L3. Their sum is compared to the sum of the $Q_F + Q_B \equiv Q_+ + Q_-$ distributions for 1994 data.

Using the SM dependence of R_q and $A_{\text{FB}}^{q\bar{q}}$ in terms of the effective electroweak mixing angle, the analyses [139, 140, 121, 141] of the forward-backward charge asymmetry are directly expressed in terms of $\sin^2 \theta_{\text{eff}}^{\text{lept}}$. The results listed in Table 1.11 agree very well. Taking correlated uncertainties into account, the combined result is [69]:

$$\sin^2 \theta_{\text{eff}}^{\text{lept}} = 0.2324 \pm 0.0012, \quad (36)$$

The total error is dominated by systematic effects amounting to 0.0010. The largest systematic uncertainties arise from the model input required to describe the properties of jets created in the fragmentation of light quarks and thus the description of the charge separation achievable. Note

that the correlation of this measurement with the asymmetry measurements of identified heavy-flavour samples presented in Section 1.2.5 is negligible. Since the inclusive charge separation is worse compared to that of identified $q\bar{q}$ flavours, and due to the larger model dependence, the resulting measurement of $\sin^2 \theta_{\text{eff}}^{\text{lept}}$ is of limited precision compared to the measurements with leptonic or heavy-quark final states.

Table 1.11: Determination of $\sin^2 \theta_{\text{eff}}^{\text{lept}}$ from inclusive hadronic charge asymmetries at LEP. For each experiment, the first error is statistical and the second systematic. Also listed is the correlation matrix for the total errors, summing statistical and systematic uncertainties in quadrature, used in the average of $Q_{\text{FB}}^{\text{had}}$ results.

Experiment	$\sin^2 \theta_{\text{eff}}^{\text{lept}}$	Correlations
ALEPH (1990-94)	$0.2322 \pm 0.0008 \pm 0.0011$	1.00
DELPHI (1990-91)	$0.2345 \pm 0.0030 \pm 0.0027$	0.12 1.00
L3 (1991-95)	$0.2327 \pm 0.0012 \pm 0.0013$	0.27 0.13 1.00
OPAL (1990-91)	$0.2321 \pm 0.0017 \pm 0.0029$	0.14 0.37 0.15 1.00
LEP Average	$0.2324 \pm 0.0007 \pm 0.0010$	

1.2.7 Z Boson Properties and Effective Couplings

The results presented above are derived in largely model independent analyses and are quoted in terms of experimentally motivated pseudo observables defined such that correlations between them are reduced. Other familiar pseudo observables, such as partial decay widths, effective vector and axial-vector coupling constants, or the effective electroweak mixing angle, can easily be derived through parameter transformations [69] and are presented in the following.

Z-Boson Decay Widths and Number of Neutrinos

A first example is given by the partial decay widths of the Z boson. The results, derived from the ratios of partial widths determined above, are reported in Table 1.12. The invisible decay width, i.e., the decay width for Z decays into invisible particles such as neutrinos, is included and calculated as the difference between the total decay width and the sum of all visible decay width caused by decays into hadrons and charged leptons. Assuming only SM particles, the invisible decay width constrains the number of light neutrino species to:

$$N_\nu = \frac{\Gamma_{\text{inv}}}{\Gamma_{\ell\ell}} \left(\frac{\Gamma_{\ell\ell}}{\Gamma_{\nu\bar{\nu}}} \right)_{\text{SM}} = 2.9840 \pm 0.0082, \quad (37)$$

in agreement with the three known neutrino species, excluding the existence of additional families or generations of fermions with light neutrinos. Using ratios in the above equation is advantageous because the first ratio is determined with higher precision experimentally, and in the SM calculation of the second ratio, many parametric uncertainties cancel.

Table 1.12: Partial Z decay widths, derived from the results of Tables 1.1, 1.9 and 1.10. The width denoted as $\ell^+\ell^-$ is that of a single charged massless lepton species. The width to invisible particles is calculated as the difference of total and all other partial widths.

Parameter	Average [MeV]	Correlations						
Without Lepton Universality								
		Γ_{had}	Γ_{ee}	$\Gamma_{\mu\mu}$	$\Gamma_{\tau\tau}$	$\Gamma_{b\bar{b}}$	$\Gamma_{c\bar{c}}$	Γ_{inv}
Γ_{had}	1745.8 \pm 2.7	1.00						
Γ_{ee}	83.92 \pm 0.12	-0.29	1.00					
$\Gamma_{\mu\mu}$	83.99 \pm 0.18	0.66	-0.20	1.00				
$\Gamma_{\tau\tau}$	84.08 \pm 0.22	0.54	-0.17	0.39	1.00			
$\Gamma_{b\bar{b}}$	377.6 \pm 1.3	0.45	-0.13	0.29	0.24	1.00		
$\Gamma_{c\bar{c}}$	300.5 \pm 5.3	0.09	-0.02	0.06	0.05	-0.12	1.00	
Γ_{inv}	497.4 \pm 2.5	-0.67	0.78	-0.45	-0.40	-0.30	-0.06	1.00
With Lepton Universality								
		Γ_{had}	$\Gamma_{\ell\ell}$	$\Gamma_{b\bar{b}}$	$\Gamma_{c\bar{c}}$	Γ_{inv}		
Γ_{had}	1744.4 \pm 2.0	1.00						
$\Gamma_{\ell\ell}$	83.985 \pm 0.086	0.39	1.00					
$\Gamma_{b\bar{b}}$	377.3 \pm 1.2	0.35	0.13	1.00				
$\Gamma_{c\bar{c}}$	300.2 \pm 5.2	0.06	0.03	-0.15	1.00			
Γ_{inv}	499.0 \pm 1.5	-0.29	0.49	-0.10	-0.02	1.00		

The Asymmetry Parameters

The forward-backward asymmetries determine products of the asymmetry parameters, $A_{\text{FB}}^{0,f} = (3/4)\mathcal{A}_e\mathcal{A}_f$, while the polarised asymmetries measure \mathcal{A}_f directly. Using all measurements determining any (combination of) leptonic asymmetry parameters, combined values are calculated and reported in Table 1.13. The results for the different charged lepton species agree well as expected from lepton universality. With this assumption, a combined value of

$$\mathcal{A}_\ell = 0.1501 \pm 0.0016 \quad (38)$$

is obtained, where this average has a χ^2/dof of 7.8/9, corresponding to a probability of 56%.

Table 1.13: Results on the leptonic asymmetry parameters \mathcal{A}_ℓ using the 14 electroweak measurements of Tables 1.1 and 1.2, and Equations 20 and 21. The combination has a χ^2/dof of 3.6/5, corresponding to a probability of 61%.

Parameter	Average	Correlations		
		\mathcal{A}_e	\mathcal{A}_μ	\mathcal{A}_τ
\mathcal{A}_e	0.1514 ± 0.0019	1.00		
\mathcal{A}_μ	0.1456 ± 0.0091	-0.10	1.00	
\mathcal{A}_τ	0.1449 ± 0.0040	-0.02	0.01	1.00

Using this combined value of the leptonic asymmetry parameter \mathcal{A}_ℓ , the mutual consistency of the heavy-flavour measurements $A_{\text{FB}}^{0,q} = (3/4)\mathcal{A}_\ell\mathcal{A}_q$ and \mathcal{A}_q is shown in Figure 1.24. While the bands show good overlap for c quarks, the b-quark case exhibits some tension between the measurements. This is made strikingly obvious by extracting the asymmetry parameter \mathcal{A}_b from the forward-backward asymmetry measurement using the above value of \mathcal{A}_ℓ : $\mathcal{A}_b = (4/3)A_{\text{FB}}^{0,b}/\mathcal{A}_\ell$. All \mathcal{A}_q determinations are compared in Table 1.14, together with the SM expectation. While there is good agreement for c quarks, the ratio $\mathcal{A}_b = (4/3)A_{\text{FB}}^{0,b}/\mathcal{A}_\ell$ shows a 3.2 standard deviation discrepancy from the SM expectation; a consequence of the same effect as discussed towards the end of Section 1.2.5. The numerical results of the joint analysis in terms of asymmetry parameters are in reported in Table 1.15.

Table 1.14: Determination of the quark asymmetry parameters \mathcal{A}_q , based on the ratio $A_{\text{FB}}^{0,q}/\mathcal{A}_\ell$ and the direct measurement A_{LRFB}^q . Lepton universality for \mathcal{A}_ℓ is assumed. The correlation between $4A_{\text{FB}}^{0,b}/3\mathcal{A}_\ell$ and $4A_{\text{FB}}^{0,c}/3\mathcal{A}_\ell$ is +0.24, while it is +0.11 between the direct measurements \mathcal{A}_b and \mathcal{A}_c . The expectation of \mathcal{A}_q in the SM is listed in the last column.

Flavour q	$\mathcal{A}_q = \frac{4}{3} \frac{A_{\text{FB}}^{0,q}}{\mathcal{A}_\ell}$	Direct \mathcal{A}_q	SM
b	0.881 ± 0.017	0.923 ± 0.020	0.935 ± 0.001
c	0.628 ± 0.032	0.670 ± 0.027	0.668 ± 0.002

Effective Couplings of the Neutral Weak Current

The electroweak measurements presented above determine asymmetry parameters \mathcal{A}_f , their products such as $A_{\text{FB}}^{0,f} = (3/4)\mathcal{A}_e\mathcal{A}_f$, as well as ratios of partial decay widths. In terms of effective

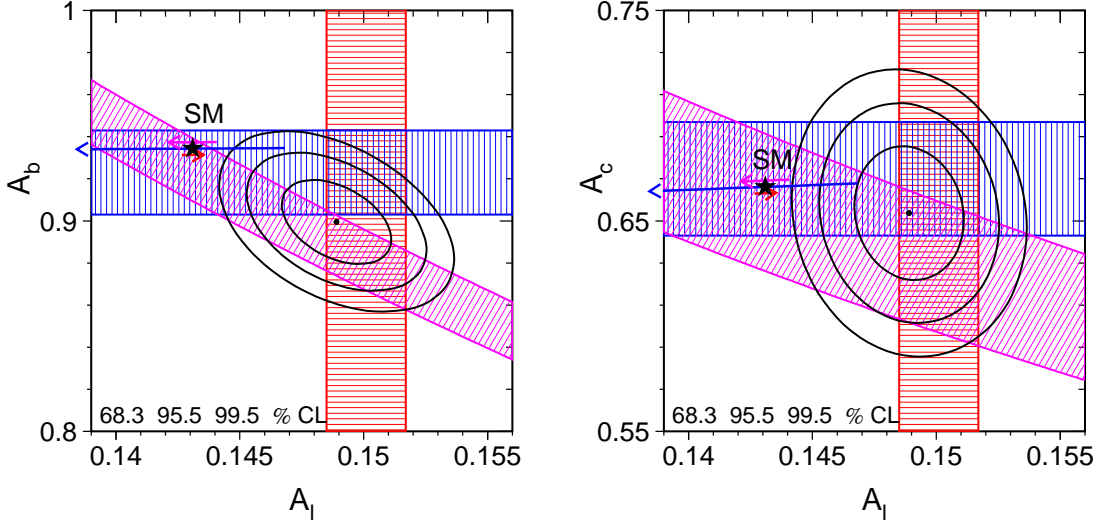


Figure 1.24: Comparison of the measurements of \mathcal{A}_ℓ , \mathcal{A}_q and $A_{\text{FB}}^{0,q}$ for (top) b-quarks, and (bottom) c-quarks, assuming lepton universality. Bands of ± 1 standard deviation width in the $(\mathcal{A}_\ell, \mathcal{A}_q)$ plane are shown for the measurements of \mathcal{A}_ℓ (vertical band), \mathcal{A}_q (horizontal band), and $A_{\text{FB}}^{0,q} = (3/4)\mathcal{A}_e\mathcal{A}_q$ (diagonal band). Also shown are the 68%, 95% and 99.5% confidence level contours for the two asymmetry parameters resulting from the joint analysis (Table 1.15). The arrows pointing to the right and to the left show the variation in the SM prediction for varying $\Delta\alpha_{\text{had}}^{(5)}(m_Z^2)$ in the range 0.02758 ± 0.00035 (arrow displaced vertically upwards), m_H in the range of 300_{-186}^{+700} GeV, and m_t in the range 170.9 ± 1.8 GeV (arrow displaced vertically downwards). All arrows point in the direction of increasing values of these parameters.

Table 1.15: Results on the quark asymmetry parameters \mathcal{A}_q and the leptonic asymmetry parameter \mathcal{A}_ℓ assuming neutral-current lepton universality using the 13 electroweak measurements of Tables 1.1, 1.9 and 1.10, and Equations 13 and 22. The combination has a χ^2/dof of 4.5/4, corresponding to a probability of 34%.

Parameter	Average	Correlations		
		\mathcal{A}_ℓ	\mathcal{A}_b	\mathcal{A}_c
\mathcal{A}_ℓ	0.1489 ± 0.0015	1.00		
\mathcal{A}_b	0.899 ± 0.013	-0.42	1.00	
\mathcal{A}_c	0.654 ± 0.021	-0.10	0.15	1.00

vector and axial-vector coupling constants of the neutral weak current, g_{Vf} and g_{Af} , the asymmetry parameters \mathcal{A}_f depend only on the ratio g_{Vf}/g_{Af} , while partial widths are proportional to $g_{Vf}^2 + g_{Af}^2$. Hence, the combined set of measurements allows to disentangle the effective coupling constants g_{Vf} and g_{Af} .

Results for the leptonic couplings are reported in Tables 1.16. The values for the three charged leptons agree well as expected from neutral-current lepton universality. This is also shown in Figure 1.25. Imposing lepton universality results with increased precision are obtained and reported

in Table 1.17. Including also the results on heavy quarks, the results are listed in Table 1.18. The value of the leptonic axial coupling $g_{A\ell}$ is different from the corresponding Born-level value of $T_3^\ell = -1/2$ by 4.8 standard deviations, indicating the presence of non-QED electroweak radiative corrections. The contour curves corresponding to the quark couplings are presented in Figure 1.26. The difference between b-quark couplings and the SM expectation is caused by the b-quark asymmetry parameter extracted from the forward-backward asymmetry as discussed above.

Table 1.16: Results on the effective coupling constants for leptons, using the 14 electroweak measurements of Tables 1.1 and 1.2, and Equations 20 and 21. The combination has a χ^2/dof of 3.6/5, corresponding to a probability of 61%.

Parameter	Average	Correlations						
		$g_{A\nu}$	g_{Ae}	$g_{A\mu}$	$g_{A\tau}$	g_{Ve}	$g_{V\mu}$	$g_{V\tau}$
$g_{A\nu} \equiv g_{V\nu}$	$+0.5003 \pm 0.0012$	1.00						
g_{Ae}	-0.50111 ± 0.00035	-0.75	1.00					
$g_{A\mu}$	-0.50120 ± 0.00054	0.39	-0.13	1.00				
$g_{A\tau}$	-0.50204 ± 0.00064	0.37	-0.12	0.35	1.00			
g_{Ve}	-0.03816 ± 0.00047	-0.10	0.01	-0.01	-0.03	1.00		
$g_{V\mu}$	-0.0367 ± 0.0023	0.02	0.00	-0.30	0.01	-0.10	1.00	
$g_{V\tau}$	-0.0366 ± 0.0010	0.02	-0.01	0.01	-0.07	-0.02	0.01	1.00

Table 1.17: Results on the effective coupling constants for leptons, using the 14 electroweak measurements of Tables 1.1 and 1.2, and Equations 20 and 21. Lepton universality is imposed. The combination has a χ^2/dof of 7.8/9, corresponding to a probability of 56%.

Parameter	Average	Correlations		
		g_ν	$g_{A\ell}$	$g_{V\ell}$
$g_{A\nu} \equiv g_{V\nu}$	$+0.50076 \pm 0.00076$	1.00		
$g_{A\ell}$	-0.50123 ± 0.00026	-0.48	1.00	
$g_{V\ell}$	-0.03783 ± 0.00041	-0.03	-0.06	1.00

The Effective Electroweak Mixing Angle

The effective electroweak mixing angle is in one to one correspondence with the ratio g_{Vf}/g_{Af} and thus the asymmetry parameters \mathcal{A}_f . Owing to the values of weak isospin and electric charge, the leptonic asymmetry parameter \mathcal{A}_ℓ shows the largest sensitivity to the mixing angle, and is thus determined with highest precision even in case of heavy-quark forward-backward asymmetry measurements.

The comparison of all $\sin^2 \theta_{\text{eff}}^{\text{lept}}$ values derived from asymmetry measurements is shown in Figure 1.27. The average of these six $\sin^2 \theta_{\text{eff}}^{\text{lept}}$ determinations is:

$$\sin^2 \theta_{\text{eff}}^{\text{lept}} = 0.23153 \pm 0.00016, \quad (39)$$

where the average has a χ^2/dof of 11.8/5, corresponding to a probability of only 3.7%. This large χ^2/dof value is caused by the two most precise determinations of $\sin^2 \theta_{\text{eff}}^{\text{lept}}$, the measurements

Table 1.18: Results on the effective coupling constants for leptons and quarks assuming neutral-current lepton universality, using the 13 electroweak measurements of Tables 1.1, 1.9 and 1.10, and Equations 13 and 22. The combination has a χ^2/dof of 4.5/4, corresponding to a probability of 34%.

Parameter	Average	Correlations							
		$g_{A\nu}$	$g_{A\ell}$	g_{Ab}	g_{Ac}	$g_{V\ell}$	g_{Vb}	g_{Vc}	
$g_{A\nu} \equiv g_{V\nu}$	$+0.50075 \pm 0.00077$	1.00							
$g_{A\ell}$	-0.50125 ± 0.00026	-0.49	1.00						
g_{Ab}	-0.5144 ± 0.0051	0.01	-0.02	1.00					
g_{Ac}	$+0.5034 \pm 0.0053$	-0.02	-0.02	0.00	1.00				
$g_{V\ell}$	-0.03753 ± 0.00037	-0.04	-0.04	0.41	-0.05	1.00			
g_{Vb}	-0.3220 ± 0.0077	0.01	0.05	-0.97	0.04	-0.42	1.00		
g_{Vc}	$+0.1873 \pm 0.0070$	-0.01	-0.02	0.15	-0.35	0.10	-0.17	1.00	

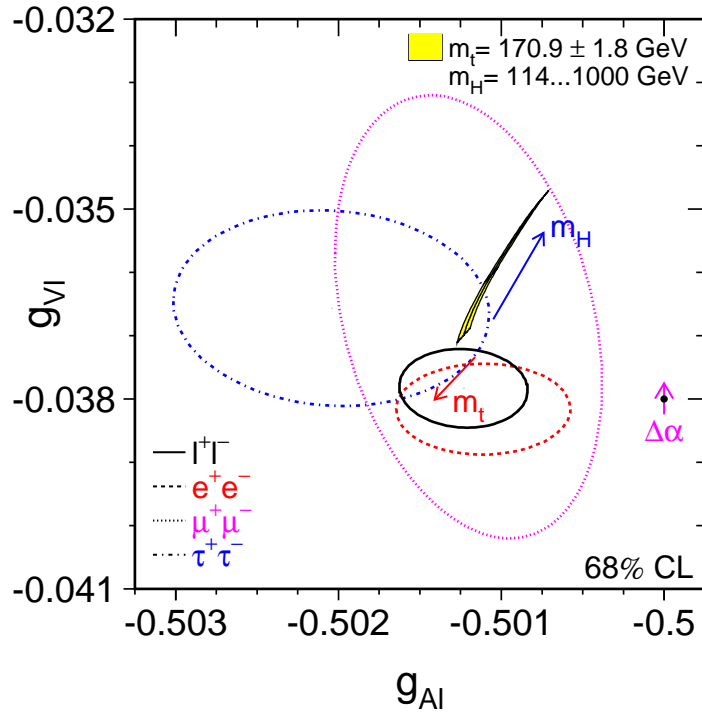


Figure 1.25: Comparison of the effective vector and axial-vector coupling constants for leptons (Tables 1.16 and 1.17). The shaded region in the lepton plot shows the predictions within the SM for $m_t = 170.9 \pm 1.8$ GeV and $m_H = 300_{-186}^{+700}$ GeV; varying the hadronic vacuum polarisation by $\Delta\alpha_{\text{had}}^{(5)}(m_Z^2) = 0.02758 \pm 0.00035$ yields an additional uncertainty on the SM prediction shown by the arrow labeled $\Delta\alpha$.

of \mathcal{A}_ℓ by SLD, dominated by the A_{LR}^0 result, and of $A_{FB}^{0,b}$ at LEP. These two measurements fall on opposite sides of the average and differ by 3.2 standard deviations. This is a consequence of

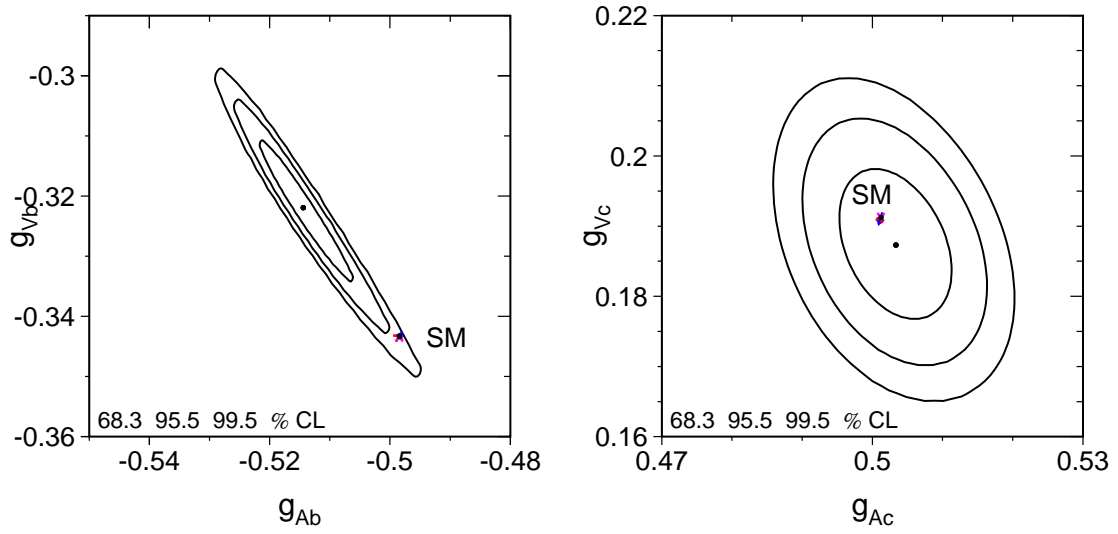


Figure 1.26: Comparison of the effective vector and axial-vector coupling constants for heavy quarks, using results on leptons and assuming lepton universality (Table 1.18). Top: b quarks; bottom: c quarks. Compared to the experimental uncertainties, the SM predictions for the heavy quarks b and c have negligible dependence on the SM input parameters.

the same effect as discussed above: the deviation in b-quark couplings is reflected in the value of $\sin^2 \theta_{\text{eff}}^{\text{lept}}$ extracted from $A_{\text{FB}}^{0,b}$.

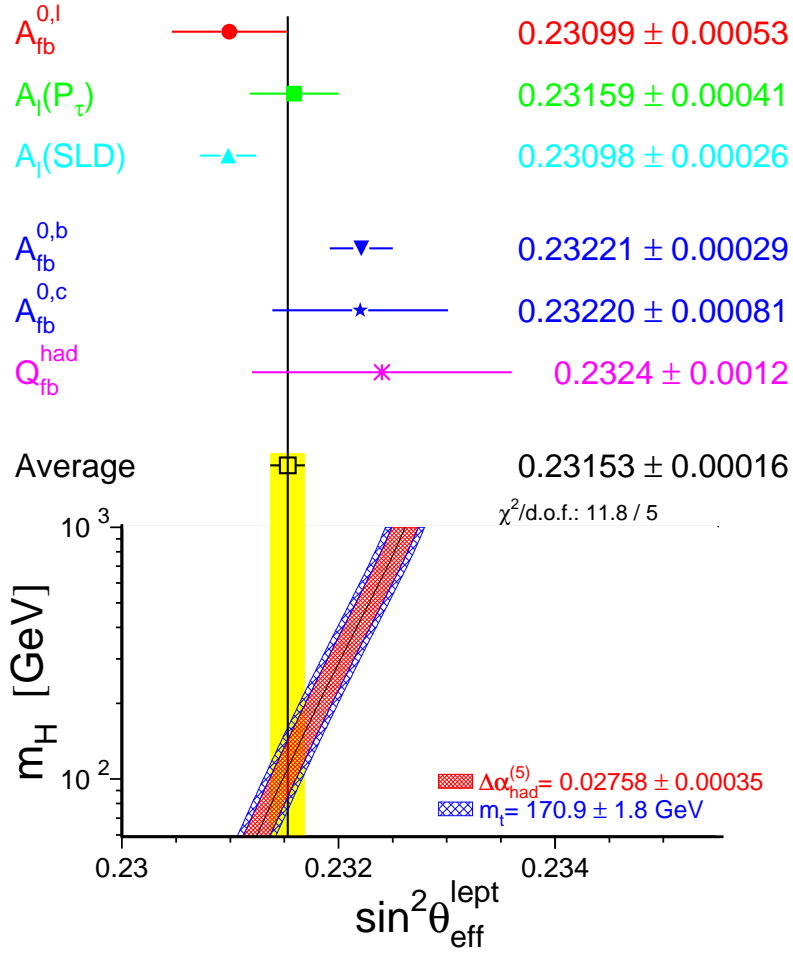


Figure 1.27: Comparison of the effective electroweak mixing angle $\sin^2 \theta_{\text{eff}}^{\text{lept}}$ derived from measurements depending on lepton couplings only (top) and also quark couplings (bottom). Also shown is the SM prediction for $\sin^2 \theta_{\text{eff}}^{\text{lept}}$ as a function of m_H . The additional uncertainty of the SM prediction is parametric and dominated by the uncertainties in $\Delta\alpha_{\text{had}}^{(5)}(m_Z^2)$ and m_t , shown as the bands. The total width of the band is the linear sum of these effects.

1.3 The W Boson

1.3.1 W Bosons at Hadron Colliders

Production of W Bosons

At hadron colliders, W and Z bosons are produced by quark-antiquark fusion, $p\bar{p} \rightarrow W + X_W$ and $p\bar{p} \rightarrow Z + X_Z$, where X_V , $V = W, Z$, denotes the $p\bar{p}$ remnant recoiling against the heavy intermediate vector boson V. Owing to the hadronic event environment and overwhelming background of QCD multi-jet production, only events where the Z or W decay into leptons can be selected: $W \rightarrow \ell\nu_\ell$ and $Z \rightarrow \ell^+\ell^-$. The lowest-order Feynman diagrams on parton level for W and Z production with subsequent leptonic decay are shown in Figure 1.28.

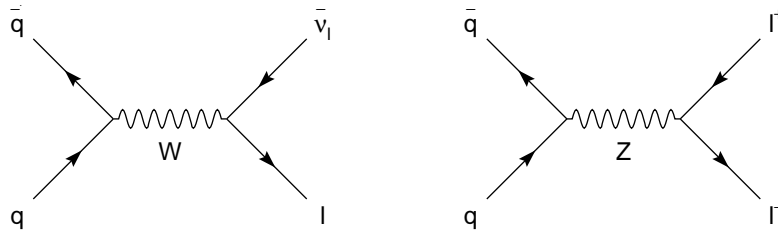


Figure 1.28: Feynman diagrams of W and Z production and decay in $p\bar{p}$ collisions on parton level.

In 1983, the W and Z bosons were discovered [142, 144] in $p\bar{p}$ collisions by the experiments UA1 and UA2 taking data at CERN's SPS collider at a centre-of-mass energy between 0.5 TeV and 0.6 TeV. In total, a few hundred events were eventually observed. The experiments CDF and DØ, taking data at the Tevatron accelerator providing $p\bar{p}$ collisions with a centre-of-mass energy of 1.8 TeV in Run-I, have observed several 10,000 leptonic W and Z decays using the complete Run-I data of about 100pb^{-1} for each experiment.

Determination of W-Boson Mass and Width

Owing to the neutrino in W decays, and loss of remnant particles along the beam axis, the kinematics of the W boson can not be fully reconstructed. However, the kinematics is closed when observed in the plane transverse to the beam axis and in case the transverse part of the hadronic recoil X is measured. For this reason, the W-boson mass and width analyses exploit kinematic variables measured in the transverse plane only: (i) E_T^ℓ , the transverse energy of the charged lepton, (ii) E_T^ν , the missing transverse energy - solely given by the transverse energy of the neutrino in the ideal case, and (iii) m_T^2 , the transverse mass of the reconstructed W boson calculated as:

$$m_T^2(\ell, \nu) = 2E_T^\ell E_T^\nu (1 - \cos \phi_{\ell\nu}) \leq m_{\text{inv}}^2(\ell, \nu) = m_W^2, \quad (40)$$

where the angle $\phi_{\ell\nu}$ denotes the azimuthal opening angle between the direction of the lepton momentum and the missing-energy vector (neutrino) in the transverse plane. The distributions of all three quantities are affected by the mass and total decay width of the W boson, allowing to measure these quantities.

The transverse mass is always smaller than the invariant mass of the decaying W boson. It approaches the invariant mass when the W boson decay products lie in the transverse plane. This cutoff or Jacobian peak allows the W mass to be extracted from the position of the upper edge

of the transverse mass distribution. The result is more precise than that derived from the other distributions. The transverse mass distribution also facilitates the measurement of the total width of the W boson. A non-zero total decay width effectively leads to a smearing, since the decaying W bosons have an invariant mass distributed according to a Breit-Wigner functional form. Since a Breit-Wigner falls off more slowly than Gaussian resolution effects, the number of W events with measured transverse mass above the nominal cut-off of m_W depends strongly on the total width of the W boson.

The distributions of the reconstructed transverse mass for $W \rightarrow e\nu_e$ events from DØ [146, 147] and $W \rightarrow \mu\nu$ events from CDF [148] are shown in Figure 1.29. DØ selects electrons in a range of pseudo rapidity $|\eta| \leq 2.5$, while CDF selects electrons and muons up to $|\eta| \leq 1$. The region in transverse mass analysed for m_W is extended around the Jacobian peak to include normalisation information. The results on m_W obtained by CDF and DØ based on all Run-I data are in good agreement: $m_W = 80.433 \pm 0.079$ GeV [148] and $m_W = 80.483 \pm 0.084$ GeV [146, 147], respectively. The contributions to the total uncertainty of each measurement are reported in Table 1.19. The dominant systematic error arises from the calibration of the lepton energy scale. Since this calibration is derived from data analysing $\pi^0 \rightarrow \gamma\gamma$ and $J/\Psi/\Upsilon/Z \rightarrow \ell^+\ell^-$ decays, it will decrease along with the statistical error of the measurements with the increased data samples collected in Run-II, as shown by the very recent CDF result obtained from 200/pb of Run-II data: $m_W = 80.413 \pm 0.048$ [149].

The principle of the width measurement is shown in Figure 1.30. The integral of the high-end tail in the transverse mass distribution depends on Γ_W . The width results from Run-I data are $\Gamma_W = 2.05 \pm 0.13$ GeV (CDF [150, 151]) and $\Gamma_W = 2.231^{+0.175}_{-0.170}$ GeV (DØ [152]). The preliminary analysis from the DØ collaboration based on Run-II data and shown in Figure 1.30 yields $\Gamma_W = 2.011 \pm 0.142$ GeV [153]. The contributions of systematic uncertainties to the total uncertainty of each measurement are listed in Table 1.20.

The combination [154, 155] of the mass and width results from Run-I and Run-II yields the values:

$$m_W = 80.429 \pm 0.039 \text{ GeV} \tag{41}$$

$$\Gamma_W = 2.078 \pm 0.087 \text{ GeV} . \tag{42}$$

Both results are dominated by statistics, and many systematic uncertainties, for example energy calibration effects, will also decrease with increased luminosity collected in Run-II.

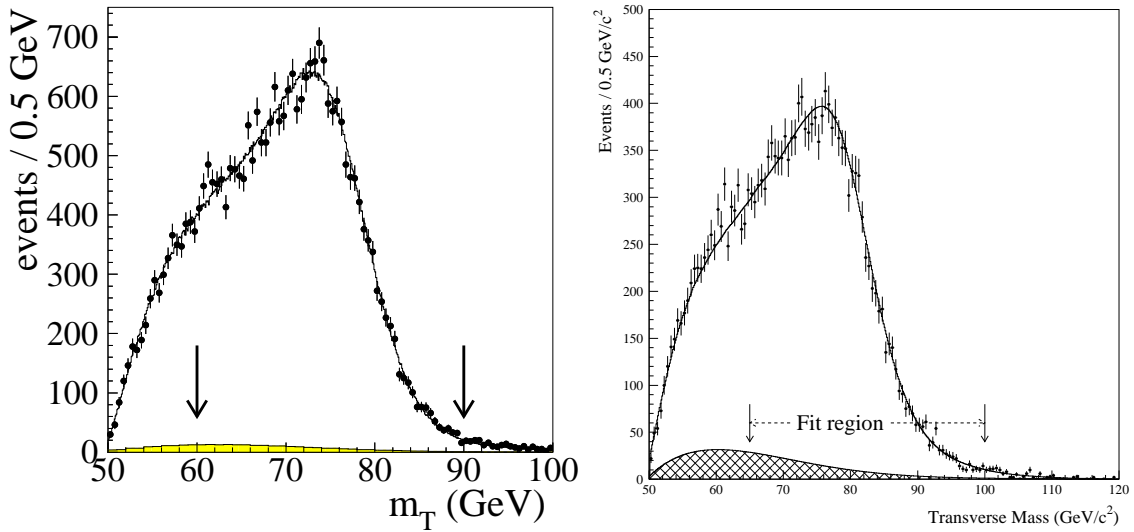


Figure 1.29: Distributions of the reconstructed transverse mass from events collected in Run-I. Left: $W \rightarrow e\nu_e$ events from $D\bar{0}$; right: $W \rightarrow \mu\nu$ events from CDF. The solid line shows the fit result including background. The arrows indicate the fit region. The shaded part denotes the background.

Table 1.19: Systematic uncertainties in the measurements of the mass of the W boson by the Tevatron experiments CDF and $D\bar{0}$ in Run-I. All numbers are in MeV. The first group denotes uncorrelated uncertainties, the second group denotes uncertainties correlated between measurements.

Source	$D\bar{0}$ e	CDF e	CDF μ
W statistics	60	65	100
Lepton energy scale	56	75	85
Lepton energy resolution	19	25	20
W transverse momentum	15	15	20
Recoil model	35	37	35
Selection	12	–	18
Background	9	5	25
PDF and parton luminosity	$7\oplus 4$	15	
Radiative corrections	12	11	
Γ_W	10	10	

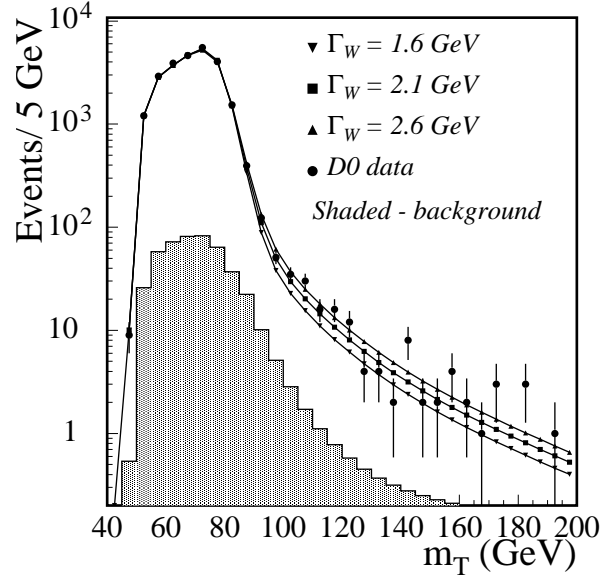


Figure 1.30: Distribution of the reconstructed transverse mass in $W \rightarrow e\nu_e$ events collected by DØ in Run-II, showing predicted curves for various values of Γ_W . The shaded part denotes the background.

Table 1.20: Summary of the five measurements of Γ_W performed by CDF and DØ. All numbers are in MeV. For the systematic uncertainties, the first group denotes uncorrelated uncertainties and the second group denotes uncertainties correlated between measurements.

	Run-I			Run-II	
	CDF		DØ	DØ	
	e (Ia)	e (Ib)	μ	e	
Result	2110	2175	1780	2231	2011
Stat.	280	125	195	142	93
E-scale	42	20	15	42	23
Non-lin	-	60	5	-	-
Recoil	103	60	90	59	80
$p_T(W)$	127	55	70	12	29
BG	17	30	50	42	3
DM, ℓ -ID	-	30	40	10	16
Resol.	13	10	20	27	51
PDF	15	15	15	39	27
QED RC	28	10	10	10	3
m_W	10	10	10	15	15
Syst.	173	114	135	99	108
Total	329	169	237	173	142

1.3.2 W Bosons at LEP-II

Production of W Bosons

The dominant production mode for W bosons in the LEP-II centre of mass energy range of 130 GeV to 209 GeV is W-pair production, $e^+e^- \rightarrow W^+W^-$. The phase space for the production of on-shell W-boson pairs opens up at the kinematic threshold of $\sqrt{s} = 2m_W$. The lowest-order Feynman diagrams contributing to this process are shown in Figure 1.31. Besides the t -channel neutrino exchange diagram, two other interesting diagrams contribute, namely the s -channel diagrams involving the triple-gauge-boson vertex between the neutral and charged gauge bosons of the electroweak interaction. The W boson decays via the charged weak current into a fermion-antifermion pair, 3 leptonic modes ($e\nu_e, \mu\nu, \tau\nu$) and 6 hadronic modes ($q\bar{q}'$ except top), so that W-pair production leads to four-fermion final states.

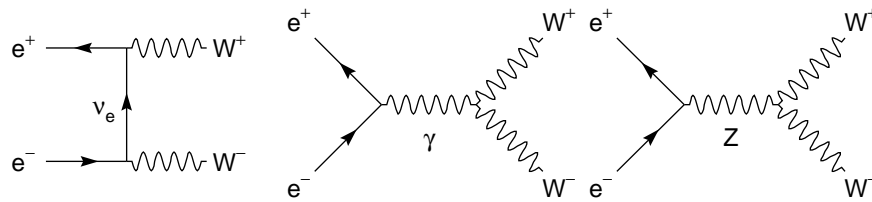


Figure 1.31: Feynman diagrams of W-pair production in e^+e^- collisions. The contribution of Higgs boson exchange diagrams is negligible.

Pair production of W bosons at LEP-II exhibits a clean signature in the detectors since the events contain only the decay products of the two W bosons. Typical events of each type are shown in Figures 1.32 to 1.35. The LEP experiments analyse all possible decay modes and event signatures. Hadronic events, $W^+W^- \rightarrow q\bar{q}q\bar{q}$ are selected with typical efficiencies of 85% and purities of 80%. Events must contain at least four well separated jets and no large missing energy. The dominant background arises from QCD multi-jet production. Leptonic events, $W^+W^- \rightarrow \ell\nu_\ell\ell\nu_\ell$ are selected by requiring two acoplanar charged leptons, which rejects the main background arising from dilepton production, $e^+e^- \rightarrow \ell^+\ell^-$. Efficiencies ranging from 30% to 70% and purities ranging from 75% to 90% are achieved, where the lower values are obtained if both leptons are τ leptons and the higher values if both leptons are electrons or muons. Semi-leptonic events, $W^+W^- \rightarrow q\bar{q}\ell\nu_\ell$, are tagged by the presence of a high-energy charged lepton. In addition, events must contain two hadronic jets and missing energy due to the neutrino. The main background arises through inclusive lepton production in $q\bar{q}$ events, where the missing energy is given by initial-state radiative photons lost in the beam pipe. Semi-leptonic events are selected with an efficiency between 30% and 90% and a purity between 70% and 95%, where the lower values are obtained for $q\bar{q}\tau\nu$ events and the higher values for $q\bar{q}e\nu_e$ and $q\bar{q}\mu\nu$ events.

The measurement of production cross sections for each final state allows the simultaneous determination of the total W-pair production cross section and the branching fractions of W decay. The total W-pair cross section measured as a function of the centre-of-mass energy, \sqrt{s} , is shown in Figure 1.36, having combined the results of the four LEP experiments at each \sqrt{s} point [156]. Especially at higher energies, the influence of the s -channel Feynman diagrams is clearly visible, establishing qualitatively as well as quantitatively the γWW and ZWW triple-gauge-boson couplings of the electroweak interaction. Combining all energy points, the ratio of measurement to theory is determined to be 0.995 ± 0.009 , a successful precision test of the theory [156].

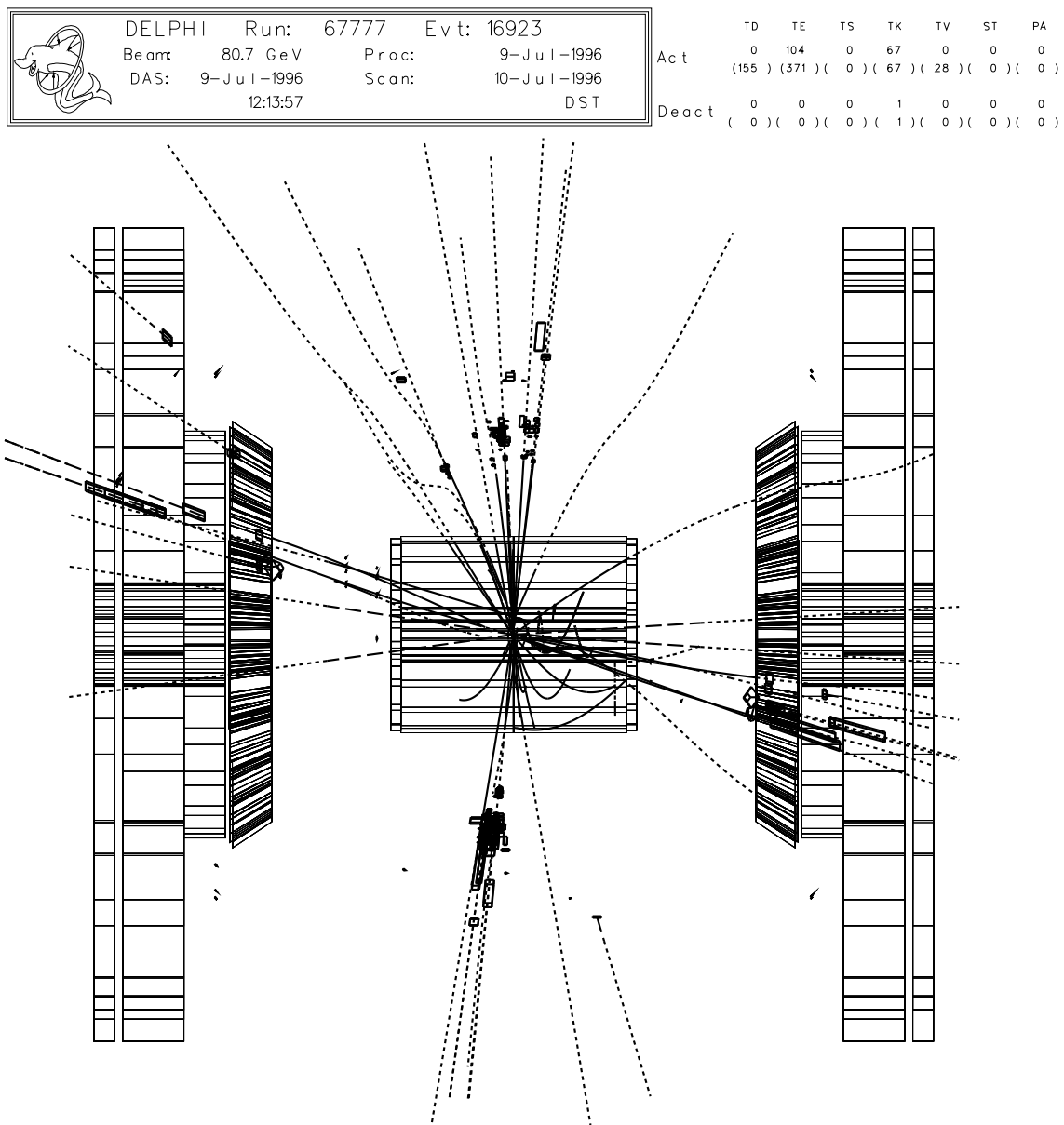


Figure 1.32: $W^+W^- \rightarrow q\bar{q}q\bar{q}$ event observed in the DELPHI detector, showing four well separated jets.

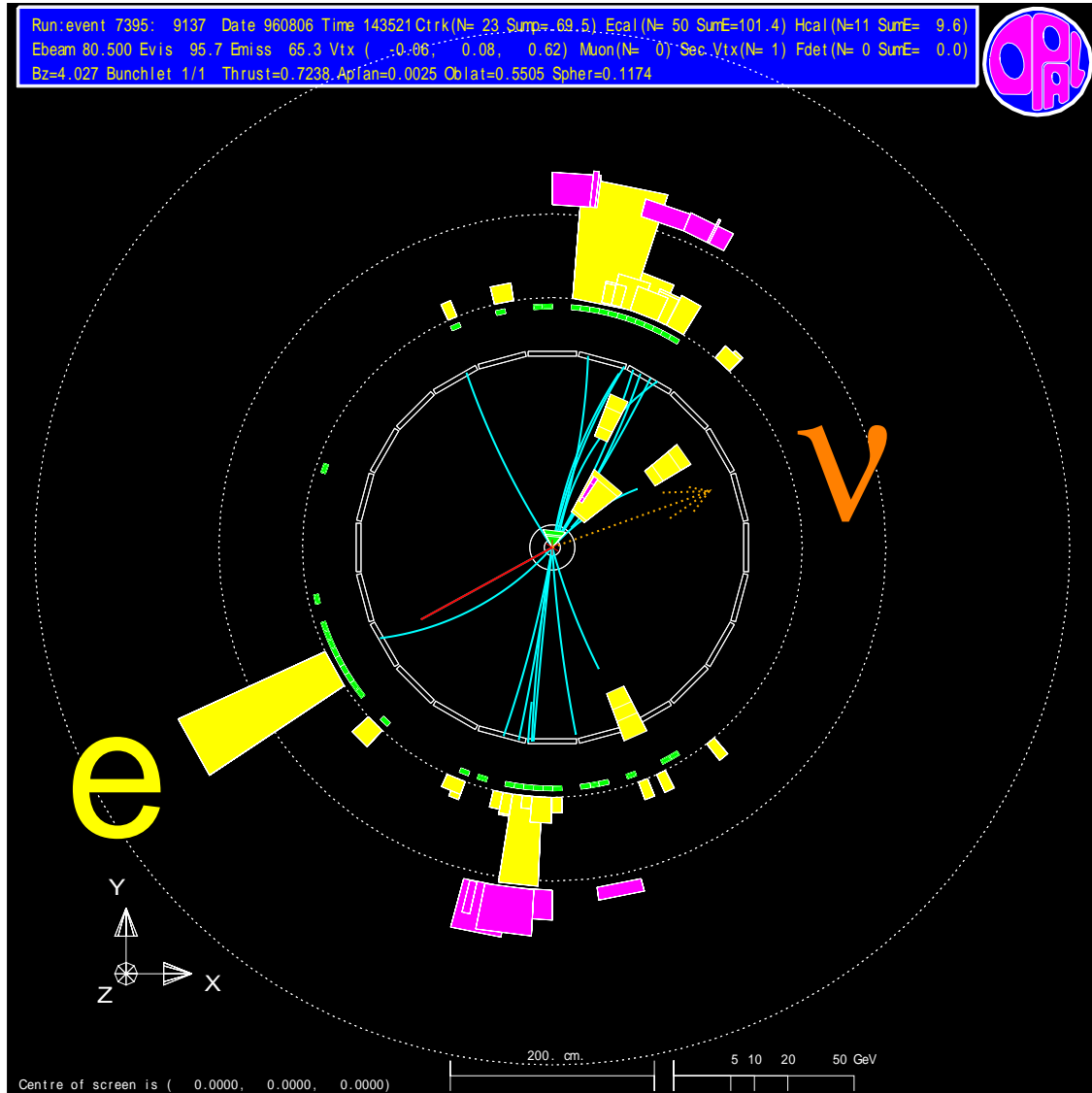


Figure 1.33: W-pair events selected at LEP-II: $W^+W^- \rightarrow q\bar{q}e\nu_e$ event observed in the OPAL detector, showing two hadronic jets and an electron.

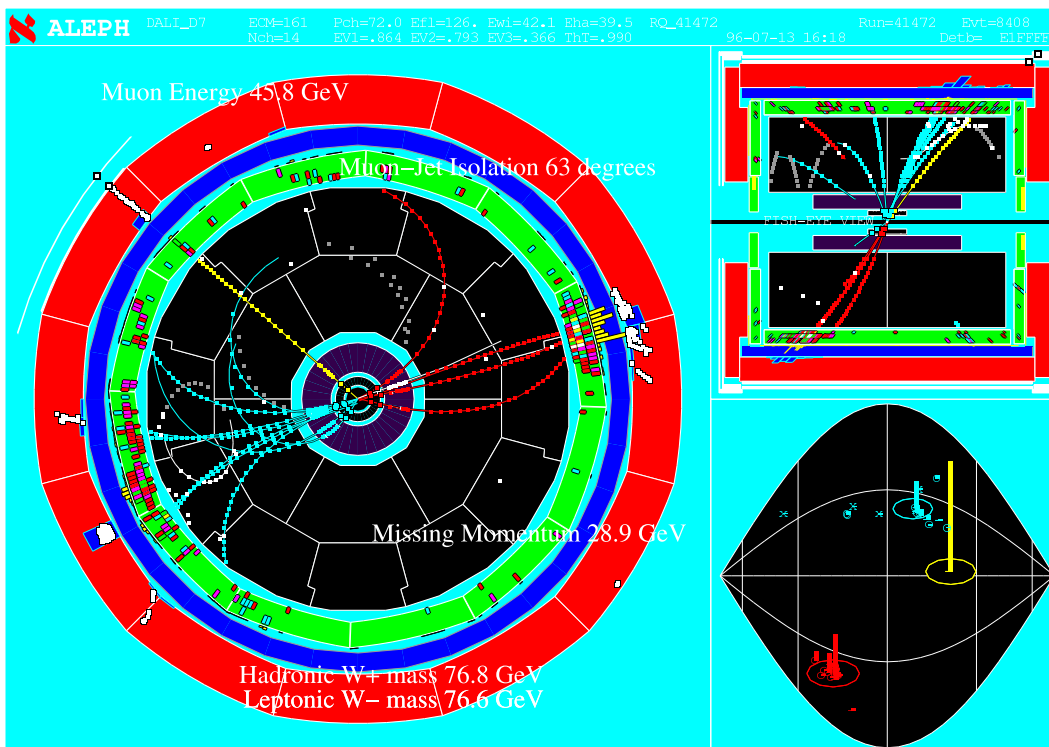


Figure 1.34: W -pair events selected at LEP-II: $W^+W^- \rightarrow q\bar{q}\mu\nu$ event observed in the ALEPH detector.

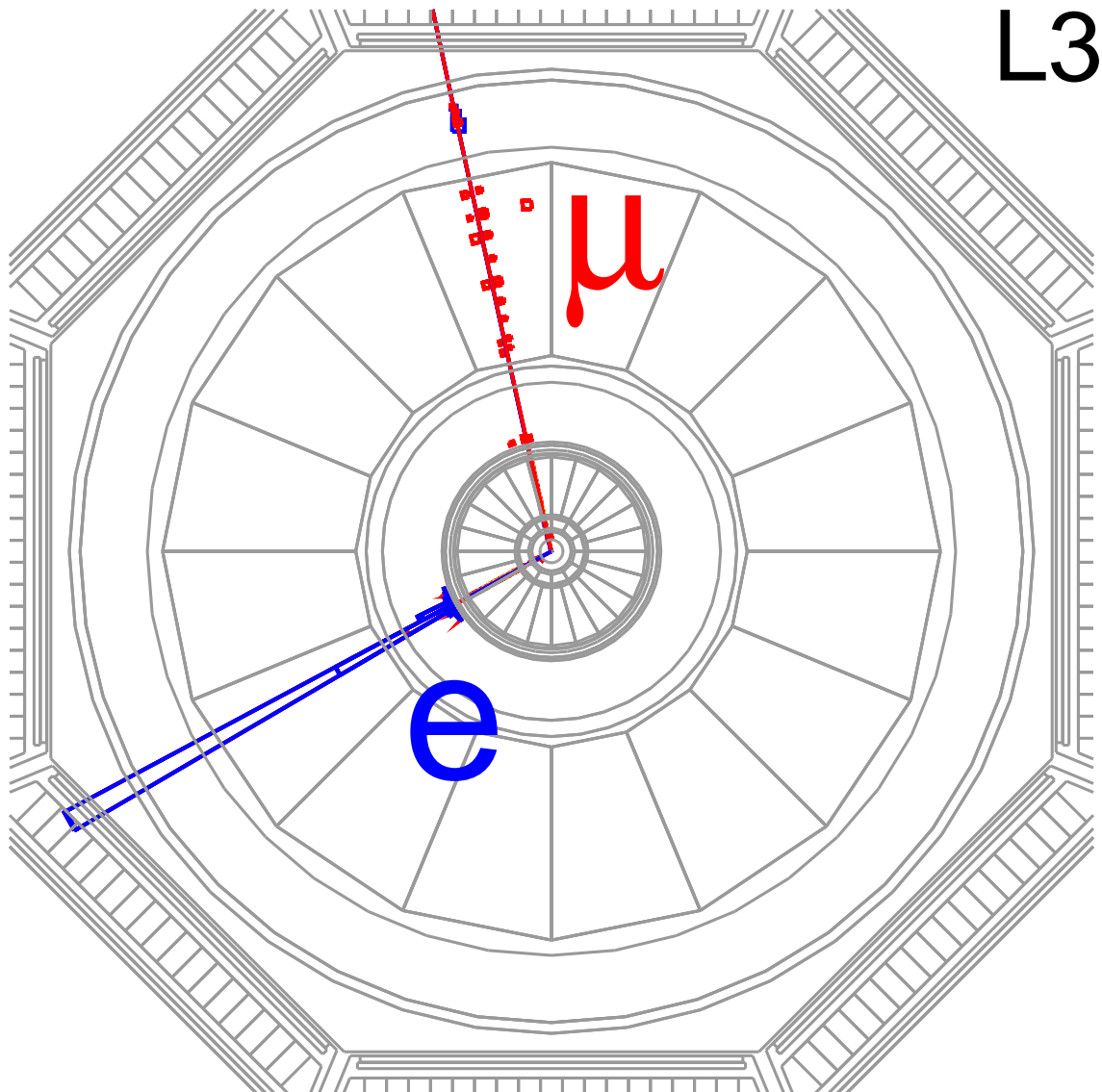


Figure 1.35: W-pair events selected at LEP-II: $W^+W^- \rightarrow e\nu_e\mu\nu$ event observed in the L3 detector.

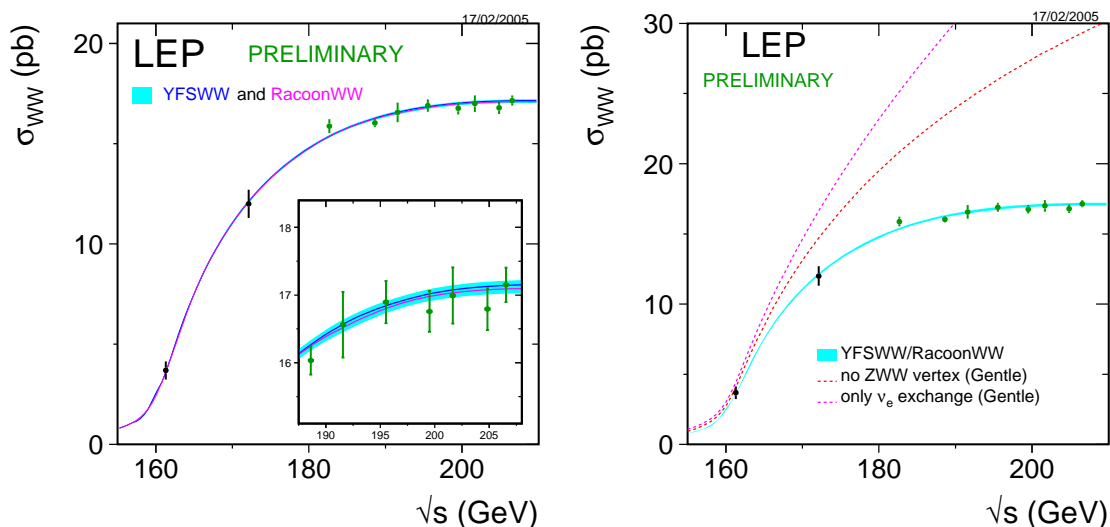


Figure 1.36: Combined W -pair cross sections, shown as dots with error bars, as measured by the four LEP experiments as a function of the centre-of-mass energy, \sqrt{s} . The results are preliminary. Left: Measured cross sections compared to the SM calculation. The theoretical uncertainty is shown as the width of the curve. Right: Cross section expected for theories without the γWW and ZWW gauge vertices. The measurements clearly require the presence of these vertices with their expected properties.

The comparison of the branching fractions of W decay, determined for the three leptonic modes and the inclusive hadronic mode, is shown in Figure 1.37. In general, good agreement is observed between the results of the four experiments. The combined results [156] agree well with the SM expectation except in the case of $W \rightarrow \tau\nu$ decays, where all experiments measured a branching fraction higher than expected. The combination under assumption of lepton universality also agrees with the expectation, because the electron and muon decay modes are measured to be slightly smaller than expected. Comparing the tau decay mode to the average of the electron and muon mode results, which maximises the significance of the effect a posteriori, results in the two values being different at the level of 2.8 standard deviations.

Determination of W -Boson Mass and Width

At the W -pair production threshold of $\sqrt{s} \simeq 161$ GeV, the cross section is sensitive to the mass of the W boson, used for the first measurement of m_W by the four LEP experiments [157, 158, 159, 160]. However, at higher centre-of-mass energies, the cross section flattens out and becomes independent of m_W . At these energies, where the bulk of the LEP-II luminosity was collected, the method of direct reconstruction is most sensitive in determining the mass and also the total width of the W boson.

The four fermions arising in W -pair decay are reconstructed in the detector, in particular energy and direction, and paired to form two W bosons. The invariant mass of each paired fermion system corresponds to the invariant mass of the decaying W boson, and follows a Breit-Wigner distribution convoluted with the detector resolution. A kinematic fit of the measured energies and angles, enforcing a 4-fermion final state, overall energy-momentum conservation as well as equal

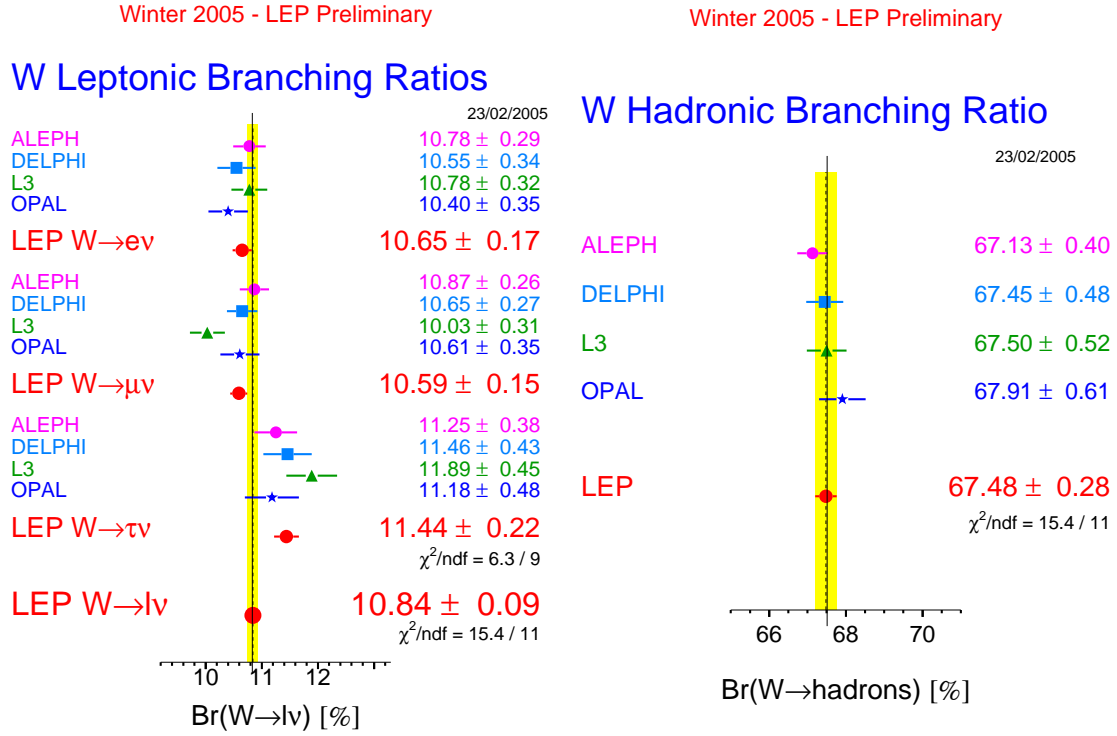


Figure 1.37: W-decay branching fractions measured by the four LEP experiments and their combination. The results are preliminary. The sum of the branching fractions is constrained to be unity. Left: branching fractions of leptonic W decays. Right: branching fractions of the inclusive hadronic W decay.

mass of the two W bosons in an event, is performed. Such a procedure allows the determination of the unmeasured neutrino kinematics in $q\bar{q}l\nu_\ell$ events and improves the resolutions in the kinematics of the measured fermions by a factor of up to four.

Spectra of reconstructed invariant masses are shown in Figure 1.38. The W-mass peak around 80 GeV is clearly visible. Its width is given by the total decay width of the W boson and the detector resolution. These distributions are analysed by the four LEP experiments in order to extract the pole mass and total decay width of the W boson [161, 162, 163, 164], where a definition of mass and width using a Breit-Wigner with s -dependent width is used. The results of the experiments for the different channels and their combinations [156] are compared in Figures 1.39 and 1.40. The combined W-mass values obtained in the $q\bar{q}l\nu_\ell$ and $q\bar{q}q\bar{q}$ channels are [156]:

$$m_W(q\bar{q}l\nu_\ell) = 80.372 \pm 0.030(\text{stat.}) \pm 0.020(\text{syst.}) \text{ GeV} \quad (43)$$

$$m_W(q\bar{q}q\bar{q}) = 80.387 \pm 0.040(\text{stat.}) \pm 0.044(\text{syst.}) \text{ GeV}, \quad (44)$$

where the two results show a correlation of 20%.

Systematic uncertainties affecting the mass measurements are compared in Table 1.21. The largest systematic uncertainty affecting both channels arises from the uncertainty in the modeling of quark fragmentation and hadronisation. In addition, the hadronic channel suffers from additional sources of uncertainty, which are related to the fact that the two hadronic W-boson decays strongly overlap in space-time. Thus, cross talk between the two hadronic system arising through the strong interaction may lead to four-momentum exchange between them so that the invariant masses of the

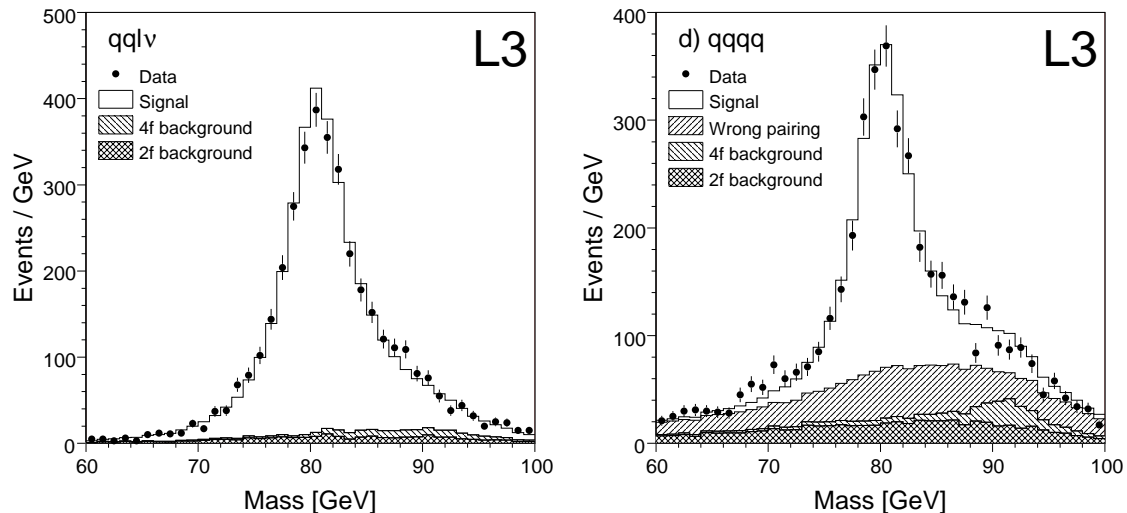


Figure 1.38: Distribution of reconstructed invariant masses from the L3 experiment. Left: $q\bar{q}\ell\nu_\ell$ final states. Right: $q\bar{q}q\bar{q}$ final states.

Table 1.21: Error decomposition for the combined LEP W mass results. Detector systematics include uncertainties in the jet and lepton energy scales and resolution. The ‘Other’ category refers to errors, all of which are uncorrelated between experiments, arising from: simulation statistics, background estimation, four-fermion treatment, fitting method and event selection.

Source	Systematic Error on m_W (MeV)		
	$q\bar{q}\ell\nu_\ell$	$q\bar{q}q\bar{q}$	Combined
Initial-/final-state radiation	8	5	7
Hadronisation	13	19	14
Detector Systematics	10	8	10
LEP Beam Energy	9	9	9
Colour Reconnection	–	35	8
Bose-Einstein Correlations	–	7	2
Other	3	11	4
Total Systematic	21	44	22
Statistical	30	40	25
Total	36	59	33
Statistical in absence of Systematics	30	27	20

visible decay products measured in the detector can not be attributed uniquely to one of the two decaying W bosons. Such FSI effects can arise due to (i) Bose-Einstein correlations (BE) between identical neutral hadrons, mainly pions, or (ii) colour-reconnection effects (CR) in the perturbative or non-perturbative evolution of the $q\bar{q}$ systems originating from the two W bosons. Dedicated studies are performed to analyse in detail particle correlations and the particle and energy flow in $q\bar{q}q\bar{q}$ events between jets to search for BE and CR effects.

In case of BE, the effects within a jet are measured to be at the same strength as observed between jets from Z boson decay, excluding b quarks as these are suppressed in W decays. Of relevance for the W mass, however, is the strength of inter- W BE. These are measured by com-

paring genuine $W^+W^- \rightarrow q\bar{q}q\bar{q}$ with two combined $W^+W^- \rightarrow q\bar{q}\ell\nu_\ell$ events where the leptons are removed. The mixed events properly contain the intra- W correlations while inter- W correlations are absent. Hence any difference to $W^+W^- \rightarrow q\bar{q}q\bar{q}$ events must be attributed to inter- W correlations. The analyses of the LEP experiments result in a combined limit of 30% in the data on the strength of a model describing such BE correlations in the Monte Carlo simulation [156]. This limit is turned into a systematic uncertainty on the mass of the W boson using the same model.

A similar strategy is followed in limiting possible CR effects. Again, for the W mass reconstruction, only inter- W effects are relevant since intra- W effects do not change the invariant mass of a hadronic system. To limit CR, the particle flow in $W^+W^- \rightarrow q\bar{q}q\bar{q}$ between jets from the same W boson is compared to that between jets from different W bosons. Interpreting the particle flow with the help of CR models allows to constrain model parameters, for example limiting the model parameter k_i describing CR in the SK-I model to a value of at most 2.13 combining the LEP analyses [156]. The consequences for the mass are then evaluated using the same SK-I model, comparing $k_i = 0$ with $k_i = 2.13$.

The difference of the W -boson masses obtained in the two channels may also indicate the presence of FSI effects. Excluding FSI related uncertainties in its calculation, the mass difference is evaluated to be -12 ± 45 MeV, showing no indication of any significant FSI effects.

The combined results for mass and total decay width of the W boson obtained by the four LEP experiments, including also the threshold measurements [157, 158, 159, 160], are [156]:

$$m_W = 80.376 \pm 0.033 \text{ GeV} \tag{45}$$

$$\Gamma_W = 2.196 \pm 0.083 \text{ GeV}, \tag{46}$$

where the contributions of the statistical and systematic errors to the total error are also reported in Table 1.21. Owing to the additional FSI errors in the $q\bar{q}q\bar{q}$ channel, the average is dominated by the $q\bar{q}\ell\nu_\ell$ channel, having a weight of 78% in the average.

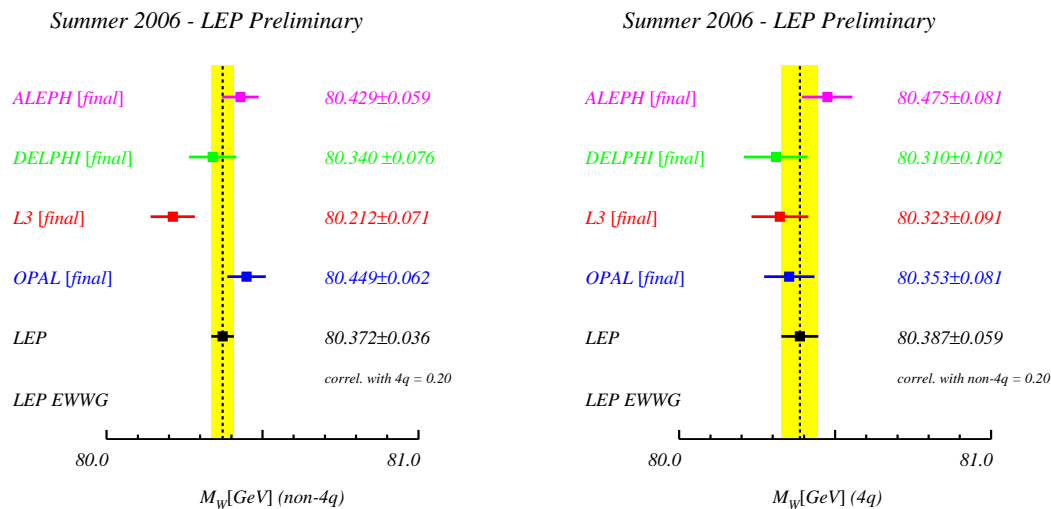


Figure 1.39: The W mass measurements from the $W^+W^- \rightarrow q\bar{q}\ell\nu_\ell$ (left) and $W^+W^- \rightarrow q\bar{q}q\bar{q}$ (right) channels obtained by the four LEP collaborations, propagating the common LEP estimates of FSI effects to the mass. The combined values take into account correlations between experiments, years and the two channels. The $q\bar{q}\ell\nu_\ell$ and $q\bar{q}q\bar{q}$ results are correlated since they are obtained from a fit to both channels taking into account inter-channel correlations. The LEP combined values and common estimates for CR uncertainties are still preliminary.

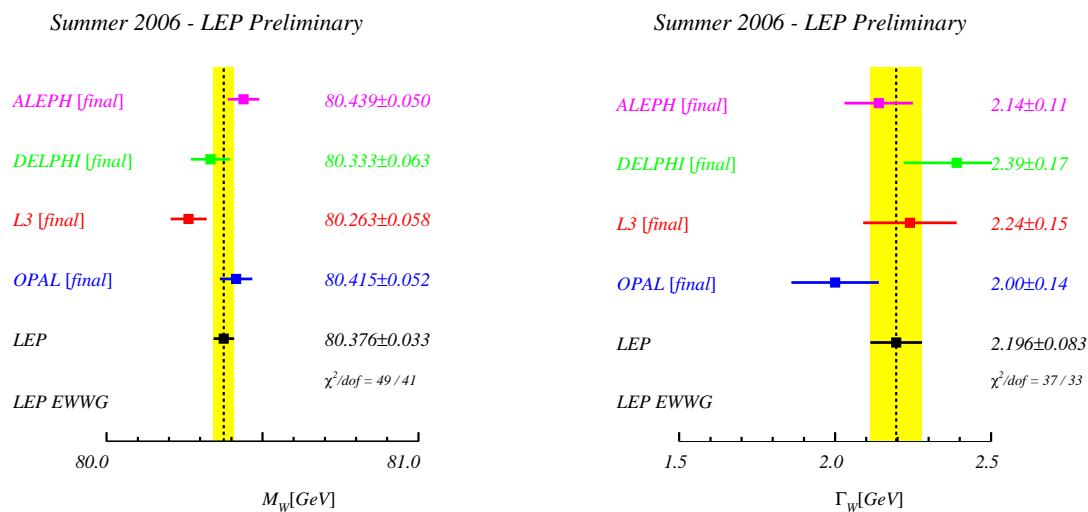


Figure 1.40: The combined results for the measurements of the W mass (left) and total W width (right) compared to the results obtained by the four LEP collaborations, propagating the common LEP estimates of FSI effects to mass and width (see text). The combined values take into account correlations between experiments and years and hence, in general, do not give the same central value as a simple average. The individual and combined m_W results include the measurements from the threshold cross section. The LEP combined values and common estimates for CR uncertainties are still preliminary.

1.4 The Top Quark

1.4.1 Top Quark Production

Currently the Tevatron collider is the only accelerator in the world powerful enough to produce top quarks. Proton-antiproton collisions produce $t\bar{t}$ pairs in the reaction $p\bar{p} \rightarrow t\bar{t} + X$ where X denotes the $p\bar{p}$ remnant recoiling against the $t\bar{t}$ system. The lowest-order Feynman diagrams on parton level contributing to this process are QCD mediated processes as shown in Figure 1.41.

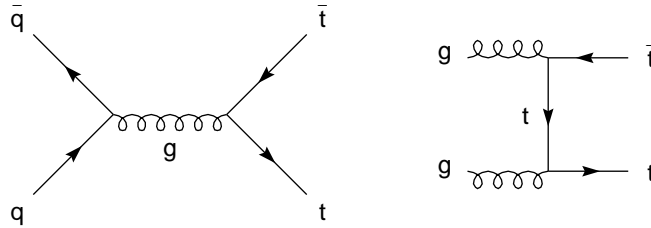


Figure 1.41: Feynman diagrams of $t\bar{t}$ production in $p\bar{p}$ collisions on parton level.

For a $p\bar{p}$ centre-of-mass energy of 1.8 TeV (1.96 TeV), the total $t\bar{t}$ production cross section is expected to be about 5.2 pb (6.7 pb), with a theoretical uncertainty of about 10% [165, 166]. About 90% (85%) of the cross section is due to the $q\bar{q}$ diagram. The top quark immediately decays via the charged-current reaction:

$$t \rightarrow bW, \quad W \rightarrow f\bar{f}' \quad (f, f' \neq t), \quad (47)$$

since the Cabibbo-Kobayashi-Maskawa matrix element V_{tb} dominates. Since $m_t > m_W + m_b$, the daughter W boson is on-shell. The total decay width of the top quark is then $\Gamma_t \propto G_F m_t^3$, for example $\Gamma_t = 1.4$ GeV for $m_t = 175$ GeV. Thus the top quark decays before there is enough time for it to combine with other quarks to form top-flavoured bound states of hadrons.

The decay modes of a $t\bar{t}$ system are those of a W -pair accompanied by a $b\bar{b}$ system. Hence, in analogy to W -pair production discussed in electron-positron collisions, fully hadronic modes, semileptonic modes and dilepton modes occur. The branching fractions for these final states are given by the corresponding products of W branching fractions:

$$t\bar{t} \rightarrow b\bar{b}W^+W^- \rightarrow b\bar{b}(f\bar{f}')_1(f\bar{f}')_2 \quad (48)$$

$$\rightarrow \begin{cases} b\bar{b}q\bar{q}'q\bar{q}' & 45.6\% \\ b\bar{b}q\bar{q}'l\nu_\ell & 14.6\% \text{ each for } \ell = e, \mu, \tau \\ b\bar{b}l\nu_\ell l\nu_\ell & 10.6\% \text{ for } \ell = e, \mu, \tau \text{ combined} \end{cases} . \quad (49)$$

Like in W and Z physics at the Tevatron, the main leptonic W decay modes analysed are $W \rightarrow e\nu_e$ and $W \rightarrow \mu\nu$, including $W \rightarrow \tau\nu$ where the tau decays to leptons. These leptons are easy to identify in the hadronic event environment and constitute an important selection tool; the more leptons, the higher the efficiency and purity. The common signature of all $t\bar{t}$ events consists of the $b\bar{b}$ system; hence in several $t\bar{t}$ analyses b -tagging is explicitly used in the event selection. On the balance of branching fraction, efficiency and purity of the selected sample, the semileptonic channel offers best prospects for high precision measurements of top-quark properties.

Electroweak single-top production, a charged weak current process mediated by W -boson exchange, has an expected cross section only slightly smaller than $t\bar{t}$ production, a strong process. However, single-top production is much harder to observe experimentally, as only one heavy

top quark is produced. Only very recently, first evidence for single-top production has been reported by DØ and also found by CDF [167, 168]. For a robust and precise mass measurement, large samples top quarks must be selected with high efficiency and purity. Hence, for the study of top-quark properties such as its mass, $t\bar{t}$ events are used.

1.4.2 Mass of the Top Quark

In $t\bar{t} \rightarrow b\bar{b}W^+W^-$ events where both W bosons decay leptonically, $t\bar{t} \rightarrow b\bar{b}\ell\nu_\ell\ell\nu_\ell$, the two unmeasured neutrinos in the event prevent a complete reconstruction of the decayed top quarks and hence a direct determination of their invariant mass. However, the mass of the top quark affects the kinematic properties of the measured decay products, such as lepton energies, quark jet energies and jet-lepton angular separations. Analysing the distribution of these observables yields a determination of m_t though with comparably large errors. While the purity of the selected event sample is high, the low branching fractions cause large statistical uncertainties.

In hadronic events, $t\bar{t} \rightarrow b\bar{b}q\bar{q}q\bar{q}$, all decay products are quarks, leading to an event signature with six jets or more due to gluon radiation and no unobserved partons. Hence the kinematics of the top quarks can be reconstructed completely, up to combinatorial ambiguities in associating light quark jets to the correct W boson, and combining W bosons with b-quark jets to top quarks. The number of combinations can be reduced by using b-tagging to identify the two b jets among the six jets, and by a matrix-element based probability assignment to find the most likely combination representing a $t\bar{t}$ decay. While the branching fraction is high, the lack of leptons to reduce the QCD multi-jet background causes low efficiencies and purities and hence limited precision in the mass determination.

In principle, semileptonic events, $t\bar{t} \rightarrow b\bar{b}q\bar{q}\ell\nu_\ell$ also allow a complete reconstruction of the invariant masses of the decaying top quarks. However, it is necessary to consider the complete production and decay chain including the hadronic system recoiling against the $t\bar{t}$ system:

$$\begin{aligned}
 p\bar{p} &\rightarrow t_1 t_2 + X_t \\
 t_1 &\rightarrow b_1 + W_1 & t_2 &\rightarrow b_2 + W_2 \\
 W_1 &\rightarrow \ell + \nu & W_2 &\rightarrow q_1 + q_2.
 \end{aligned}
 \tag{50}$$

These five four-vector equations contain seven unknown four-momenta, namely those of q_1 , q_2 , ℓ , ν , b_1 , b_2 , and X_t , corresponding to 28 unknowns. There are 17 measurements, namely the three-momenta of the five fermions q_1, q_2, ℓ, b_1, b_2 and the two transverse momentum components of the underlying event X_t . Overall four-momentum conservation, using the known masses of $\ell, \nu, q_1, q_2, b_1, b_2, W_1, W_2$ and enforcing $m_{\text{inv}}(t_1) = m_{\text{inv}}(t_2)$ introduce 13 constraints, leading to a 2C kinematic fit in the determination of all four-momenta. Nevertheless, also here combinatorial ambiguities arise in associating decay fermions to W bosons and top quarks. This channel combines high branching fractions with a lepton in the final state to allow for selection of event samples with reasonable efficiency and purity.

Example invariant mass distributions are shown in Figure 1.42 from DØ in the semileptonic channel [169], and in Figure 1.43 from CDF in the hadronic channel [170]. Figure 1.42 compares topologically selected $t\bar{t}$ events with a sample requiring in addition at least one jet tagged as a b-jet. Figure 1.43 shows the invariant mass distribution reconstructed in a sample of hadronic $t\bar{t}$ events, having required a b-tag in the event. In both cases, the b-tagging requirements lead to a significantly higher purity and a more precise mass measurement.

The mass analyses in the various final states are augmented by using neural networks on pre-selected samples, and/or the $t\bar{t}$ matrix element to assign probabilities, to resolve combinatorial ambiguities, and to increase the sensitivity to m_t by exploiting the dependence of the matrix element on m_t . Essentially, the matrix element is evaluated using the reconstructed kinematics of

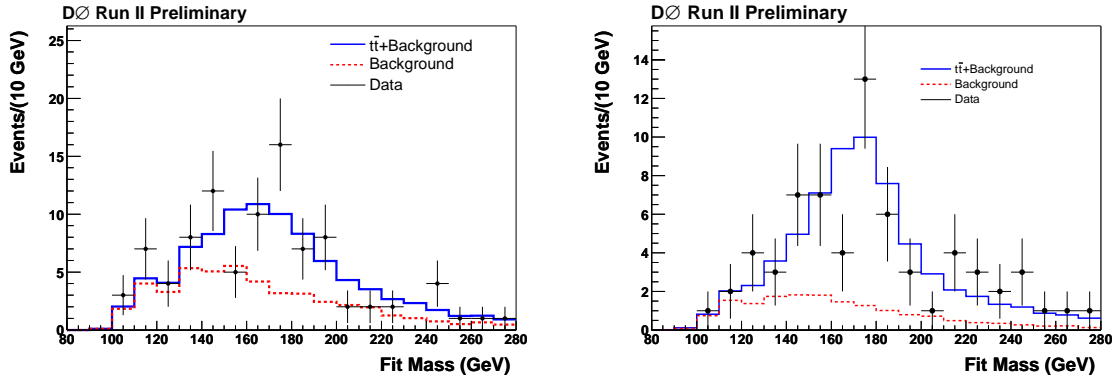


Figure 1.42: Distribution of top-quark masses reconstructed in semi-leptonic $t\bar{t}$ events selected by $D\bar{O}$ in a data sample of 230/pb, without (left) and with (right) requiring at least one jet tagged as a b-quark jet. The data is shown as dots with error bars and is compared to the MC expectations shown as lines.

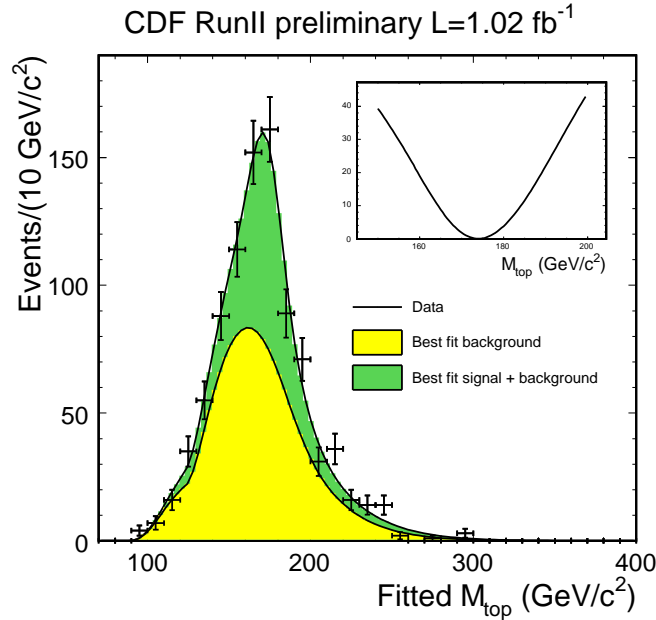


Figure 1.43: Distribution of top-quark masses reconstructed in hadronic $t\bar{t}$ events selected by CDF in a data sample of 1.02/fb, where at least one jet is tagged as b-quark jet. The data is shown as dots with error bars and is compared to the MC expectations shown as lines.

the visible fermions and the missing transverse energy as estimates for the fermion kinematics; convolutions are used to account for resolution effects, and unmeasured parameters are integrated out. The resulting differential cross section is used as a relative probability estimate to estimate correct pairings and the mass dependence. The $D\bar{O}$ collaboration pioneered the use of this computing-intensive approach in the determination of the mass of the top quark in the semileptonic channel [171].

The mass of the top quark has been measured by the Tevatron experiments CDF and $D\bar{O}$ in all channels, with various techniques, and in data collected during Run-I and Run-II of the Tevatron. For the combination, only the most precise results of each experiment in the various channels are

used, namely References [172, 173, 174, 175, 171, 176] for the final and published Run-I results, two published Run-II CDF results [177, 178], two preliminary Run-II CDF results [179, 180] and two preliminary Run-II DØ results [181, 182]. A comparison of these results, as used in the most recent combination, is shown in Figure 1.44. Taking correlated uncertainties into account, the combined result is [183]:

$$m_t = 170.9 \pm 1.8 \text{ GeV}. \quad (51)$$

The combination has a χ^2 of 9.2 for 10 degrees of freedom, which corresponds to a probability of 51%, indicating good agreement between the various measurements as also visible in Figure 1.44.

The total uncertainty contains a statistical part of 1.1 GeV and a systematic part of 1.5 GeV. The dominant part of the systematic error of each measurement is given by the jet-energy scale, i.e., the energy calibration for hadronic jets. This uncertainty alone contributes 1.1 GeV to the combined result. Recent m_t analyses use a W-mass constraint to fix the jet energy scale in situ, adjusting the jet energies such that the mass of the hadronically decaying W boson averages to the known W mass. This technique fixes the jet energy scale for light-quark jets occurring in W decays. Only energy scale of b-quark jets then remains to be calibrated relative to light-quark jets. Other important systematic uncertainties include the modelling dependence of the simulated event samples for signal and background used in the mass extraction procedure.

With the advent of new mass analysis techniques and the larger luminosity collected in Run-II, the mass of the top quark is now known with an accuracy of 1.1%, much improved compared to just a few years ago. The prediction of m_t within the SM based on the analysis of electroweak radiative corrections measured at the Z-pole is discussed in Section 1.6.3.

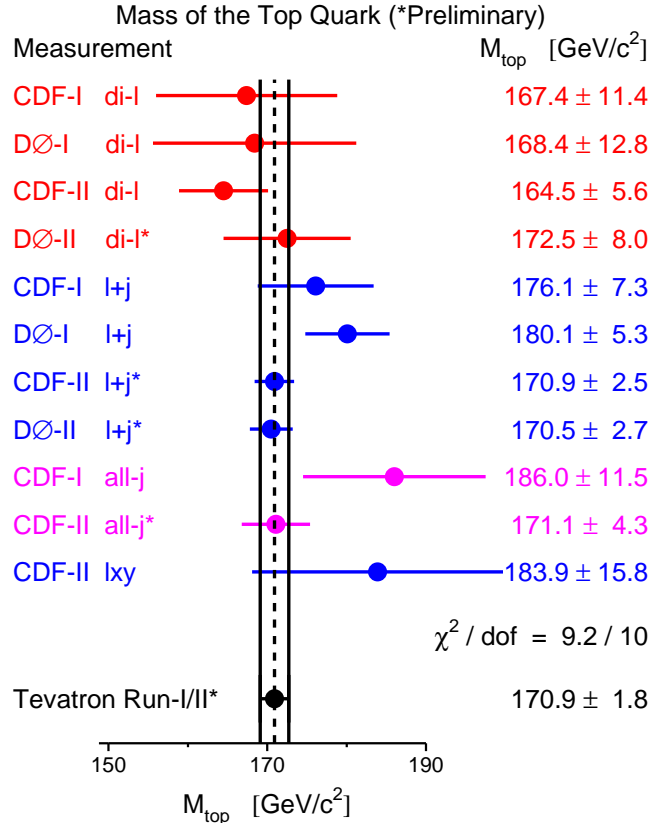


Figure 1.44: Comparison of measurements of the top-quark mass from CDF and DØ and the resulting world average mass of the top quark.

1.5 Low-Energy Measurements

Effective coupling constants of the weak current are not only measured in high- Q^2 interactions such as at the Z-pole ($Q^2 \approx m_Z^2$), but also in low- Q^2 processes, $Q^2 \ll m_Z^2$. Because of the running of effective coupling constants with Q^2 , the couplings measured in these reactions are different from those measured at the Z pole. This running has to be accounted for before comparisons can be made.

1.5.1 Parity Violation in Atoms

A parity violating effect occurs in atomic transitions due to the parity-violating t -channel γZ exchange between the shell electron and the quarks in the atomic nucleus. Its strength is given by the weak charge of the atomic nucleus as probed by the shell electron, $Q_W(Z, N) = -2[(2Z + N)C_{1u} + (Z + 2N)C_{1d}]$ for a nucleus with Z protons and N neutrons. The weak charges C_{1q} of up and down quarks can be expressed in terms of effective vector and axial-vector coupling constants introduced earlier, $C_{1q} = 2g_{Ae}g_{Vq}$.

The most precise results have been obtained from measurements with cesium [33, 34]. Over the last years, the corrections due to nuclear many-body perturbation theory and QED radiative corrections needed in the experimental analyses have been revised [35]. The newly corrected experimental results for cesium is: $Q_W(\text{Cs}) = -72.74 \pm 0.46$ [35]. This result is now in good agreement with the SM expectation.

1.5.2 Parity Violation in Møller Scattering

The weak charge of the electron, $Q_W(e) = -4g_{Ae}g_{Ve}$, is measured by Møller scattering, e^-e^- , using polarised beams. The experiment was performed at an average momentum transfer of $Q^2 = 0.026 \text{ GeV}^2$ by the E-158 collaboration at SLAC. Expressed in terms of the electroweak mixing angle, the result is [36, 37]: $\sin^2 \theta_{\text{eff}}(Q^2) = 0.2397 \pm 0.0013$ or $\sin^2 \theta_{\overline{\text{MS}}}(m_Z) = 0.2330 \pm 0.0015$ using the SM running of the electroweak mixing angle with Q^2 . The effective electroweak mixing angle, $\sin^2 \theta_{\text{eff}}^{\text{lep}}$, is obtained by adding 0.00029 [184] to $\sin^2 \theta_{\overline{\text{MS}}}(m_Z)$.

1.5.3 Neutrino-Nucleon Scattering

Neutrino-nucleon scattering allows to measure both charged weak current and neutral weak current interactions. As shown in Figure 1.45, the interactions proceed via the t -channel exchange of a W or Z boson, connecting the incoming neutrino or anti-neutrino to a quark in the nucleons of the target material.

Using both a neutrino and an anti-neutrino beam, as done for the first time by the NuTeV experiment, it is possible to exploit the Paschos-Wolfenstein relation [185]:

$$R_- = \frac{\sigma_{NC}(\nu) - \sigma_{NC}(\bar{\nu})}{\sigma_{CC}(\nu) - \sigma_{CC}(\bar{\nu})} = 4g_{L\nu}^2 \sum_{u,d} [g_{Lq}^2 - g_{Rq}^2] = \rho_\nu \rho_{ud} [1/2 - \sin^2 \theta_W^{\text{on-shell}}], \quad (52)$$

where the sum runs over the valence quarks u and d. This relation holds for iso-scalar targets and up to small electroweak radiative corrections. Thus R_- is a measurement of the on-shell electroweak mixing angle.



Figure 1.45: Feynman diagrams in neutrino-nucleon scattering on parton level. Left: charged-current reaction. Right: neutral-current reaction.

Using a muon (anti-) neutrino beam, CC reactions contain a primary muon in the final state, while NC reactions do not. The muon as a minimum ionising particle traverses the complete detector, while the hadronic shower alone is confined in a small target volume. The length of the event thus discriminates between CC and NC events. The distributions of event lengths as observed for neutrino and anti-neutrino beams are shown in Figure 1.46. In total, close to 2 million events were recorded by the NuTeV collaboration, 1167K CC and 457K NC events with neutrino beams, and 250K CC and 101K NC events with anti-neutrino beams. The separation between CC and NC events is dependent on the energy of the hadronic shower and ranges from 16 to 18 in units of counters (equivalent to 10 cm of steel) as indicated in the inserts of Figure 1.46.

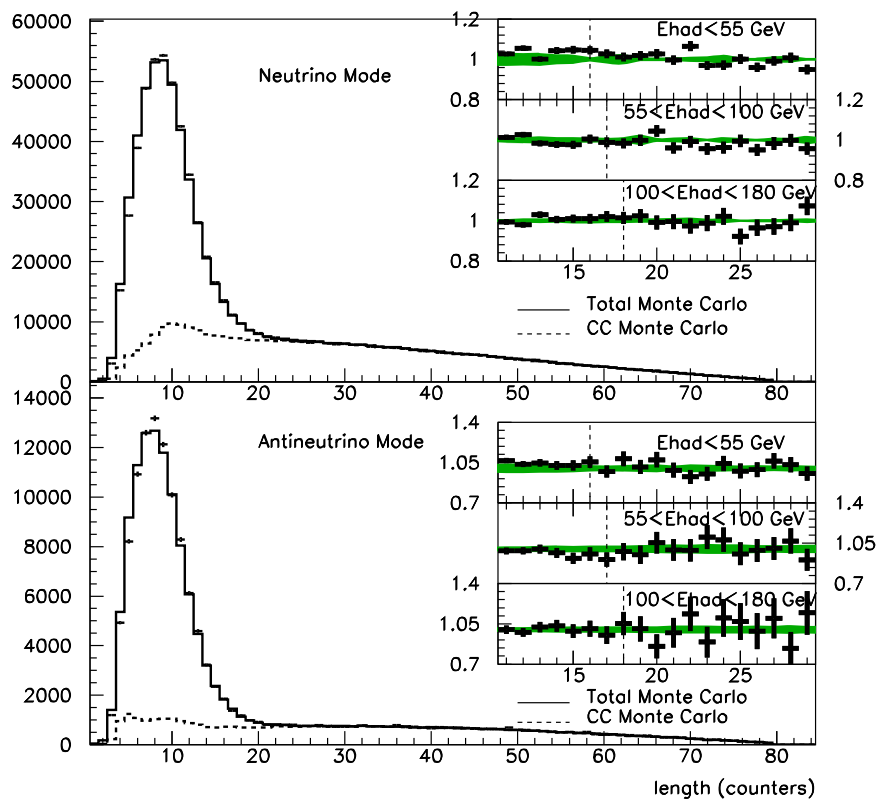


Figure 1.46: Distribution of event lengths.

In order to extract R_- from the measured distributions, a Monte Carlo simulation of the spectra of the (anti-) neutrino beams, radiative corrections and detector response is used. In terms of the on-shell electroweak mixing angle, NuTeV's final results reads [38]:

$$\sin^2 \theta_W^{on-shell} \equiv 1 - m_W^2/m_Z^2 \quad (53)$$

$$\begin{aligned} &= 0.2277 \pm 0.0013 \pm 0.0009 \\ &\quad - 0.00022 \frac{m_t^2 - (175 \text{ GeV})^2}{(50 \text{ GeV})^2} + 0.00032 \ln(m_H/150 \text{ GeV}), \end{aligned} \quad (54)$$

where the first error is statistical and the second is systematic. Here $\rho = \rho_{SM}$ is assumed. This result is a factor of two more precise than the average of all previous neutrino-nucleon measurements.

The two main contributions to the total systematic uncertainty of 0.0009 are about equal, 0.0006 each for experimental systematics and for modelling. The experimental systematics are dominated by the uncertainty on the (anti-)electron neutrino flux, as for such beams both CC and NC interactions lead to final states without primary muons. The model systematics are dominated by charm production and the strange-quark sea, effects which are much reduced compared to previous single-beam experiments. With a statistical error of 0.0013 and a total systematic error of 0.0009, NuTeV's final result is statistics limited.

When presented this result caused a great deal of excitement, as the global SM analysis of all electroweak measurements, presented later in this paper, predicts a value of 0.2232 ± 0.0004 for the on-shell electroweak mixing angle, showing a deviation from the NuTeV result at the level of 2.8 standard deviations.

In a more model-independent analysis, the NuTeV result is also interpreted in terms of effective left- and right-handed couplings, shown in Figure 1.47, defined as: $g_X^2(ef) = 4g_{L\nu}^2 \sum_q g_{Xq}^2$ for $X = L, R$. Here the deviation is confined to the effective left-handed coupling product. Modifying all ρ parameters by a scale factor ρ_0 , also shown in Figure 1.47, shows that either ρ_0 or the mixing angle, but not both, could be in agreement with the SM. Assuming the electroweak mixing angle to have its expected value, the change in the ρ factors can be absorbed in ρ_ν , *i.e.*, interpreted as a change in the coupling strength of neutrinos, then lower than expected by about $(1.2 \pm 0.4)\%$. A similar trend is observed with the neutrino coupling as measured by the invisible width of the Z boson at LEP-1, yielding a much less significant deficit of $(0.5 \pm 0.3)\%$ in ρ_ν .

To date, various explanations ranging from old and new physics effects have been put forward. Some old physics effects are: theoretical uncertainties in PDFs, iso-spin violating PDFs, quark-antiquark asymmetries for sea quarks, nuclear shadowing asymmetries between W and Z interactions, etc. Some new physics effects are: a new heavy Z boson, contact interactions, leptokuarks, new fermions, neutrinos oscillations, etc. Most of the old and new physics effects are, however, severely constrained by NuTeV itself or other precision electroweak measurements, thus cannot explain the full effect. It seems, however, that PDF uncertainties should be investigated, and in particular the partly leading-order analysis employed by NuTeV should be assessed and eventually improved to next-to-leading order.

1.5.4 Anomalous Magnetic Moment of the Muon

The Pauli and Dirac equations of quantum mechanics describe pointlike spin-1/2 particles of mass m with a magnetic moment $\vec{\mu} = (g/2)(e/m)\vec{S}$ where g is predicted to be 2. In quantum field theory, small corrections to g arise, leading to a non-zero so-called anomalous magnetic moment, $a = (g - 2)/2 \neq 0$. Recently, a precision measurement of the anomalous magnetic moment for muons was performed by the experiment E821 in Brookhaven, which measured the precession of the muon spin relative to its direction of flight, ω_a , when moving on a circular orbit in a homogeneous

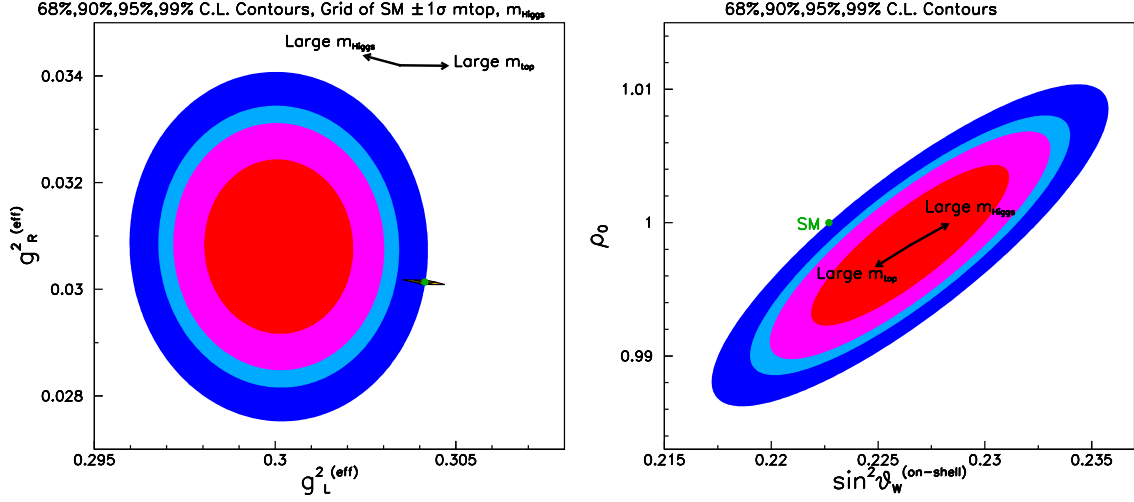


Figure 1.47: NuTeV result in the plane of (left:) effective right- and left-handed couplings, and (right:) on-shell angle versus ρ -scale factor ρ_0 . In both cases, the SM expectation is shown as the small dot located at the outer-most contour edge.

magnetic field:

$$\omega_a = \omega_s - \omega_c = a_\mu \frac{eB}{m_\mu}, \quad (55)$$

where ω_s and ω_c are the spin precession and cyclotron frequencies, respectively. In a storage ring, electric fields are also present which are felt by the moving muon as additional magnetic fields due to the Lorentz transformation from laboratory system to muon system, modifying the above equation:

$$\omega_a = \frac{e}{m_\mu} \left[a_\mu B - \left(a_\mu - \frac{1}{\gamma^2 - 1} \right) \frac{\beta E}{c} \right]. \quad (56)$$

The additional term vanishes for $\gamma = 29.30$ corresponding to the “magic” muon momentum of 3.094 GeV, establishing the working point used by all a_μ measurements to suppress the effect of electric fields.

Longitudinally polarised muons are injected into the storage ring with the magic momentum, leading to a time-dilated lifetime of $64.4\mu\text{s}$. The muon decays through the charged weak current into an electron and two neutrinos. Because of the parity violation of the charged weak current, the muon spin is correlated with the direction of flight of the electron. This correlation allows the muon spin to be measured by observing the electron signal at a fixed direction from the muon beam. The E821 experiment used 24 electromagnetic calorimeters, placed symmetrically along the inside of the storage ring, to measure the time of the muon decay and the decay electron energy. The distribution of events as a function of time is shown in Figure 1.48, showing the exponential decay following the time-dilated muon lifetime, modulated by the relative precession frequency ω_a :

$$N(t) = N_0 \exp(-t/\gamma\tau_\mu) [1 - A \cos(\omega_a t - \phi)], \quad (57)$$

where N_0 , A and ϕ implicitly depend on the electron energy threshold, 1.8 GeV for E821, used to select events.

Measurements of ω_a and hence a_μ were made by E821 for both positive and negative muons, and found to be in good agreement as expected from CPT invariance, with an average value of [32]:

$$a_\mu = (116592080 \pm 63) \cdot 10^{-11}, \quad (58)$$

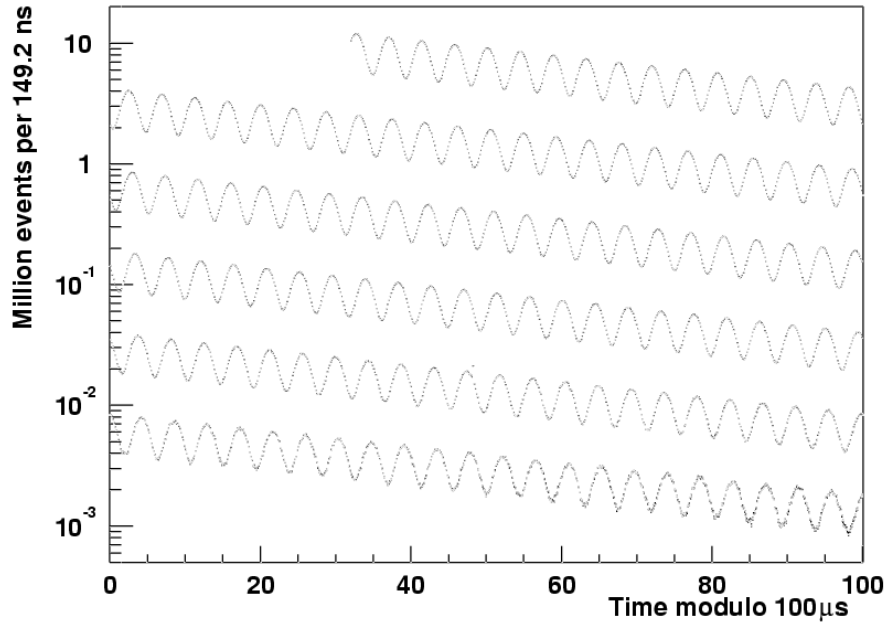


Figure 1.48: Distribution of electron counts as a function of time. The data is wrapped every $100\mu\text{s}$.

a 0.54 ppm measurement. The total uncertainty combines a statistical error of 54 units and a systematic error of 33 units in quadrature.

The expected value of a_μ is calculated within the SM to similar precision, allowing to test the theory. Since the SM calculation is sensitive to the full particle content of the theory through loops of virtual particles, any measured excess could indicate the existence of new particles not found so far. Typical diagrams contributing to the calculation are shown in Figure 1.49, and are classified as pure QED, weak, hadronic and light-by-light diagrams. The pure QED contribution is by far the dominant term but known extremely precisely [186, 187]. The weak [188], hadronic [189, 190, 191] and light-by-light [188] contributions are all much smaller but have larger uncertainties. Adding all contributions, the error on the SM calculations [189, 190, 191] is dominated by the leading-order hadronic contribution (6-7 units, depending on calculation), followed by the hadronic light-by-light contribution (3.5 units). The measured value turns out to be larger than the SM expectation at the level of 2.2 to 2.7 standard deviations [32], depending on calculation.

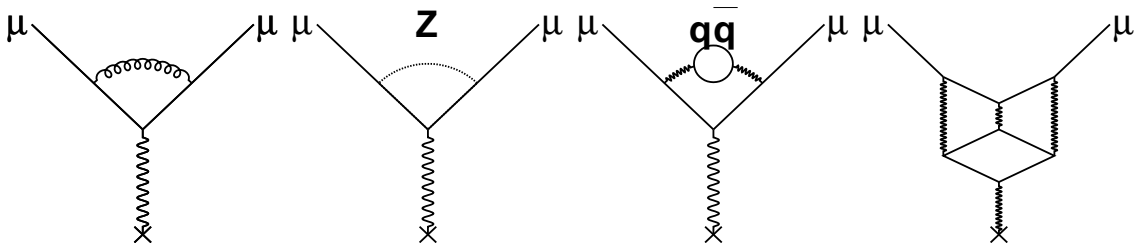


Figure 1.49: Contributions to the SM calculation of a_μ , from left to right: QED, weak, hadronic, light-by-light diagrams.

1.6 Constraints on the Standard Model

1.6.1 Introduction

The SM expectations for the various observables discussed so far depend on the free parameters of the SM theory, as shown in many preceding figures. This dependence exists already at Born level or is introduced by radiative corrections involving virtual particles, and needs to be taken into account in precision calculations. Conversely, the measurement results can be used to constrain these free parameters. For the measurements discussed here, there are five main SM parameters on which the predictions depend, conventionally chosen as: (i) the hadronic vacuum polarisation $\Delta\alpha_{\text{had}}^{(5)}(m_Z^2)$ contributing to the running of the electromagnetic coupling constant $\alpha(m_Z^2)$, (ii) the coupling constant of the strong interaction, $\alpha_S(m_Z^2)$, determining QCD corrections, (iii) the mass m_Z of the Z boson, (iv) the mass m_t of the top quark, and (v) the mass m_H of the as yet unobserved Higgs boson.

The hadronic vacuum polarisation is determined in dedicated analyses, using experimental results only [192, 193, 194], or also theory constraints introducing some model dependence but leading to higher precision [195, 205]. In the following, we use the experimentally driven result [194]:

$$\Delta\alpha_{\text{had}}^{(5)}(m_Z^2) = 0.02758 \pm 0.00035, \quad (59)$$

but in some cases also illustrate the effect of using the more precise theory-driven result [205]:

$$\Delta\alpha_{\text{had}}^{(5)}(m_Z^2) = 0.02749 \pm 0.00012. \quad (60)$$

1.6.2 Z-Pole Results

Using only the Z-pole measurements of Section 1.2 together with the hadronic vacuum polarisation, the five SM parameters are determined in a χ^2 fit of the theory predictions to the measured results, taking uncertainties and correlations properly into account. The fit has a χ^2/dof of 16.0/10, corresponding to a probability of 9.9%. The results of the fit are reported in Table 1.22.

Table 1.22: Results for the five SM input parameters derived from a fit to the Z-pole results and $\Delta\alpha_{\text{had}}^{(5)}(m_Z^2)$. The results on m_H , obtained by exponentiating the fit results on $\log_{10}(m_H/\text{GeV})$, are also shown.

Parameter	Value	Correlations				
		$\Delta\alpha_{\text{had}}^{(5)}(m_Z^2)$	$\alpha_S(m_Z^2)$	m_Z	m_t	$\log_{10}(m_H/\text{GeV})$
$\Delta\alpha_{\text{had}}^{(5)}(m_Z^2)$	0.02759 ± 0.00035	1.00				
$\alpha_S(m_Z^2)$	0.1190 ± 0.0027	-0.04	1.00			
m_Z [GeV]	91.1874 ± 0.0021	-0.01	-0.03	1.00		
m_t [GeV]	$173 \pm_{10}^{13}$	-0.03	0.19	-0.07	1.00	
$\log_{10}(m_H/\text{GeV})$	$2.05 \pm_{0.34}^{0.43}$	-0.29	0.25	-0.02	0.89	1.00
m_H [GeV]	$111 \pm_{60}^{190}$	-0.29	0.25	-0.02	0.89	1.00

The fitted hadronic vacuum polarisation is nearly unchanged compared to the input measurement Equation 59, showing that the data has only a low sensitivity to it. However, the parameter

is crucial in the determination of the mass of the Higgs boson as evidenced from the sizeable correlation coefficient of 0.89. The fitted strong coupling constant is one of the most precise determination of this quantity, and in good agreement with other determinations [206, 184]. The mass of the Z boson in this SM analysis is identical to that derived in the model-independent analysis of Section 1.2, but now m_Z changed its role to a parameter of the theory, in terms of which all other observables are calculated. Even though Z-pole radiative corrections are sensitive to $\log_{10}(m_H/\text{GeV})$ only, the mass of the Higgs boson is nevertheless constrained within a factor of two and lies in the region below 1 TeV as required by theory, showing the self-consistency of this analysis.

1.6.3 The Mass of the Top Quark and of the W Boson

The results on the mass and total width of the W boson obtained at LEP-II and the Tevatron and presented in Section 1.3 are in good agreement, as shown in Figure 1.50. The results are combined assuming no correlations between the two sets of results, yielding preliminary world averages of:

$$m_W = 80.398 \pm 0.025 \text{ GeV} \quad (61)$$

$$\Gamma_W = 2.140 \pm 0.060 \text{ GeV} . \quad (62)$$

Based on the analysis reported in Table 1.22, the mass of the W boson is predicted to be $m_W = 80.363 \pm 0.032 \text{ GeV}$. The prediction of m_W is greatly improved when the direct measurement of the mass of the top quark, Section 1.4, is also used in its calculation, with the result: $m_W = 80.360 \pm 0.020 \text{ GeV}$. This result must be compared with the direct measurements of m_W performed at the Tevatron and LEP-II given above, $m_W = 80.398 \pm 0.025 \text{ GeV}$. The different results on m_W are compared in Figure 1.50 (left). The agreement between the prediction and the direct measurement is good, constituting an important and successful test of the electroweak SM.

The mass of the top quark is found with an accuracy of about 12 GeV: $m_t = 173_{-10}^{+13} \text{ GeV}$ as given in Table 1.22. This result must be compared with the direct measurement of m_t at the Tevatron, with the most recent combined preliminary result of $m_t = 170.9 \pm 1.8 \text{ GeV}$ as presented in Section 1.4. The good agreement constitutes another important and successful test of the electroweak SM. The prediction of the top-quark mass is improved slightly when the latest results on the mass and width of the W boson are also used in its determination: $m_t = 179_{-9}^{+12} \text{ GeV}$. Historically, this type of analysis was used to predict the mass of the top quark before it was discovered at the Tevatron; a historical perspective is illustrated in 1.51. The most recent results on m_t are compared in Figure 1.50 (right).

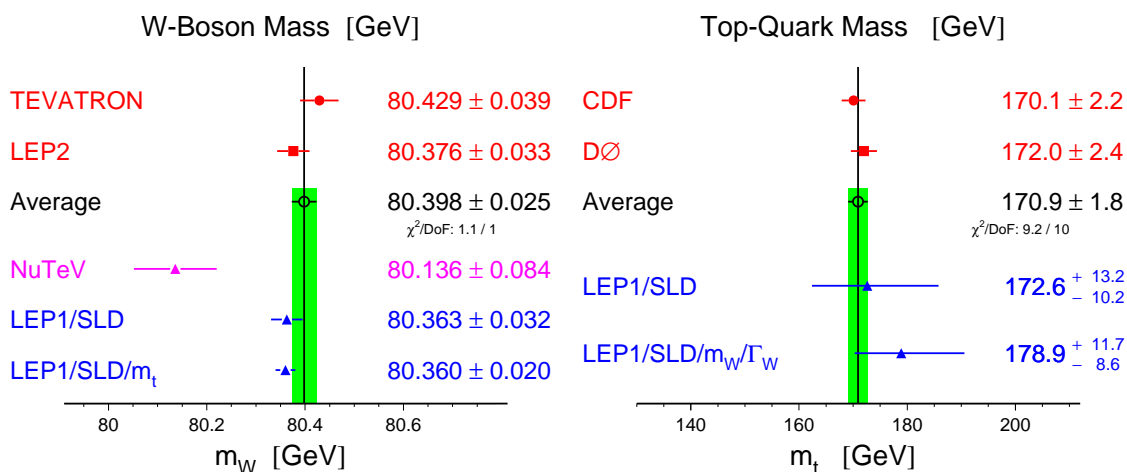


Figure 1.50: Left: results on the mass of the W boson, m_W . The direct measurements of m_W at LEP-II (preliminary) and at Run-I of the Tevatron (top) are compared with the indirect determinations (bottom). The NuTeV result interpreted in terms of m_W is shown separately. Right: results on the mass of the top quark. The direct measurements of m_t at Run-I of the Tevatron (top) are compared with the indirect determinations (bottom).

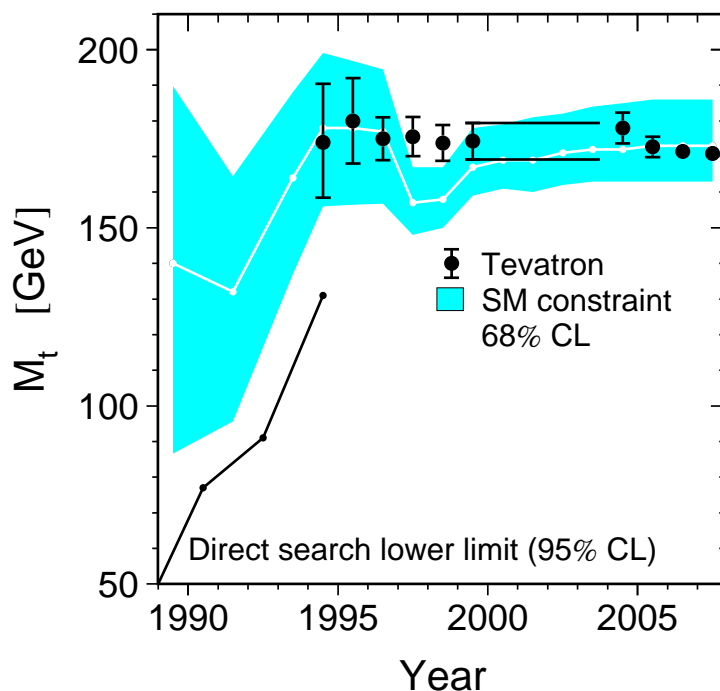


Figure 1.51: Comparison of direct and indirect determinations of the mass of the top quark, m_t , as a function of time. The shaded area denotes the indirect determination of m_t at 68% confidence level derived from the analysis of radiative corrections within the framework of the SM using precision electroweak measurements. The dots with error bars at 68% confidence level denote the direct measurements of m_t performed by the Tevatron experiments. Also shown is the 95% confidence level lower limit on m_t from direct searches before the discovery of the top quark.

1.6.4 The Mass of the Higgs Boson

The predictions of the masses of heavy fundamental particles, such as top quark and W boson, turned out to be very successful as the predictions agree well with the direct measurements. These analyses clearly demonstrate the predictive power of the electroweak SM as well as the precision achieved by the experimental measurements. Building on this success, the mass of the as yet unobserved Higgs boson of the minimal SM will be predicted. As a first step, Figure 1.52 shows the comparison between the direct and indirect determinations of m_t and m_W in the (m_t, m_W) plane. As already discussed, both sets of measurements agree well as shown by the overlapping contour curves. Within the SM, m_t and m_W are correlated quantities which is driven by the Fermi constant G_F . The exact correlation depends crucially on the mass of the Higgs boson, which can thus be determined with increased precision from both sets of results.

Including also the direct measurements of the top quark and of the mass and width of the W boson, the SM analysis yields the results as reported in Table 1.23. The χ^2 fit to the experimental results is 18.2 for 13 degrees of freedom, corresponding to a probability of 15%. The pulls of the measurements relative to the fit results are listed in Table 1.24 and shown in Figure 1.53. The largest pull occurs for the forward-backward asymmetry measured in the reaction $e^+e^- \rightarrow b\bar{b}$ at the Z pole, another consequence of the effects observed in the b-quark sector and already discussed in Sections 1.2.5 and 1.2.7.

The $\Delta\chi^2(m_H) = \chi_{min}^2(m_H) - \chi_{min}^2$ curve is shown in Figure 1.54. Compared to the results shown in Table 1.22, the relative uncertainty on m_H is decreased by more than a factor of two. Theoretical uncertainties in the SM calculations of the expectations, due to missing higher-order corrections, are shown as the shaded area around the thin solid curve. Including these theoretical uncertainties, the one-sided 95% CL upper limit on $\log_{10}(m_H/\text{GeV})$ ($\Delta\chi^2 = 2.7$) is:

$$m_H < 144 \text{ GeV}. \quad (63)$$

This limit increases to 182 GeV when the lower limit of 114 GeV [207] from the direct search for the Higgs boson at LEP-II, shown as the shaded rectangle in Figure 1.54, is taken into account. The determination of the limit on the Higgs mass is only marginally affected by using the theory-driven determination of $\Delta\alpha_{\text{had}}^{(5)}(m_Z^2)$, Equation 60.

The analyses of the high- Q^2 results are now used to predict the values of observables measured in low- Q^2 reaction such as those discussed in Section 1.5. Measured results and predictions are compared in Table 1.25. In general, good agreement is observed except for the result on the left-handed quark coupling combination $g_{\nu\text{Lud}}^2$, measured by the NuTeV experiment eight times more precisely than $g_{\nu\text{Rud}}^2$. The difference to the expected result is at the level of three standard deviations. However, the determination of the Higgs mass and its limit is only marginally affected when including the low- Q^2 results, as visible in Figure 1.54.

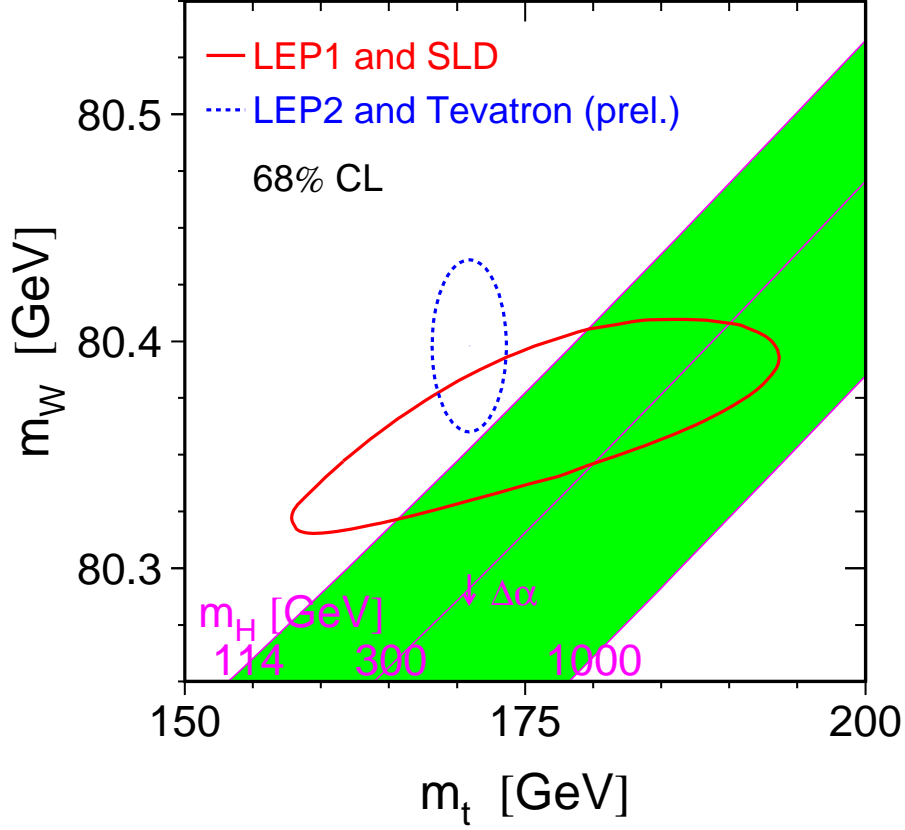


Figure 1.52: Contour curves of 68% probability in the (m_t, m_W) plane. The shaded band shows the SM prediction based on the value for G_F for various values of the Higgs-boson mass and fixed $\Delta\alpha_{\text{had}}^{(5)}(m_Z^2)$; varying the hadronic vacuum polarisation by $\Delta\alpha_{\text{had}}^{(5)}(m_Z^2) = 0.02758 \pm 0.00035$ yields an additional uncertainty on the SM prediction shown by the arrow labeled $\Delta\alpha$.

Table 1.23: Results for the five SM input parameters derived from a fit to the Z-pole results and $\Delta\alpha_{\text{had}}^{(5)}(m_Z^2)$, plus m_t , m_W , and Γ_W from Tevatron Run-I and LEP-II. The results on m_H , obtained by exponentiating the fit results on $\log_{10}(m_H/\text{GeV})$, are also shown.

Parameter	Value	Correlations				
		$\Delta\alpha_{\text{had}}^{(5)}(m_Z^2)$	$\alpha_S(m_Z^2)$	m_Z	m_t	$\log_{10}(m_H/\text{GeV})$
$\Delta\alpha_{\text{had}}^{(5)}(m_Z^2)$	0.02768 ± 0.00034	1.00				
$\alpha_S(m_Z^2)$	0.1185 ± 0.0026	0.03	1.00			
m_Z [GeV]	91.1875 ± 0.0021	0.00	-0.02	1.00		
m_t [GeV]	171.3 ± 1.7	-0.01	0.03	-0.02	1.00	
$\log_{10}(m_H/\text{GeV})$	1.88 ± 0.16	-0.54	0.06	0.09	0.39	1.00
m_H [GeV]	76^{+33}_{-24}	-0.54	0.06	0.09	0.39	1.00

Table 1.24: Summary of measurements included in the analyses of the five SM input parameters. The top 15 results are included in the Z-pole and the high- Q^2 fit, while the bottom three results are only used in the high- Q^2 fit. The total errors in column 2 include the systematic errors listed in column 3. The SM results in column 4 and the pulls (absolute value of the difference between measurement and fit in units of the total measurement error, see Figure 1.53) in column 5 are derived from the SM analysis of all 18 results.

^(a)Only common systematic errors are indicated.

	Measurement with Total Error	Systematic Error	Standard Model High- Q^2 Fit	Pull
$\Delta\alpha_{\text{had}}^{(5)}(m_Z^2)$ [194]	0.02758 ± 0.00035	0.00034	0.02766 ± 0.00035	0.2
m_Z [GeV]	91.1875 ± 0.0021	^(a) 0.0017	91.1875 ± 0.0021	0.0
Γ_Z [GeV]	2.4952 ± 0.0023	^(a) 0.0012	2.4957 ± 0.0015	0.2
σ_{had}^0 [nb]	41.540 ± 0.037	^(a) 0.028	41.477 ± 0.014	1.7
R_ℓ^0	20.767 ± 0.025	^(a) 0.007	20.744 ± 0.018	0.9
$A_{\text{FB}}^{0,\ell}$	0.0171 ± 0.0010	^(a) 0.0003	0.01645 ± 0.00023	0.7
+ correlation matrix Table 1.1				
$\mathcal{A}_\ell (P_\tau)$	0.1465 ± 0.0033	0.0015	0.1481 ± 0.0010	0.5
\mathcal{A}_ℓ (SLD)	0.1513 ± 0.0021	0.0011	0.1481 ± 0.0010	1.5
R_b^0	0.21629 ± 0.00066	0.00050	0.21586 ± 0.00006	0.7
R_c^0	0.1721 ± 0.0030	0.0019	0.1722 ± 0.0001	0.0
$A_{\text{FB}}^{0,b}$	0.0992 ± 0.0016	0.0007	0.1038 ± 0.0007	2.9
$A_{\text{FB}}^{0,c}$	0.0707 ± 0.0035	0.0017	0.0743 ± 0.0006	1.0
\mathcal{A}_b	0.923 ± 0.020	0.013	0.9347 ± 0.0001	0.6
\mathcal{A}_c	0.670 ± 0.027	0.015	0.6684 ± 0.0005	0.1
+ correlation matrix Table 1.10				
$\sin^2 \theta_{\text{eff}}^{\text{lep}t} (Q_{\text{FB}}^{\text{had}})$	0.2324 ± 0.0012	0.0010	0.23138 ± 0.00013	0.8
m_t [GeV] (Run-I+II [183])	170.9 ± 1.8	1.5	171.3 ± 1.7	0.2
m_W [GeV]	80.398 ± 0.025		80.374 ± 0.015	1.0
Γ_W [GeV]	2.140 ± 0.060		2.092 ± 0.002	0.8
+ correlation given in Section 1.6.3				

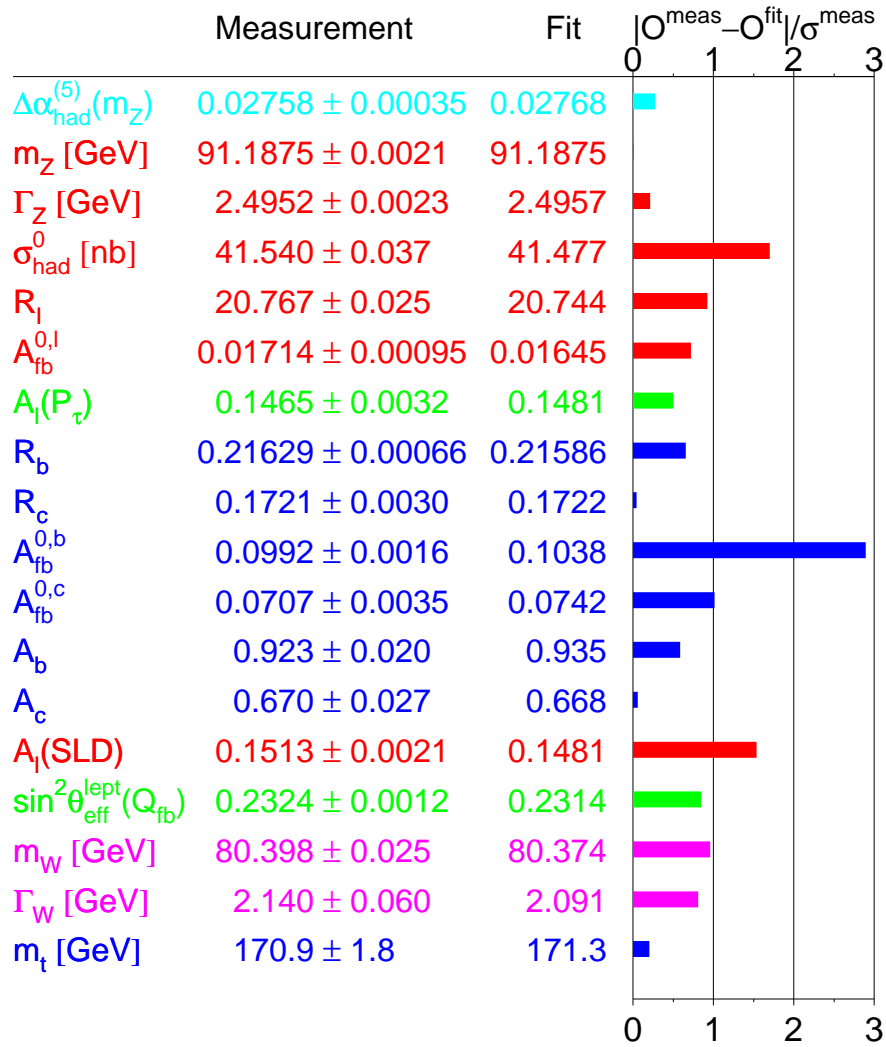


Figure 1.53: Comparison of the measurements with the expectation of the SM, calculated for the five SM input parameter values in the minimum of the global χ^2 of the fit. Also shown is the pull of each measurement, where pull is defined as the absolute value of the difference of measurement and expectation in units of the measurement uncertainty.

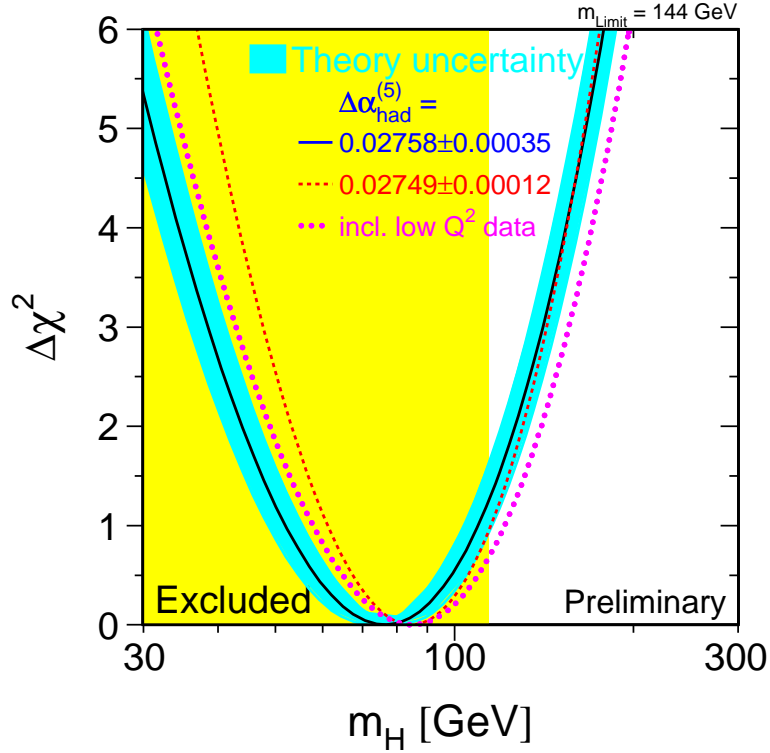


Figure 1.54: $\Delta\chi^2(m_H) = \chi_{min}^2(m_H) - \chi_{min}^2$ as a function of m_H . The line is the result of the fit using all 18 results. The associated band represents the estimate of the theoretical uncertainty due to missing higher-order corrections. The vertical band shows the 95% confidence level exclusion limit on m_H of 114.4 GeV derived from the direct search at LEP-II [207]. The dashed curve is the result obtained using the theory-driven $\Delta\alpha_{had}^{(5)}(m_Z^2)$ determination of Equation 60.

Table 1.25: Summary of predictions for results obtained in low- Q^2 processes described in Section 1.5, derived from the fit to all high- Q^2 data.

	Measurement with Total Error	Standard Model High- Q^2 Fit	Pull
APV [35]			
$Q_W(\text{Cs})$	-72.74 ± 0.46	-72.899 ± 0.032	0.4
Møller [37]			
$\sin^2 \theta_{\overline{\text{MS}}}(m_Z)$	0.2330 ± 0.0015	0.23109 ± 0.00013	1.3
νN [38]			
$g_{\nu\text{Lud}}^2$	0.30005 ± 0.00137	0.30391 ± 0.00016	2.8
$g_{\nu\text{Rud}}^2$	0.03076 ± 0.00110	0.03011 ± 0.00003	0.6

1.7 Summary and Conclusion

Over the last two decades, a large body of high-precision measurements became available, testing the SM of electroweak interactions both at Born level but also, very importantly, at loop-level. In general, the many precise results presented here are in good agreement with the SM expectations, thus constraining any hypothetical theories beyond it. The notable exceptions, all at the level of about three standard deviations, are: (i) the (final) forward-backward asymmetry in $e^+e^- \rightarrow b\bar{b}$ measured at the Z pole, (ii) the (still preliminary) leptonic W-decay branching fractions measured in $e^+e^- \rightarrow W^+W^-$ at LEP-II, and (iii) the left-handed quark couplings combination measured in neutrino-nucleon scattering by the NuTeV experiment. While the first two are likely to be of statistical nature, the last one may also be explained through an improved theoretical understanding of hadronic physics inside the atomic nucleus.

The precision measurements test the theory at loop level, verifying the SM as a renormalisable field theory correctly describing nature. The data impose very tight constraints on any new physics beyond the SM. Any extended theory must be consistent with the SM or one or more Higgs doublet models such as super-symmetry. Masses of heavy fundamental particles are predicted from the analysis of reactions where these particles are not directly produced but occur as virtual particles in loops contributing to the process under study. The predictions of W-boson mass and top-quark mass agree well with the direct measurements, constituting crucial tests of the electroweak SM. In addition, the mass of the as yet unobserved Higgs boson is constrained, with the result: $m_H < 144$ GeV at 95% confidence level. The direct observation of the Higgs boson and the measurement of its mass, expected for the next few years, will complete this domain of the electroweak interaction, but may also lead to new surprises.

1.7.1 Prospects for the Future

The next generation of high-energy particle colliders consists of the Large Hadron Collider (LHC), and the planned International Linear Collider (ILC). The LHC, a proton-proton collider with a centre-of-mass energy of 14 TeV, will start operations at the end of this year (2007). The ILC, a linear electron-positron collider with a centre-of-mass energy of 500 GeV to 1000 GeV, is currently in the design phase.

The upper limit on the Higgs mass indicated above opens a window of opportunity for the Tevatron experiments CDF and DØ to find the Higgs boson, but only the LHC is powerful enough to cover the entire mass range of the SM Higgs boson allowed by theory - or to find alternative signs for physics governing electroweak symmetry breaking. The high centre-of-mass energy also gives the LHC a wide range in searching for new massive particles beyond the Higgs, such as supersymmetric particles. The LHC is a W/Z/top factory, allowing for high-statistics measurements in any final state with leptons. In contrast, the ILC is a precision machine allowing to make highly accurate measurements in both leptonic and hadronic channels, covering all possible decay modes of new heavy states in the clean environment of an e^+e^- collider. The smaller centre-of-mass energy limits its mass reach compared to the LHC, but the ILC is essential to be able to survey and measure precisely all properties of the Higgs boson and other new particles found at the LHC, setting the stage for detailed comparisons with theoretical models.

1.8 Acknowledgements

The author thanks the members of the LEP, SLD and Tevatron electroweak working groups, as well as Guido Altarelli and Tord Riemann, for valuable and stimulating discussions.

1.9 References

- 1 S. L. Glashow, Nucl. Phys. **22** (1961) 579
- 2 S. Weinberg, Phys. Rev. Lett. **19** (1967) 1264
- 3 A. Salam, Weak and Electromagnetic Interactions, p. 367, in Elementary Particle Theory, Proceedings of the 1968 Nobel Symposium, ed. N. Svartholm, (Almquist and Wiksells, Stockholm, 1968)
- 4 M. Veltman, Nucl. Phys. **B7** (1968) 637
- 5 G. 't Hooft, Nucl. Phys. **B35** (1971) 167
- 6 G. 't Hooft and M. Veltman, Nucl. Phys. **B44** (1972) 189
- 7 G. 't Hooft and M. Veltman, Nucl. Phys. **B50** (1972) 318
- 8 SLD Collaboration, M. J. Fero *et al.*, Nucl. Instrum. Meth. **A367** (1995) 111
- 9 SLD Collaboration, D. Axen *et al.*, Nucl. Instrum. Meth. **A328** (1993) 472
- 10 SLD Collaboration, K. Abe *et al.*, Nucl. Instrum. Meth. **A343** (1994) 74
- 11 SLD Collaboration, S. C. Berridge *et al.*, IEEE Trans. Nucl. Sci. **39** (1992) 1242
- 12 *SLAC Linear Collider Conceptual Design Report, SLAC-R-229*, Internal report, SLAC, 1980
- 13 ALEPH Collaboration, D. Decamp *et al.*, Nucl. Instrum. Meth. **A294** (1990) 121–178
- 14 ALEPH Collaboration, D. Buskulic *et al.*, Nucl. Instrum. Meth. **A360** (1995) 481–506
- 15 DELPHI Collaboration, P. Aarnio *et al.*, Nucl. Instrum. Meth. **A303** (1991) 233–276
- 16 DELPHI Collaboration, P. Abreu *et al.*, Nucl. Instrum. Meth. **A378** (1996) 57–100
- 17 L3 Collaboration, B. Adeva *et al.*, Nucl. Instrum. Meth. **A289** (1990) 35–102
- 18 M. Acciarri *et al.*, Nucl. Instrum. Meth. **A351** (1994) 300–312
- 19 M. Chemarin *et al.*, Nucl. Instrum. Meth. **A349** (1994) 345–355
- 20 A. Adam *et al.*, Nucl. Instrum. Meth. **A383** (1996) 342–366
- 21 OPAL Collaboration, K. Ahmet *et al.*, Nucl. Instrum. Meth. **A305** (1991) 275–319
- 22 OPAL Collaboration, P. P. Allport *et al.*, Nucl. Instrum. Meth. **A324** (1993) 34–52
- 23 OPAL Collaboration, P. P. Allport *et al.*, Nucl. Instrum. Meth. **A346** (1994) 476–495
- 24 OPAL Collaboration, B. E. Anderson *et al.*, IEEE Trans. Nucl. Sci. **41** (1994) 845–852
- 25 *LEP Design Report, CERN-LEP/84-01*, Internal report, CERN, 1984,
The main features of LEP have been reviewed by:
- 26 S. Myers and E. Picasso, Contemp. Phys. **31** (1990) 387–403
- 27 D. Brandt *et al.*, Rept. Prog. Phys. **63** (2000) 939–1000,
A useful retrospective view of the accelerator is presented in:
- 28 R. Assmann, M. Lamont, and S. Myers, Nucl. Phys. Proc. Suppl. **109B** (2002) 17–31

-
- 29 CDF Collaboration, F. Abe *et al.*, Nucl. Instr. Meth. **A271** (1988) 387–403
- 30 D0 Collaboration, S. Abachi *et al.*, Nucl. Instrum. Meth. **A338** (1994) 185–253
- 31 D0 Collaboration, V. M. Abazov *et al.*, Nucl. Instrum. Meth. **A565** (2006) 463–537
- 32 Muon G-2 Collaboration, G. W. Bennett *et al.*, Phys. Rev. **D73** (2006) 072003
- 33 C. S. Wood *et al.*, Science **275** (1997) 1759
- 34 S. C. Bennett and C. E. Wieman, Phys. Rev. Lett. **82** (1999) 2484–2487
- 35 J. S. M. Ginges and V. V. Flambaum, Phys. Rept. **397** (2004) 63–154
- 36 SLAC E158 Collaboration, P. Anthony *et al.*, Phys. Rev. Lett. **92** (2004) 181602
- 37 SLAC E158 Collaboration, P. L. Anthony *et al.*, Phys. Rev. Lett. **95** (2005) 081601
- 38 NuTeV Collaboration, G. P. Zeller *et al.*, Phys. Rev. Lett. **88** (2002) 091802, erratum: 90 (2003) 239902
- 39 G. Montagna *et al.*, Nucl. Phys. **B401** (1993) 3–66
- 40 G. Montagna *et al.*, Comput. Phys. Commun. **76** (1993) 328–360
- 41 G. Montagna *et al.*, Comput. Phys. Commun. **93** (1996) 120–126
- 42 G. Montagna *et al.*, Comput. Phys. Commun. **117** (1999) 278–289, updated to include initial state pair radiation (G. Passarino, priv. comm.)
- 43 D. Y. Bardin *et al.*, Z. Phys. **C44** (1989) 493
- 44 D. Y. Bardin *et al.*, Comput. Phys. Commun. **59** (1990) 303–312
- 45 D. Y. Bardin *et al.*, Nucl. Phys. **B351** (1991) 1–48
- 46 D. Y. Bardin *et al.*, Phys. Lett. **B255** (1991) 290–296
- 47 D. Y. Bardin *et al.*, *ZFITTER: An Analytical program for fermion pair production in e^+e^- annihilation*, Eprint arXiv:hep-ph/9412201, 1992
- 48 D. Y. Bardin *et al.*, Comput. Phys. Commun. **133** (2001) 229–395, updated with results from [208]
- 49 Two Fermion Working Group, M. Kobel, *et al.*, *Two-fermion production in electron positron collisions*, Eprint hep-ph/0007180, 2000
- 50 A. B. Arbuzov *et al.*, *ZFITTER: a semi-analytical program for fermion pair production in e^+e^- annihilation, from version 6.21 to version 6.42*, Eprint hep-ph/0507146, 2005
- 51 W. Beenakker, F.A. Berends and S.C. van der Marck, Nucl. Phys. **B349** (1991) 323–368, (ALIBABA)
- 52 ALEPH Collaboration, D. Decamp *et al.*, Z. Phys. **C48** (1990) 365–392
- 53 ALEPH Collaboration, D. Decamp *et al.*, Z. Phys. **C53** (1992) 1–20
- 54 ALEPH Collaboration, D. Buskulic *et al.*, Z. Phys. **C60** (1993) 71–82
- 55 ALEPH Collaboration, D. Buskulic *et al.*, Z. Phys. **C62** (1994) 539–550
- 56 ALEPH Collaboration, R. Barate *et al.*, Eur. Phys. J. **C14** (2000) 1–50

-
- 57 DELPHI Collaboration, P. Abreu *et al.*, Nucl. Phys. **B367** (1991) 511–574
- 58 DELPHI Collaboration, P. Abreu *et al.*, Nucl. Phys. **B417** (1994) 3–57
- 59 DELPHI Collaboration, P. Abreu *et al.*, Nucl. Phys. **B418** (1994) 403–427
- 60 DELPHI Collaboration, P. Abreu *et al.*, Eur. Phys. J. **C16** (2000) 371–405
- 61 L3 Collaboration, B. Adeva *et al.*, Z. Phys. **C51** (1991) 179–204
- 62 L3 Collaboration, O. Adriani *et al.*, Phys. Rept. **236** (1993) 1–146
- 63 L3 Collaboration, M. Acciarri *et al.*, Z. Phys. **C62** (1994) 551–576
- 64 L3 Collaboration, M. Acciarri *et al.*, Eur. Phys. J. **C16** (2000) 1–40
- 65 OPAL Collaboration, G. Alexander *et al.*, Z. Phys. **C52** (1991) 175–208
- 66 OPAL Collaboration, P. D. Acton *et al.*, Z. Phys. **C58** (1993) 219–238
- 67 OPAL Collaboration, R. Akers *et al.*, Z. Phys. **C61** (1994) 19–34
- 68 OPAL Collaboration, G. Abbiendi *et al.*, Eur. Phys. J. **C19** (2001) 587–651
- 69 The ALEPH, DELPHI, L3, OPAL, SLD Collaborations, the LEP Electroweak Working Group, the SLD Electroweak and Heavy Flavour Groups, Phys. Rept. **427** (2006) 257
- 70 R. Assmann *et al.*, Eur. Phys. J. **C6** (1999) 187–223
- 71 SLD Collaboration, K. Abe *et al.*, Phys. Rev. Lett. **70** (1993) 2515–2520
- 72 SLD Collaboration, K. Abe *et al.*, Phys. Rev. Lett. **73** (1994) 25–29
- 73 SLD Collaboration, K. Abe *et al.*, Phys. Rev. Lett. **78** (1997) 2075–2079
- 74 SLD Collaboration, K. Abe *et al.*, Phys. Rev. Lett. **84** (2000) 5945–5949
- 75 SLD Collaboration, K. Abe *et al.*, Phys. Rev. Lett. **86** (2001) 1162–1166
- 76 SLD Collaboration, K. Abe *et al.*, Phys. Rev. Lett. **79** (1997) 804–808
- 77 P. H. Eberhard *et al.*, in *Z Physics At Lep 1. Proceedings, Workshop, Geneva, Switzerland, September 4-5, 1989. Vol. 1: Standard Physics*, CERN 89-08, ed. G. Altarelli, R. Kleiss, and C. Verzegnassi, (CERN, Geneva, Switzerland, 1989), pp. 235–265
- 78 ALEPH Collaboration, A. Heister *et al.*, Eur. Phys. J. **C20** (2001) 401–430
- 79 ALEPH Collaboration, D. Buskulic *et al.*, Z. Phys. **C69** (1996) 183–194
- 80 ALEPH Collaboration, D. Buskulic *et al.*, Z. Phys. **C59** (1993) 369–386
- 81 ALEPH Collaboration, D. Decamp *et al.*, Phys. Lett. **B265** (1991) 430–444
- 82 DELPHI Collaboration, P. Abreu *et al.*, Eur. Phys. J. **C14** (2000) 585–611
- 83 DELPHI Collaboration, P. Abreu *et al.*, Z. Phys. **C67** (1995) 183–202
- 84 L3 Collaboration, M. Acciarri *et al.*, Phys. Lett. **B429** (1998) 387–398
- 85 L3 Collaboration, M. Acciarri *et al.*, Phys. Lett. **B341** (1994) 245–256
- 86 L3 Collaboration, O. Adriani *et al.*, Phys. Lett. **B294** (1992) 466–478

- 87 OPAL Collaboration, G. Abbiendi *et al.*, Eur. Phys. J. **C21** (2001) 1–21
- 88 OPAL Collaboration, G. Alexander *et al.*, Z. Phys. **C72** (1996) 365–375
- 89 OPAL Collaboration, R. Akers *et al.*, Z. Phys. **C65** (1995) 1–16
- 90 OPAL Collaboration, G. Alexander *et al.*, Phys. Lett. **B266** (1991) 201–217
- 91 M. Davier *et al.*, Phys. Lett. **B306** (1993) 411–417
- 92 S. Jadach, B.F.L. Ward and Z. Wąs, Comput. Phys. Commun. **79** (1994) 503, (KORALZ 4.0)
- 93 E. Barbiero, B. van Eijk, and Z. Wąs, Comput. Phys. Commun. **66** (1991) 115, CERN-TH 7033/93, (PHOTOS)
- 94 Particle Data Group, C. Caso *et al.*, Eur. Phys. J. **C3** (1998) 1–794
- 95 Particle Data Group, D. E. Groom *et al.*, Eur. Phys. J. **C15** (2000) 1–878
- 96 R. Decker and M. Finkemeier, Phys. Rev. **D48** (1993) 4203
- 97 M. Finkemeier, Radiative corrections to the decay $\tau \rightarrow \pi\nu$, Ph.D. thesis, University of Karlsruhe, Feb 1994
- 98 ALEPH Collaboration, D. Buskulic *et al.*, Phys. Lett. **B313** (1993) 535–548
- 99 ALEPH Collaboration, R. Barate *et al.*, Phys. Lett. **B401** (1997) 150–162
- 100 DELPHI Collaboration, P. Abreu *et al.*, Eur. Phys. J. **C10** (1999) 415–442
- 101 DELPHI Collaboration, J. Abdallah *et al.*, Eur. Phys. J. **C32** (2004) 185–208
- 102 L3 Collaboration, M. Acciarri *et al.*, Eur. Phys. J. **C13** (2000) 47–61
- 103 OPAL Collaboration, G. Abbiendi *et al.*, Eur. Phys. J. **C8** (1999) 217–239
- 104 D. J. Jackson, Nucl. Instrum. Meth. **A388** (1997) 247–253
- 105 ALEPH Collaboration, R. Barate *et al.*, Phys. Lett. **B401** (1997) 163–175
- 106 SLD Collaboration, K. Abe *et al.*, Phys. Rev. **D71** (2005) 112004
- 107 ALEPH Collaboration, R. Barate *et al.*, Eur. Phys. J. **C4** (1998) 557–570
- 108 ALEPH Collaboration, R. Barate *et al.*, Eur. Phys. J. **C16** (2000) 597–611
- 109 DELPHI Collaboration, P. Abreu *et al.*, Eur. Phys. J. **C12** (2000) 225–241
- 110 DELPHI Collaboration, P. Abreu *et al.*, Eur. Phys. J. **C12** (2000) 209–224
- 111 OPAL Collaboration, G. Alexander *et al.*, Z. Phys. **C72** (1996) 1–16
- 112 OPAL Collaboration, K. Ackerstaff *et al.*, Eur. Phys. J. **C1** (1998) 439–459
- 113 ALEPH Collaboration, A. Heister *et al.*, Eur. Phys. J. **C22** (2001) 201–215
- 114 ALEPH Collaboration, A. Heister *et al.*, Eur. Phys. J. **C24** (2002) 177–191
- 115 DELPHI Collaboration, P. Abreu *et al.*, Z. Phys. **C65** (1995) 569–586
- 116 DELPHI Collaboration, J. Abdallah *et al.*, Eur. Phys. J. **C34** (2004) 109–125

-
- 117 DELPHI Collaboration, P. Abreu *et al.*, Eur. Phys. J. **C10** (1999) 219–237
- 118 DELPHI Collaboration, J. Abdallah *et al.*, Eur. Phys. J. **C40** (2005) 1–25
- 119 L3 Collaboration, O. Adriani *et al.*, Phys. Lett. **B292** (1992) 454–462
- 120 L3 Collaboration, M. Acciarri *et al.*, Phys. Lett. **B448** (1999) 152–162
- 121 L3 Collaboration, M. Acciarri *et al.*, Phys. Lett. **B439** (1998) 225–236
- 122 OPAL Collaboration, G. Abbiendi *et al.*, Phys. Lett. **B546** (2002) 29–47
- 123 OPAL Collaboration, G. Abbiendi *et al.*, Phys. Lett. **B577** (2003) 18–36
- 124 OPAL Collaboration, G. Alexander *et al.*, Z. Phys. **C73** (1997) 379–395
- 125 ALEPH Collaboration, R. Barate *et al.*, Phys. Lett. **B434** (1998) 415–425
- 126 SLD Collaboration, K. Abe *et al.*, Phys. Rev. Lett. **88** (2002) 151801
- 127 SLD Collaboration, K. Abe *et al.*, Phys. Rev. Lett. **83** (1999) 3384–3389
- 128 SLD Collaboration, K. Abe *et al.*, Phys. Rev. Lett. **81** (1998) 942–946
- 129 SLD Collaboration, K. Abe *et al.*, Phys. Rev. Lett. **90** (2003) 141804
- 130 SLD Collaboration, K. Abe *et al.*, Phys. Rev. Lett. **83** (1999) 1902–1907
- 131 SLD Collaboration, K. Abe *et al.*, Phys. Rev. Lett. **94** (2005) 091801
- 132 SLD Collaboration, K. Abe *et al.*, Phys. Rev. **D63** (2001) 032005
- 133 LEP Heavy Flavor Working Group, D. Abbaneo *et al.*, Eur. Phys. J. **C4** (1998) 185–191
- 134 G. Altarelli and B. Lampe, Nucl. Phys. **B391** (1993) 3–22
- 135 V. Ravindran and W. L. van Neerven, Phys. Lett. **B445** (1998) 214–222
- 136 S. Catani and M. H. Seymour, JHEP **9907** (1999) 023
- 137 ALEPH, DELPHI, L3, OPAL Collaborations, Nucl. Instrum. Meth. **A378** (1996) 101–115
- 138 A. Freitas and K. Mönig, Eur. Phys. J. **C40** (2005) 493–496
- 139 ALEPH Collaboration, D. Buskulic *et al.*, Z. Phys. **C71** (1996) 357–378
- 140 DELPHI Collaboration, P. Abreu *et al.*, Phys. Lett. **B277** (1992) 371–382
- 141 OPAL Collaboration, P. D. Acton *et al.*, Phys. Lett. **B294** (1992) 436–450
- 142 UA1 Collaboration, G. Arnison *et al.*, Phys. Lett. **B122** (1983) 103
- 143 UA2 Collaboration, M. Banner *et al.*, Phys. Lett. **B122** (1983) 476
- 144 UA1 Collaboration, G. Arnison *et al.*, Phys. Lett. **B126** (1983) 398
- 145 UA2 Collaboration, P. Bagnaia *et al.*, Phys. Lett. **B129** (1983) 130
- 146 D0 Collaboration, B. Abbott *et al.*, Phys. Rev. **D62** (2000) 092006
- 147 D0 Collaboration, V. M. Abazov *et al.*, Phys. Rev. **D66** (2002) 012001
- 148 CDF Collaboration, A. A. Affolder *et al.*, Phys. Rev. **D64** (2001) 052001

-
- 149 The CDF Collaboration, *First Measurement of the W bosons Mass in Run II of the Tevatron*, preprint arXiv:0707.0085 [hep-ex]; *First Run II Measurement of the W Boson Mass*, preprint arXiv:0708.3642 [hep-ex]
- 150 CDF Collaboration, F. Abe *et al.*, Phys. Rev. Lett. **74** (1995) 341–345
- 151 CDF Collaboration, A. A. Affolder *et al.*, Phys. Rev. Lett. **85** (2000) 3347–3352
- 152 D0 Collaboration, V. M. Abazov *et al.*, Phys. Rev. **D66** (2002) 032008
- 153 The DØ Collaboration, *Direct Measurement of the W Boson Width in $p\bar{p}$ Collisions at $\sqrt{s} = 1.96$ TeV*, DØ Note 4563-CONF (August 2004)
- 154 The CDF Collaboration, the DØ Collaboration, and the Tevatron Electroweak Working Group, Phys. Rev. **D70** (2004) 092008
- 155 Tevatron Electroweak Working Group Collaboration, (2005)
- 156 The LEP Collaborations ALEPH, DELPHI, L3, OPAL, and the LEP Electroweak Working Group, *A Combination of Preliminary Electroweak Measurements and Constraints on the Standard Model*, Eprint hep-ex/0612034 and update winter 2007, <http://www.cern.ch/LEPEWWG>, CERN, 2006
- 157 ALEPH Collaboration, R. Barate *et al.*, Phys. Lett. **B401** (1997) 347–362
- 158 DELPHI Collaboration, P. Abreu *et al.*, Phys. Lett. **B397** (1997) 158–170
- 159 L3 Collaboration, M. Acciarri *et al.*, Phys. Lett. **B398** (1997) 223–238
- 160 OPAL Collaboration, K. Ackerstaff *et al.*, Phys. Lett. **B389** (1996) 416–428
- 161 ALEPH Collaboration, S. Schael *et al.*, (2006)
- 162 DELPHI Collaboration, J. Abdallah *et al.*, (2006)
- 163 L3 Collaboration, M. Acciarri *et al.*, Euro. Phys. C **45** (2006) 569
- 164 OPAL Collaboration, G. Abbiendi, hep-ex/0508060 (2005)
- 165 M. Cacciari *et al.*, JHEP **04** (2004) 068
- 166 N. Kidonakis and R. Vogt, Phys. Rev. **D68** (2003) 114014
- 167 D0 Collaboration, V. M. Abazov, (2006)
- 168 The CDF Collaboration, *Search for Single Top Quark Production in $955/\text{pb}$ using the Matrix Element Technique*, CDF Note 8588, November 2006
- 169 The DØ Collaboration, *Measurement of the top quark mass in the lepton+jets channel using DØ run-II Data: The Low Bias Template Method*, DØ Note 4728, March 2005
- 170 The CDF Collaboration, *Measurement of the top mass in the all-hadronic channel using the template method with $1.02/\text{fb}$* , CDF Note 8420, July 2006
- 171 DØ Collaboration, V. M. Abazov *et al.*, Nature **429** (2004) 638–642
- 172 CDF Collaboration, F. Abe *et al.*, Phys. Rev. Lett. **82** (1999) 271–276
- 173 CDF Collaboration, F. Abe *et al.*, Erratum: Phys. Rev. Lett. **82** (1999) 2808–2809
- 174 DØ Collaboration, B. Abbott *et al.*, Phys. Rev. **D60** (1999) 052001

-
- 175 CDF Collaboration, T. Affolder *et al.*, Phys. Rev. **D63** (2001) 032003
- 176 CDF Collaboration, F. Abe *et al.*, Phys. Rev. Lett. **79** (1997) 1992–1997
- 177 CDF Collaboration, A. Abulencia *et al.*, Phys. Rev. D **75** (2007) 031105(R)
- 178 The CDF Collaboration, A. Abulencia *et al.*, *Measurement of the Top-Quark Mass in the Lepton+Jets Channel using the Decay Length Technique*, CDF Conference Note 8133, accepted by Phys. Rev. D.
- 179 The CDF Collaboration, A. Abulencia *et al.*, *Measurement of the Top-Quark Mass with 940 pb^{-1} using the Matrix Element Analysis Technique*, CDF Conference Note 8375
- 180 The CDF Collaboration, A. Abulencia *et al.*, *Measurement of the top quark mass in the all hadronic channel using an in-situ calibration of the dijet invariant mass with 0.9 fb^{-1}* , CDF Note 8709
- 181 The DØ Collaboration, V.M. Abazov *et al.*, *Measurement of the top quark mass with the matrix element method using the lepton+jets 1 fb^{-1} data set*, DØ-note 5362-CONF.
- 182 The DØ Collaboration, V.M. Abazov *et al.*, *Measurement of the top quark mass in dilepton events with neutrino weighting in Run-II at DØ*, DØ-note 5347-CONF.
- 183 The Tevatron Electroweak Working Group on behalf of the CDF and DØ Collaborations, (2007)
- 184 Particle Data Group, S. Eidelman, *et al.*, Phys. Lett. **B592** (2004) 1
- 185 E. A. Paschos and L. Wolfenstein, Phys. Rev. **D7** (1973) 91–95
- 186 T. Kinoshita and M. Nio, Phys. Rev. Lett. **90** (2003) 021803
- 187 T. Kinoshita and M. Nio, Phys. Rev. **D70** (2004) 113001
- 188 M. Davier and W. J. Marciano, Ann. Rev. Nucl. Part. Sci. **54** (2004) 115–140
- 189 M. Davier *et al.*, Eur. Phys. J. **C31** (2003) 503–510
- 190 K. Hagiwara *et al.*, Phys. Lett. **B557** (2003) 69–75
- 191 K. Hagiwara *et al.*, Phys. Rev. **D69** (2004) 093003
- 192 S. Eidelman and F. Jegerlehner, Z. Phys. **C67** (1995) 585–602
- 193 H. Burkhardt and B. Pietrzyk, Phys. Lett. **B356** (1995) 398–403
- 194 H. Burkhardt and B. Pietrzyk, Phys. Rev. **D72** (2005) 057501
- 195 M. L. Swartz, Phys. Rev. **D53** (1996) 5268–5282
- 196 A. D. Martin and D. Zeppenfeld, Phys. Lett. **B345** (1995) 558–563
- 197 R. Alemany, M. Davier, and A. Hocker, Eur. Phys. J. **C2** (1998) 123–135
- 198 M. Davier and A. Hocker, Phys. Lett. **B419** (1998) 419–431
- 199 J. H. Kuhn and M. Steinhauser, Phys. Lett. **B437** (1998) 425–431
- 200 F. Jegerlehner, in Proceedings, 4th International Symposium, RADCOR'98, ed. J. Sola, (World Scientific, Singapore, Sep 1999), p. 75

- 201 J. Erler, Phys. Rev. **D59** (1999) 054008
- 202 A. D. Martin, J. Outhwaite, and M. G. Ryskin, Phys. Lett. **B492** (2000) 69–73
- 203 J. F. de Troconiz and F. J. Yndurain, Phys. Rev. **D65** (2002) 093002
- 204 K. Hagiwara *et al.*, Phys. Rev. **D69** (2004) 093003
- 205 J. F. de Troconiz and F. J. Yndurain, Phys. Rev. **D71** (2005) 073008
- 206 S. Bethke, Nucl. Phys. Proc. Suppl. **135** (2004) 345–352
- 207 ALEPH, DELPHI, L3, and OPAL Collaborations, Phys. Lett. **B565** (2003) 61–75
- 208 A. B. Arbuzov, JHEP **07** (2001) 043.